TÉCNICO LISBOA

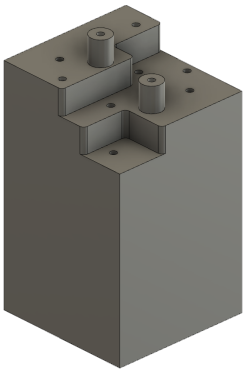

Design and exploitation of a vorticity probe for turbulence studies in fusion devices

Sérgio Alexandre Correia Caramona

Thesis to obtain the Master of Science Degree in

Engineering Physics

Supervisor(s): Doutor Bruno Miguel Soares Gonçalves
Doutor Carlos Alberto Nogueira Garcia Silva

Examination Committee

Chairperson: Professor Horácio João Matos Fernandes
Supervisor: Doutor Bruno Miguel Soares Gonçalves
Member of the Committee: Doutor Rui Miguel Dias Alves Coelho

September 2020

Dedicated to my parents,

Thank you for all the support during this journey

Acknowledgments

Thanks to Dr. Bruno Gonçalves and Dr. Carlos Silva, who supervised my work. They were always helpful and open to discuss my results, bringing new ideas that were crucial though all the work. I would also like to thank Humberto Figueiredo from IPFN for guiding me through all the experimental process, being always available to clarify all my doubts, giving me all the tools I needed to conduct this thesis.

To my family, a special thanks for the values instilled through my education process. It was thanks to your effort and unconditional suport that it was possbible to finish this stage

I would also like to thank my friends for all the support during this years.

Resumo

A vorticidade, uma quantidade associada ao transporte de estruturas num regime turbulento, que pode ser vista como uma medida local do rotacional do campo de velocidade, é estudada no tokamak IST-TOK. Recorrendo a uma sonda de Langmuir, especificamente desenhada para extrair potenciais fluctuantes e correntes de saturação iónicas, é possível inferir sobre quantidades características do plasma como: Reynolds Stress, fluxo de partículas, vorticidade e fluxo de vorticidade e, ainda, a velocidade poloidal. É apresentada uma descrição estatística destes processos que evidencia a relação entre flutuações em gradientes com o transporte turbulento. A influência da polarização nos parâmetros do plasma é estudada com o auxílio de um eléctrodo emissivo. Efeitos de uma configuração magnética com um campo superior são explorados. Estes são estudos importantes que poderão ser uteis para desvendar mecanismos relacionados com a turbulência em plasmas na região da Scrape off Layer.

Palavras-chave: Fusão nuclear,potenciais fluctuantes, vorticidade, Reynolds Stress, fluxo de particulas, velocidade poloidal

Abstract

The vorticity, a quantity associated with the transport of structures on turbulent flow, that gives a local measure of the velocity field circulation in the plasma fluid, is studied at ISTTOK tokamak. Recurring to a Langmuir probe array, specifically designed to acquire floating potentials and ionic saturation currents, it is possible to infer about some plasma characteristics as: Reynolds stress, particle flux, vorticity, vorticity flux, and even the poloidal velocity. A detailed statistical description of these processes is presented which highlights the interplay between fluctuations in gradients and turbulent transport. The influence of polarization on global and edge plasma parameters is studied with a negative bias induced by an emissive electrode. The effects of higher magnetic field configurations on these quantities is also explored. These are important studies, that hopefully will help to unveil some mechanisms behind the plasma turbulence around the Scrape off Layer.

Keywords: Nuclear fusion, floating potential, vorticity, Reynolds Stress, Particle flux, Poloidal velocity

Contents

List of Tables

List of Figures

Chapter 1

Introduction

Global energy consumption is projected to increase by 30% until 2040[1]. A growing global economy and population presents itself with some challenges to meet these energy demands.

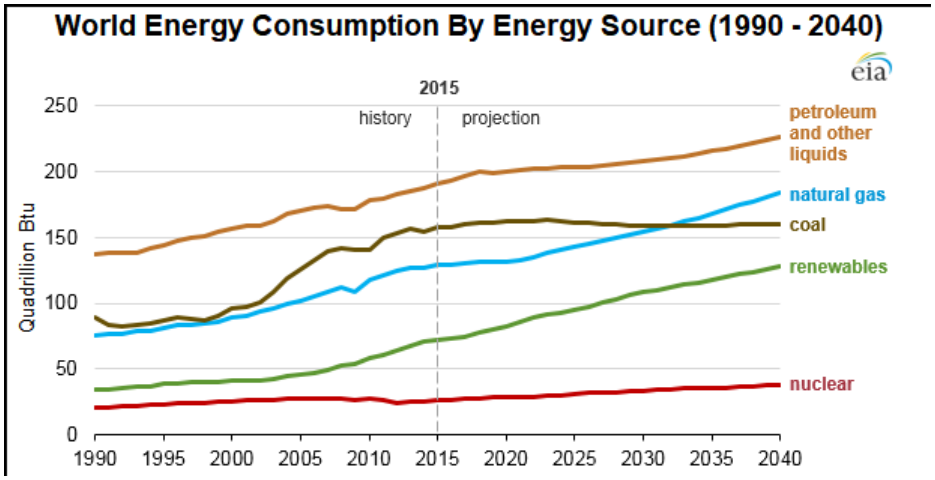

Figure 1.1: Electricity growth demand by energy source [1]

The fossil energy sources, which make up by far the majority of world-wide power today, are limited and associated with carbon dioxide and other greenhouse gas emissions to the atmosphere, therefore, from a longterm point of view they cannot stand as a solution to this problem.

The common renewable energy sources keep expanding, with the population being more aware of the climate changes and the implementation of government policies that support renewable energy worldwide. In Europe, the energy strategies set by the European Commission for a more sustainable and low-carbon economy lead to an increase of 64% of renewable electricity produced in the period between 2007-2017[2], with a stimulus that pretends to increase the use of renewable energy sources up to 20% of the total energy consumption by 2020. On the other hand, these sources are inconsistent, depending on the weather to be able to collect energy and are not completely 'green' with the pollution effects associated with the production of devices and the manufacturing of the structures. The low efficiency of renewable energy technologies, the battery storage required due to the intermittent power supply and the space usage requirements also present a challenge to meet the constant energy growing demand.

A new large-scale, clean and carbon-free form of energy production is then needed, and one of the options worth pursuing is nuclear fusion. Fusion emits only helium as exhaust, producing zero greenhouse gas emissions and without long-lived waste, in a process inherently safe. As a safe and clean energy source, power stations can be located close to where the energy is needed, eliminating the battery storage requirement and assuring the desired long term solution.

1.1 Plasma Fusion

Fusion energy comes from controlled nuclear fusion reactions, where the nuclei of small atoms fuse into a single and heavier atom, releasing high amounts of energy, the very same process that fuels stars like the Sun. For light atoms(mass up to iron) there is an increase in the binding energy per nucleon, that represents the work that must be done to disassemble a nucleus into free neutrons and protons. Therefore, in fusion reactions, a small amount of mass is converted into a large amount of energy due to Einstein's relation $E = mc^2$, by the large conversion factor c^2. Although, taking the process that fuels the stars to Earth it is not easily achievable. Fusion reactions are inhibited by the electrical repulsive force between two close positively charged nuclei, the Coulomb force.

The atom's kinetic energy must be then high enough to overcome the Coulomb barrier, which means that atoms need to be heated to high temperatures, in the order of $10^8 K$. In these conditions, the atoms become ionized with the electrons being separated from the positive charges. This state of the matter is called plasma, an electrically conducting medium in which there are roughly equal numbers of positively and negatively charged particles. Nuclei with very low mass numbers have lesser binding energy per nucleon, as presented in Figure 1.2, and are less stable becoming easier to separate the nucleus into its constituent nucleons.

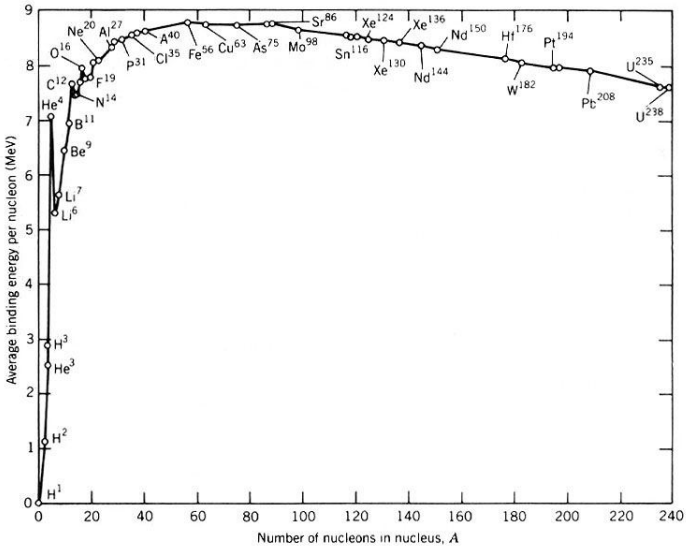

Figure 1.2: Average binding energy per nucleon number.[1]

[1] Source:https://it.wikipedia.org/wiki/File:Binding_energy.jpg

The most prominent candidates for fusion are the hydrogenic elements, that due to the small charge, allow fusion reactions to occur with a lower energy input. Although different isotopes of light elements can be paired to achieve fusion, the deuterium-tritium (DT) reaction has been identified as the most efficient for fusion devices, due to the higher effective cross-section at a lower temperature as shown in the Figure 1.3

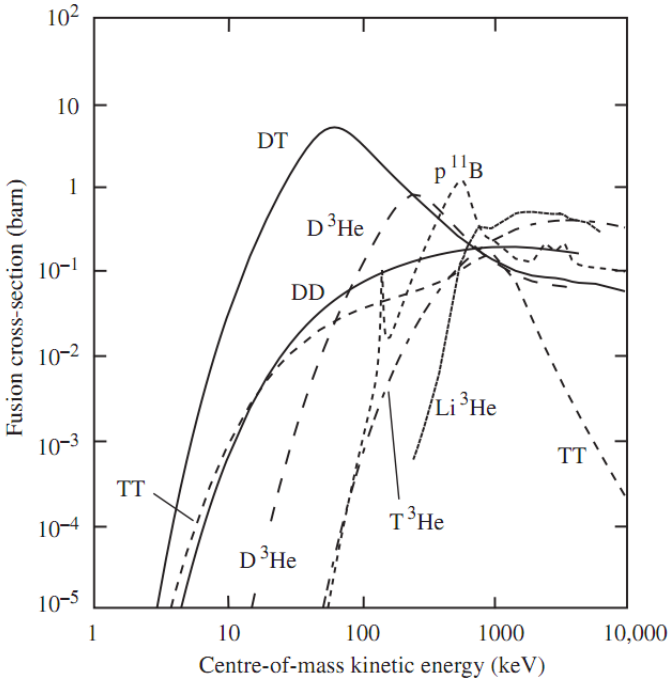

Figure 1.3: Fusion cross section as a function of the energy for the main reaction candidates [2]

The Deuterium Tritium fusion reaction occurs as follows:

$$ {}^{2}_{1}D + {}^{3}_{1}T \rightarrow {}^{4}_{2}He(3.5MeV) + {}^{1}_{0}n(14.1MeV) \tag{1.1} $$

at a relatively low temperature(around 10keV). With the same amount of fuel, the reaction releases around four million times more energy than burning coal, gas or oil and four times more energy than nuclear fission.

Deuterium is practically inexhaustible being present in all forms of water, easily extracted by distillation. Tritium is radioactive, decaying with a half-life of 12.3 years which makes him rare, with a natural abundance around 3.5Kg. This problem can be solved extracting the element by a process called Tritium breeding. The isotope is produced inside the reactor in the Breeding Blanket using lithium-based materials, where the fusion neutrons escape the plasma and react with the Lithium to produce Tritium as follows:

[2] Source:www-pnp.physics.ox.ac.uk/~barra/teaching/overheads/

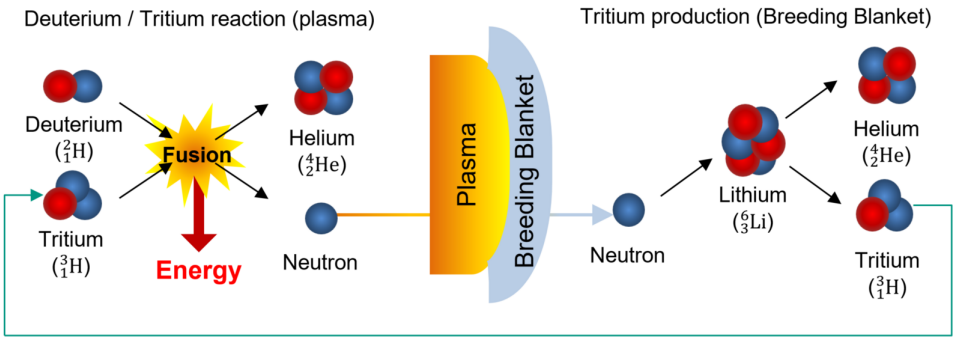

Figure 1.4: Schematic diagram of the tritium breeding inside a fusion reactor [3]

Since Lithium is easy to extract and abundant on earth (the reserves can fulfill the process for millions of years), the sustainability of Deuterium-Tritium fusion is guaranteed. Fusion is not only sustainable but also clean, without the long-lived radioactive waste associated with fission, or the emission of carbon dioxide and other greenhouse gases from fossil sources. It is also safe, without the risk of meltdown since any disturbance leads the plasma to cool down, and the reaction to stop.

Fusion seems then ideal to solve the energetic problem on earth, but replicating conditions similar to those in the stars is a complex process.

Fusion not only requires a sufficiently high temperature to overcome the Coulomb barrier, but that temperature should also be maintained for a sufficient amount of time, the confinement time τ_E. In stars, the high pressure confines the reactants, but on earth, we don't have the technology to recreate these massive pressures, with plasma confinement raising technical hurdles and presenting itself as one of the biggest challenges. The confinement time is defined as the time that the plasma is maintained at a temperature above the critical ignition temperature, to yield more energy from the fusion that has been invested to heat the plasma and compensate for the losses. With the temporal variation of the plasma energy W given by: $dW/dt = P_{alpha} + P_{external} - P_{losses}$, where P_{alpha} is the heating power supplied by the alpha particles to the plasma,$P_{external}$ the external power coupled to plasma and P_{losses} the power losses due to impurities, and particles/energy transport. The energy confinement time can be defined as $\tau_E = W/P_{losses}$, with the ignition criterion written as[3]:

$$nT\tau_E > 10^{21}(keVm^{-3}s) \tag{1.2}$$

Current devices could not reach and sustain such conditions, in order to reach a continuous mode of operation.

The two main designs to meet Lawson's criterium are the magnetic confinement and inertial confinement:

- Inertial confinement configurations consist in a setup of powerfull laser beams striking a spherical pellet containing Tritium and Lithium. The heating blows off the outer layers of the pellet and, following Newton's third law, compress the core until fusion occurs.

[3] https://www.euro-fusion.org/news/2017-3/tritium-a-challenging-fuel-for-fusion/

- Magnetic confinement uses the electrical conductivity properties of the plasma to confine the material inside a chamber with magnetic fields.

Magnetic confinement is the most developed and promising path to controlled fusion, with the tokamak being the most extensively investigated concept among all the configurations. Tokamak, a Russian acronym for ”toroidal chamber with axial magnetic field, is a configuration where the magnetic lines are helices that spiral around the torus. A strong toroidal magnetic field is generated by external magnetic coils, as in Figure1.5. Due to the toroidal configuration, the toroidal field generated is not uniform along the radial distance. To prevent the plasma from becoming unstable due to this, a poloidal magnetic field is produced by the plasma current itself, using a solenoid passing through the torus center. These magnetic configurations are specially designed to avoid particle losses at the end of the magnetic field lines, using divertors or limiters.

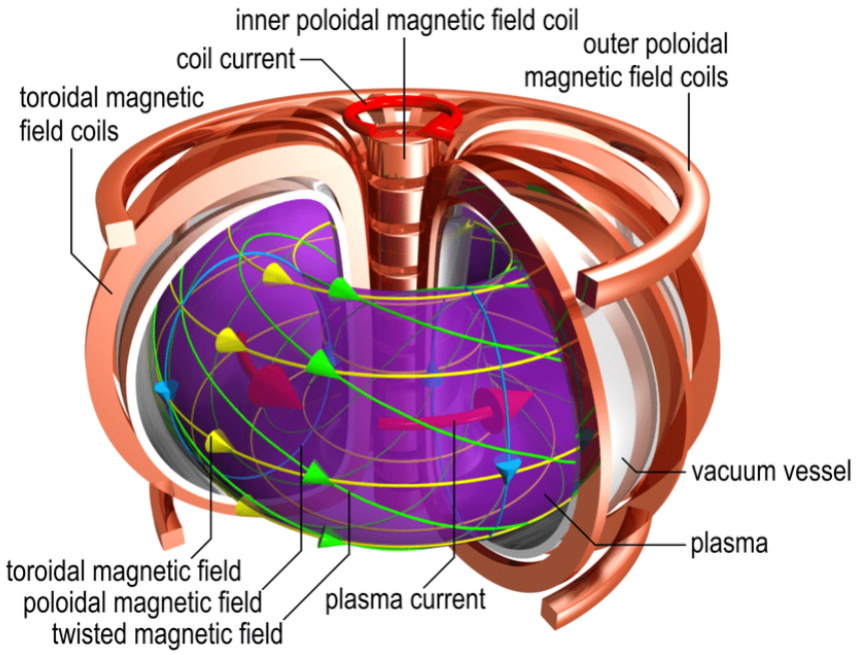

Figure 1.5: Tokamak schematic [4]

1.1.1 Limiter, Divertor and the Scrape-off-Layer

It is important to control the plasma interactions with the walls and minimize them. One of the approaches is physically limit the plasma radius using a limiter inside the device, with the magnetic field lines impinging directly on it. The limiter defines the last closed flux surface(LCFS), which is the boundary between the core plasma with magnetic field lines closing at themselves and the scrape off layer, where the magnetic field lines close at the tokamak walls. The limiter configuration has become less relevant due to the alternative option that proved to be more favorable for confinement, the divertor. The divertor employs an external magnetic coil that generates a current parallel to the plasma current, with the field lines contacting the vessel wall on specially equipped divertor plates. The limiter configuration is used at ISTTOK.

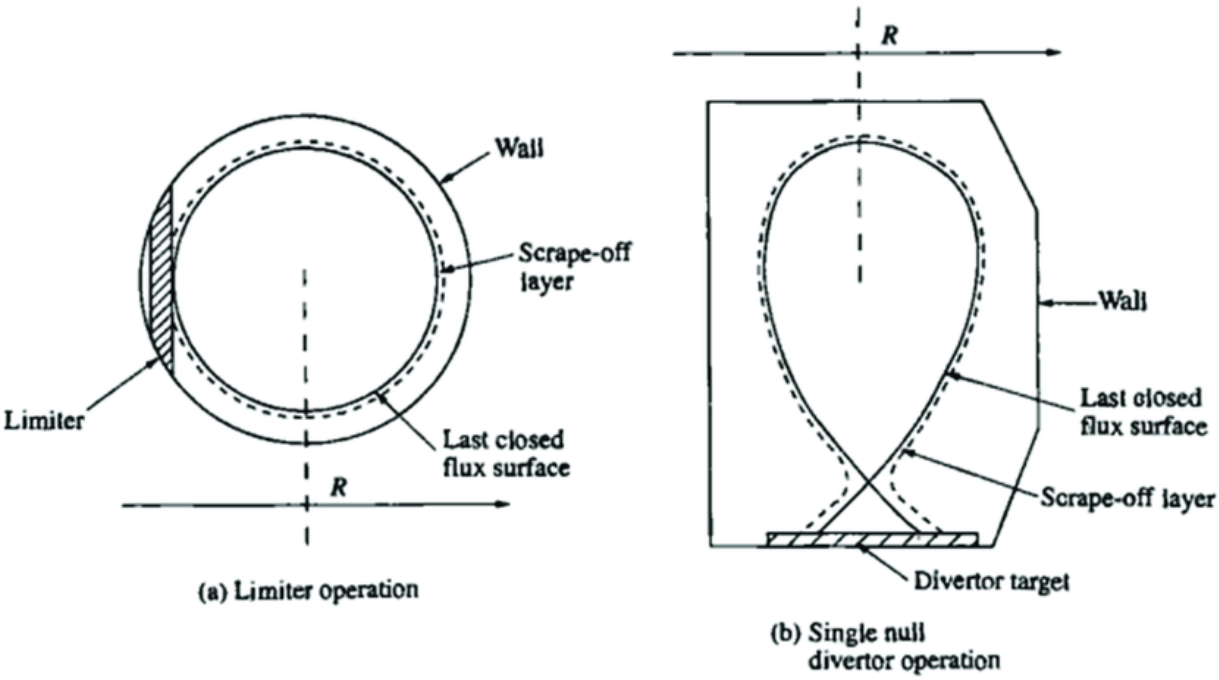

Figure 1.6: Schematic diagram of the limiter and divertor configuration [4]

A fast particle loss occurs in the limiter/divertor due to the Debye sheath created around it, limiting the radius of the plasma to a radius slightly larger than the limiter position.The limiter/divertor should, in theory, reduce the particles transport to SOL to particle collisions events in the radial direction[5]. Although, the interaction between electrons, ions, atoms and solid surfaces seems to dominate the overall plasma behavior with SOL plasmas characterized by a large effective resistivity $\mu_{||}$ due to low temperatures(comparing to the core) and the presence of open field lines that prevent charge flow[6], invalidating the ideal MHD Ohm's law

$$E' = E + V \times B = \mu_{||} j = 0 \tag{1.3}$$

which leads to instabilities. The lack of knowledge in this region requires developments of critical importance for the *ITER* experiment due to problems that affect current tokamaks:[6]

- The exhaust of fusion power without damaging the tokamak walls.
- The removal of fusion ash and other impurities from the core plasma.
- Control of material erosion and migration in the Tokamak vessel.

[4]Source:https://www.researchgate.net/figure/Configurations-of-plasma-facing-components-a-limiter-b-divertor-From_fig6_294430748

1.2 Scope and Outline of the Thesis

This work emphasizes the importance of turbulent regimes in the Srape of Layer(SOL) and the impact they have on the overall plasma confinement. There is still much to learn about fusion before this option becomes possible and viable, with some of the problems arriving from the fact that turbulence mechanisms are still not well understood yet. From previous observations, it is clear that the suppression of edge turbulence results in improve confinement for the entire device. Edge turbulence also affects heat and particle flux to the walls which lead to wall erosion and plasma contamination[7].

In Chap.2 a theoretical overview of the problem is presented, introducing the anomalous transport, in order to explain experimental results that contradict classical and neoclassical theories. The localized and intermittent characteristics of this transport is emphasized introducing eddies and Kolgomorov's theory. The relevant quantities associated with the statistical analysis are derived and related to floating potentials that can be acquired with Langmuir probes, with special focus on the measure of the vorticity around the SOL at ISTTOK tokamak, a large aspect ratio tokamak with a circular cross-section and a poloidal (graphite) limiter. The vorticity is a local measure of the velocity field circulation in the plasma fluid, which plays a key role in the transport of energy and particles in plasmas and fluids in general[8][9]. The theory behind the computation of quantities like: particle flux, vorticity flux and Reynolds stress is also presented. A method that involves the local wavenumber and frequency spectral density, in order to estimate the poloidal velocity is introduced and compared to the usual cross-correlation method. The influence of polarization on global and edge plasma parameters is introduced along with the experimental method that will be used during this work to study such effects. At last, the Langmuir probe theory is presented.

In Chap.3 the implementation of the theory presented in Chap.2 is presented with the design and construction of a Langmuir probe array that will be used during the experiments at ISTTOK. The set of equations to compute the quantities presented in the previous chapter are presented as function of floating potential or ion current saturation signals from specific pins in the probe array. The chapter closes with a detailed computational analysis description, presenting all the methods and algorithms used.

In Chap.4 the results of the experiment are explored and compared to previous experiments and simulations.

In Chap.5 a physical explanation for the observations is discussed. Possible future improvements and developments in this work lines are proposed.

Chapter 2

Background

2.1 Theoretical Overview

Plasmas in fusion research are far from thermodynamic equilibrium, which leads to a dynamical behavior and the formation of structures that affect the transport mechanisms. Spatial variations of quantities like density, temperature, the intensity of the magnetic field or external force fields create instabilities, with the properties of plasma changing dramatically, leading to anomalous transport. These mechanisms constitute themselves as one obstacle to achieving ignition in magnetically confined plasmas. The SOL region constitute only a small portion of the tokamak device in terms of geometrical dimensions and heat content. Although, this small region influences the global confinement significantly with sharp variations in the gradients of some plasma parameters as: temperature, floation potential or density. During the past decades, studies in this region shifted towards a non stationary/intermittent approach for edge turbulence[10].

Probability distribution functions (PDFs) of fluctuations, in both plasma density and floating potentials are reported to be non-Gaussian in all fusion devices [10]. Several measurements support that the intermittent behavior becomes even more non Gaussian applying band pass filters to the signals, indicating that intermittency becomes stronger at shorter scales. Analysis of the edge fluctuations show that fluctuations amplitude exhibits self-similarity of different kinds over different ranges [10, 11]

2.1.1 Plasma transport in fusion devices

Transport mechanisms are a fundamental subject, closely related to the confinement in magnetized plasmas. Since the fusion power increases with the square of the density:

$$P_{Fusion} = n_A n_B \langle \sigma v \rangle_{AB} E_{AB} V \tag{2.1}$$

where n is the density, E_{AB} the energy released in one fusion reaction, V the volume, v the velocity and σ the cross section, any density variation due to particles/energy transport will have effect on the fusion power.

When moving charges encircle the magnetic fields, they will gyrate around the magnetic field, with the typical size of the orbit known as Larmor radius given by:

$$\rho_E = \frac{mv_\perp}{qB} \tag{2.2}$$

where m is the mass of the particle, $v_\perp$ the component of velocity perpendicular to the direction of the magnetic field, q the electric charge and B the strength of the magnetic field. These binary Coulomb collisions change the helical path of the particles, with the particles eventually escaping the boundary of the field. Classical transport theory in tokamak describes the collisional transport in a uniform magnetic field through binary Coulomb collisions, and can be expressed as diffusive transport with transport coefficient [12]

$$D \sim \rho_E^2 \nu \tag{2.3}$$

where ν is the collision frequency and ρ_E the electron gyroradius (Larmor radius). The classical diffusion is characterized by very small diffusion coefficients since, only the ineffective electron-ion collisions contribute to the particle transport.

Although, due to the tokamak geometry, the magnetic field is non-uniform, with phenomena like ΔB, curvature drift affecting the motion of the particles. The nonlocality and geometry dependence also become particularly important in the high-temperature regime of proposed thermonuclear reactors.

In classical and neoclassical theories, the transport is assumed as purely diffusive, but the transport predicted by both theories can not fully explain what happens experimentally, with diffusivity coefficients that exceed the expected values. The difference between the expected and the actual transport observed is often referred to as anomalous transport, with the reasons behind it still unclear but usually attributed to turbulence driven by micro-instabilities. The importance of energy and moment transfer between flows and turbulence in fusion plasmas has been emphasized [13–16], with the observation of multiple scales in turbulence and fluctuations[17][18].

Edge and scrape-off layer(SOL) plasmas are usually characterized by a large amplitude of turbulent fluctuations with an associated enhanced transport in walls direction. Predicting SOL (the region radially outboard of the last closed flux surface) dynamics is one of the main challenges in fusion, since SOL physics determines the boundary conditions for the plasma across the machine, regulating the power losses. Transport of energy and particles in this region is usually attributed to non diffusive transport that occurs in the form of intermittent convection of coherent mesoscale plasma structures, often called blobs(or eddies) in low confinement mode (L-mode) and edge-localized modes (ELMs) in high confinement (H-mode). The vortex nature and behavior, closely related to anomalous transport and turbulence in plasmas have been attracting attention with an associated increase necessity for measuring the vorticity experimentally.

The turbulent fluxes are divided into particle flux and energy flux. These fluxes can have contributions of magnetic and electrostatic nature, with the magnetic contributions that arise from the magnetic fluctuations being negligible in the plasma boundary[19], the region where probes can be inserted to

measure the fluctuating quantities. The radial particle flux due to electrostatic fluctuation is given by:

$$\Gamma_r =< \tilde{n}.\tilde{v}_{E_r} > \tag{2.4}$$

where $\tilde{V}_{E_r}$ is the radial component of the fluctuating $E \times B$ drift. Approximating the electric field in the tokamak as an electroestatic fluctuation given by the gradient of the floating potential $\tilde{E} = -\nabla\tilde{\phi}$, with a toroidal magnetic field B, the radial and poloidal components of the $E \times B$ velocity is given respectively by:

$$\tilde{v}_r = \frac{\nabla_\theta \tilde{\phi}}{B} \propto \frac{\tilde{E}_\theta}{B} \tag{2.5}$$

$$\tilde{v}_\theta = \frac{\nabla_r \tilde{\phi}}{B} \propto \frac{\tilde{E}_r}{B} \tag{2.6}$$

where $\tilde{E}_r$ is the radial electric field ,$\tilde{E}_\theta$ the poloidal electric field and ∇_ϕ ∇_r the derivatives in poloidal and radial direction respectively. Taking these approximations, the particle flux due to electrostatic fluctuations can be expressed as function of the poloidal electric field $\tilde{E}_\theta$

$$\Gamma_r \propto< \tilde{n}.\frac{(-\tilde{E}_\theta)}{B} > \tag{2.7}$$

The coherent structures(eddies) are observed to arise near the SOL probably as a result of the change in topology from closed to open field lines[20]. These blobs, having density much higher than ambient SOL plasma density, are extended along the magnetic field lines, characterized by relatively small cross-field dimensions, and propagate outward to the wall due to ∇B plasma polarization and associated $E \times B$ drift [21]. These structures, also referred as "mesoscale [1] structures" with their perpendicular scale length being a intermediate between the ion gyro radius and the macroscopic machine dimensions [22].

Kolmogorov's theory describes how energy is transferred from larger to smaller eddies. Large eddies are unstable and break up, transferring their energy into smaller eddies, with these smaller eddies going through the same process[23]. This results in an energy cascade as shown in figure2.2 until the Reynolds number $Re(l) = u(L)L/\nu$ becomes small enough so the eddy motion is stable, and molecular viscosity is effective in dissipating the kinetic energy. In the Reynolds number expression presented above u is the velocity of the fluid, L the characteristic length and ν the kinematic viscosity. The Kolgomorov law, also known as the -5/3 law states that, in some inertial range$[k_1, k_2]$, the energy density of the flow E(k) has an approximate linear decaying behavior[24] as shown in Figure 2.1.

[1] Mesoscale refers to structures where the scale varies between the millimeter and the nanometer.

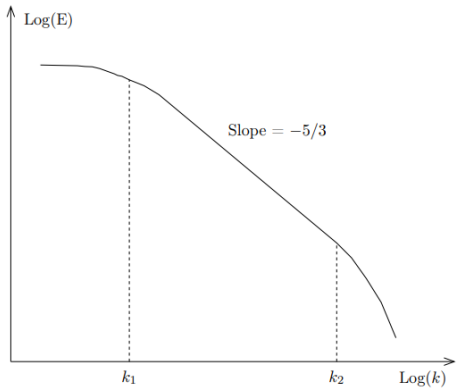

Figure 2.1: Energy spectrum Log-Log curve[24].

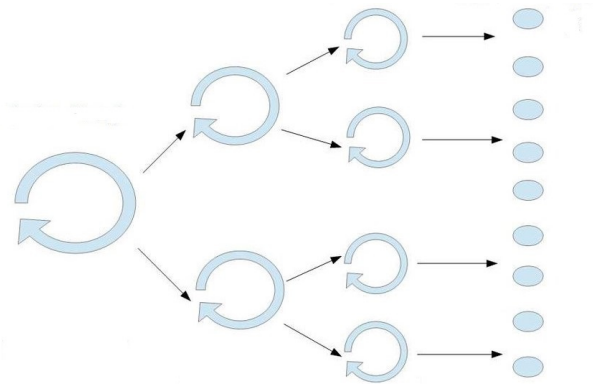

Figure 2.2: The energy cascade model of Kolmogorov[25].

At small scales, the energy is dissipated by the viscosity of the fluid. The whole transport process is known as turbulent cascade

Numerical simulations of plasma edge turbulence reveal radial motion of plasma structures arising from the LCSF into de SOL region[26]:

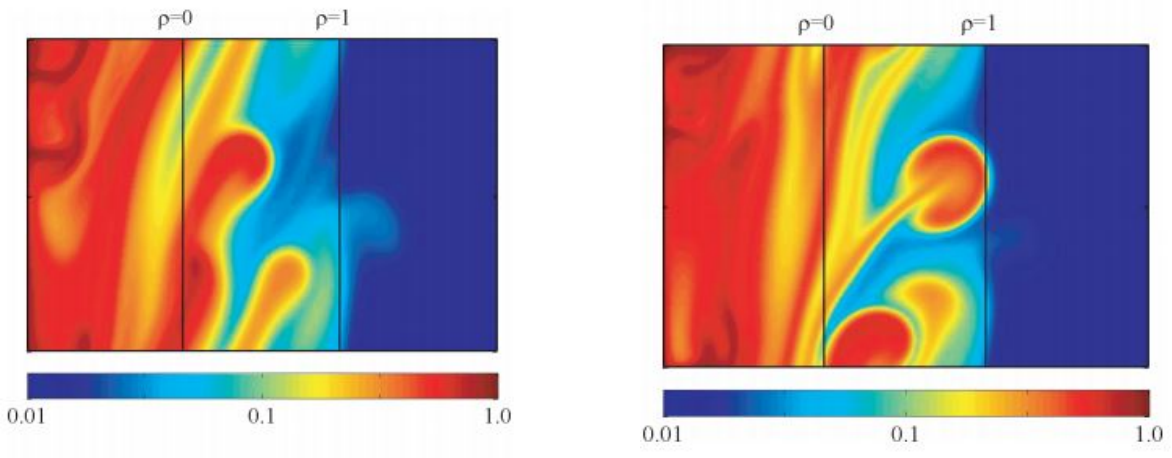

Figure 2.3: Motion of blob-like structures in the particle density from two-dimensional turbulence simulations. The vertical line labeled ρ = 0 corresponds to the last closed flux surface while the line labeled ρ = 1 corresponds to the wall radius

High-speed high-spatial-resolution data obtained by the gas puff imaging GPI diagnostic on the National Spherical Torus Experiment [27] also give a insight on blob birth and transport, suggesting that the blob birth zone is related to the location of the underlying edge instabilities, which can be seen from Figure 2.4 :

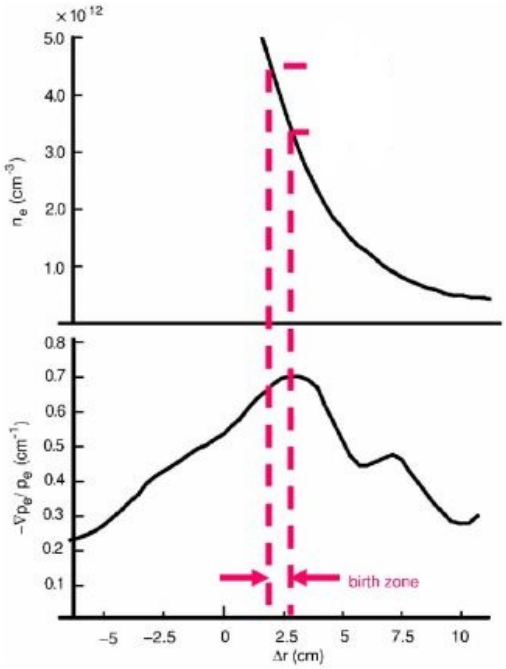

Figure 2.4: Density and normalized pressure gradient vs distance from the separatrix

Blob structures seem to be created with a density and temperature characteristic of the background plasma in that region.

The convection of blobs has directly been observed in D-IIID tokamak using beam emission spectroscopy, showing a poloidal velocity for these structures about two times higher than the radial velocity (0.5-2km/s)[10]. Measurements at DIII-D also have shown that blobs are formed near the LCFS, with the separatrix/open field lines being involved in the generation of such structures. Investigations in QUEST concluded that large scale blob-like structures are intermittently detected at the plasma edge region, interacting with the walls surface because their long life time, despite being events of small frequency [28].

In magnetically confined plasmas, a clear reduction in transport occurs in the presence of self generated transport barrier. This phenomena is associated with a shear layer with localized steepening of gradients of density, temperature and improved confinement. The generation of H-mode confinement regimes seems to be closely related to poloidal shear flows, which tend to suppress turbulence and transport. Understanding the generation mechanism of these flows presents itself with extreme importance in thermonuclear fusion. When a coherent mesoscale structure is placed in laminar background flow whose speed is transverse to the flow direction, it gets stretched and distorted, losing its coherence[29]. The eddy coherence length is the distance over which the eddy flows remain correlated, while the eddy lifetime is the rotation period, usually called eddy turnover time. In the presence of a shear flow, where the rate of shear advection exceeds the eddy lifetime, the eddy turnover occurs faster, with a decrease in eddy lifetime. Eddy scales are reduced with a decrease in the correlation time, which leads to a reduction in turbulence. The loss of correlations comes from the nonlinearity of turbulent

advection, with the temporal evolution of the flow given by the Navier-Stokes equation:

$$\left[\frac{\partial u}{\partial t} + (u.\nabla)\, u\right] = -\frac{1}{\rho}\nabla p + \mu\nabla^2 u \tag{2.8}$$

with ρ the mass density, μ the kinematic velocity, u the flow field and p the pressure. The evolution of the flow is governed by two forces, a dissipative force represented by the viscous term and the inertial force represented by the advective term, that describes the self advection of the flow. The time scale for the inertial force is given by :

$$\frac{1}{\tau_e} = \frac{u}{l} \tag{2.9}$$

where l is the length scale and u the characteristic flow scale.

2.1.2 Vorticity

A turbulent flow is also characterized by the vorticity. Considering a small fluid element, moving and deforming during an infinitesimal period of time δt. Each element of fluid undergoes a tiny displacement $\xi = v\delta t$. The gradient of that displacement can be decomposed into expansion, rotation and shear, with the vectorial angle of rotation given by:

$$\phi = \frac{1}{2}\nabla \times \xi \tag{2.10}$$

The time derivative of the vectorial angle , which is the fluids element's rotational angular velocity can be expressed as:

$$\frac{d\phi}{dt} = \frac{1}{2}\frac{d\xi}{dt} = \frac{1}{2}\nabla \times v \tag{2.11}$$

where $\vec{v}$ is the flow velocity and ∇ the Laplace operator. Hence, the vorticity is twice the angular velocity of rotation of a fluid element.

$$w = \nabla \times \vec{v} \tag{2.12}$$

Replacing the flow velocity by the fluctuations of the $E \times B$ velocity :

$$\vec{v}_{E\times B} = \frac{\vec{E} \times \vec{B}}{B^2} \tag{2.13}$$

and approximating the electric field to the electrostatic fluctuation, the vorticity can be written as:

$$\tilde{w} = \frac{\partial v_\theta}{\partial r} - \frac{\partial v_r}{\partial \theta} = \frac{1}{B}\nabla^2\tilde{\phi} \tag{2.14}$$

where $\nabla^2\tilde{\phi}$ corresponds to the Poison equation, v_r and v_θ are given by equation 2.5 and 2.6 respectively.

Vorticity is a vector field that gives a microscopic measure of the rotation at any point in the fluid. Vorticity in fluids is similar to angular momentum in solids. A simple way to visualize vorticity is seeing a tiny continuum zone as a solid, ignoring the rest of the flow. If that region is rotating, a movement that is not related to just moving along with the flow, then there is vorticity on the flow. A visual representation is shown in Figure2.5.

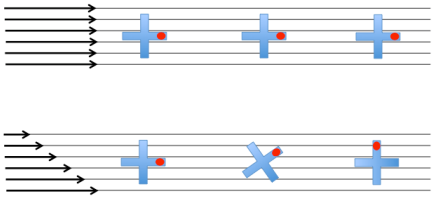

Figure 2.5: Flow fields without vorticity (top) and with vorticity (bottom)

Vorticity is a primary physical quantity in terms of plasma dynamics, where most of the knowledge comes from simulations. In this work, vorticity is investigated from a statistical point of view, recurring to data gathered from a specially designed Langmuir probe array. The presence of the electrostatic potential, related to the plasma stream gives a unique advantage in measuring vorticity in plasmas, allowing the direct measure by suitable Langmuir probe arrays. Discretizing Equation 2.14, using a finite difference approximation:

$$\frac{\partial \phi}{\partial x} \approx \frac{\phi(x+h) - \phi(x-h)}{2h} \tag{2.15a}$$

$$\frac{\partial^2 \phi}{\partial x^2} \approx \frac{\phi(x+h) - 2 \times \phi(x) + \phi(x-h)}{h^2} \tag{2.15b}$$

The vorticity can be then written as:

$$\tilde{w} = \frac{1}{B}\left(\frac{\tilde{\phi}(x+h) - 2 \times \tilde{\phi}(x) + \tilde{\phi}(x-h)}{\Delta x^2} + \frac{\tilde{\phi}(y+h) - 2 \times \tilde{\phi}(y) + \tilde{\phi}(y-h)}{\Delta y^2}\right) \tag{2.16}$$

Where the first term on the right hand side of Equation 2.16 is related to x coordinates of the probe and the second to the y coordinates.

The vorticity flux can be calculated from the relation between the vorticity and the radial $E \times B$ velocity component:

$$\Gamma_w = \langle \tilde{v}_r . \tilde{w} \rangle \propto \frac{\left\langle -\tilde{E}_\theta . \tilde{w} \right\rangle}{B} \tag{2.17}$$

with the radial velocity component given by 2.5.

Studies in fluids already measured three dimensional vorticity [30][31], coherent structures[32], turbulent energy and temperature dissipation rates[33].

Some vortex observations where already made in Argon plasmas at *HYPER-1* [34][35][36], using directional Langmuir probes [37] to measure the flow vector field. Vorticity measurements were also performed at Large Plasma Device (UCLA) with a 7-tip Langmuir probe for characterization of the vortices in the Kelvin-Helmholtz instability and characterize coherent structures driven by near steady-state shear flows [38][39].

2.1.3 Reynolds Stress

The data gathered from the Langmuir probe array also allows measuring other turbulent characteristics like the Reynolds stress. A turbulent flow is defined as the flow in which the system's inertial forces are

dominant over the viscous forces. This phenomenon is described by Reynolds number that determines when the turbulent flow will occur. Assuming a that the velocity of a flow as a typical magnitude of $|v| \approx U$ over a region of size L. The magnitude of the first-order spacial derivatives of the velocity can be expressed as $|\nabla v| \approx U/L$, and the second order derivatives by $|\nabla^2 v| \approx U/L^2$. The Reynolds number becomes[40]:

$$Re \approx \frac{|(v.\nabla)v|}{|v\nabla^2 v|} \approx \frac{U^2/L}{\nu U/L^2} = \frac{UL}{\nu} \tag{2.18}$$

with ν the kinematic viscosity.

In the context of fusion, the Reynolds stress may give a measure of the self-consistent flow generation in plasmas by the small-scale turbulent fluctuations[41], responsible for the generation of radial electric fields. It is suggested that the radially varying Reynolds stress may play an important role in the generation of sheared poloidal flows[42][43].

Starting from the incompressible momentum balance equation:

$$\frac{\partial v_\theta}{\partial t} + \nabla_r(v_r v_\theta) = -\frac{1}{\rho}\nabla_\theta P + \frac{1}{\rho}(\vec{j} \times \vec{B})_\theta \tag{2.19}$$

Averaging over a magnetic surface, neglecting the contributions from magnetic fluctuations the right-hand side cancels:

$$\frac{\partial v_\theta}{\partial t} + \nabla_r(v_r v_\theta) = 0 \tag{2.20}$$

writing the flow as the sum of a mean and a fluctuating part $v = \vec{v} + \tilde{v}$, and using mean time average values, the momentum balance equation:

$$\frac{\partial \vec{v}_\theta}{\partial t} + \nabla_r \langle \tilde{v}_r \tilde{v}_\theta \rangle = 0 \tag{2.21}$$

with the Reynolds stress (Re) approximated by:

$$Re \approx \langle \tilde{v}_r \tilde{v}_\theta \rangle \tag{2.22}$$

The velocity terms of the Reynolds stress tensor are related to the $E \times B$ velocity $\langle \tilde{v}_r \tilde{v}_\theta \rangle \propto \left\langle \tilde{E}_r \tilde{E}_\theta \right\rangle$, where $\tilde{E}_r$ and $\tilde{E}_\theta$ are the radial and poloidal components of the electric field respectively. The Reynolds stress can then be rewritten as follows:

$$Re \propto \frac{1}{B^2} \left\langle \tilde{E}_r \tilde{E}_\theta \right\rangle \tag{2.23}$$

A non-zero value of the gradient Reynolds stress can drive a laminar flow. The correlation needed between v_r and v_θ (or in the electric field components) occurs naturally in the presence of a background gradient driving turbulent transport. Evidence of the importance of Reynolds stress in fusion was found in ISTTOK, using a Langmuir probe array [44], with the vortex structures being able to transport particles, carry polarization charge and organize large-scale potential differences with induction flows perpendicular to the background density gradient [9].

2.1.4 Effects of polarization on SOL transport

The influence of polarization on global and edge plasma parameters is described in previous studies at ISTTOK tokamak [45, 46].

Although both negative and positive bias reveals a large radial electric field induced by the emissive electrode and a substantial increase in plasma density, improvements in confinement are mostly observed for a negative induced bias [45]. Positive polarization seems to be related to large-amplitude fluctuations which lead to low shear induced in the edge region. These large amplitude fluctuations are suggested as the cause for the distinctive behavior between the positive and negative biasing on plasma confinment. The current bias can be induced directly at the limiter, by emissive electrode biasing or negative biased cold electrodes. The current collected by cold electrodes in small tokamaks is not sufficient to change the plasma potential due to the limitation imposed by the ion saturation current. Emissive electrodes allow producing a much larger current and will be used during this work as they are a more efficient strategy to control de edge radial electric field. A movable emissive electrode developed at ISTTOK [47] will be used during this thesis. The emissive electrode consists of a LaB_6 (lanthanum hexaboride) disc covered by a Ta (Tantalum) cylinder, protected by a BN (Borum Nitride) as insulator. The electrode emits steady state current up to 30A, applying a bias voltage between the electrode and the vessel.

The radial electric field is known to play a key role in plasma confinement, with a clear correlation between radial electric field changes and reduction of turbulence. The turbulence suppression due to biased induced shear flows was experimentally verified at ISTTOK [46].

The emissive electrode is located 1mm inside the limiter. The statistical analysis is performed shot by shot, with polarization being applied during 2ms during each cycle discharge. Each cycle will have a time interval with a positive bias induced, and a time interval without bias induced. The results for the vorticity, Reynolds stress and transport are compared.

The polarization is controlled with a dsPIC, connected to the tokamak acquisition system and the electrode that will perform the polarization. The dsPIC receives a trigger, a optic fibers signal, from the real time control system. This trigger gives the dsPIC the information that the plasma cycle just started and starts a timer. After 15 milliseconds, the dsPIC send a signal and turn the electrode on, polarizing the plasma. After 2 milliseconds, the dsPIC send a stop signal and turn the electrode off. The dsPIC goes on a ”wait” state, until receives another trigger. The process is repeated for all cycles.

2.1.5 Statistical description

Probability density function (PDF) methods are well suited to analyze turbulent flows. A probability density function describes the relative likelihood for a random variable X to take on a given value. For a continuous distribution, the probability of X having a value in the interval (i,j) is the area under the PDF in that interval.

In a statistics, moments are parameters of the PDF, used to understand the various characteristics of a frequency distribution, in a concept closely related to moments in physics.

The nth order moment of a probability density function f(x) is defined by:

$$m_n = \langle x^n \rangle = \int_{-\infty}^{\infty} dx\ p(x) x^n \tag{2.24}$$

The first moment, m_1 corresponds to the central tendency of the observations, usually called the average value or mean. For a set of N observations of a random variable x, the mean is given by:

$$\mu = \frac{1}{N} \sum_{i=1}^{N} x_i \tag{2.25}$$

Moments are usually taken about the mean. These so called central moments μ_n are defined as:

$$\begin{aligned} \mu_n &= \langle (x-\mu)^n \rangle \\ &= \int_{-\infty}^{\infty} dx\ (x-\mu)^n p(x) \end{aligned} \tag{2.26}$$

The second central moment μ_2 is commonly know as the variance of the distribution, denoted by σ^2. The variance measures the spread of the observations from the average value, and its defined as:

$$\mu_2 = \sigma^2 = \int_{-\infty}^{\infty} dx\ (x-\mu)^2 p(x) \tag{2.27}$$

For a random variable vector A made up of N scalar observations, variance can be redefined as:

$$\sigma^2 = \frac{1}{N-1} \sum_{i=1}^{N} (x_i - \mu)^2 \tag{2.28}$$

Some definitions of variance use a normalization factor of N instead of $N-1$. The presented alternative was used to obtain an unbiased estimator for σ^2. A more intuitive quantity is the square root of the variance, the standard deviation:

$$\sigma = \sqrt{\frac{1}{N-1} \sum_{i=1}^{N} (x_i - \mu)^2} \tag{2.29}$$

The third central moment, often called skweness measures the degree of asymmetry of a a distribution. A distribution that is symmetrical about its mean has 0 skweness, a positive value indicates that the distribution is skewed to the right, and a negative to the left:

$$\mu_3 = \left\langle (x-\mu)^3 \right\rangle \tag{2.30}$$

It is convenient to analyze this quantity scaled with the third power of the standard deviation, the coefficient of skweness:

$$s = \frac{\mu_3}{\sigma^3} = \frac{\frac{1}{N} \sum_{i=1}^{n} (x_i - \mu)^3}{\left(\sqrt{\frac{1}{N-1} \sum_{i=1}^{N} (x_i - \mu)^2} \right)^3} \tag{2.31}$$

It was shown that the probability distribution function (PDF) for the density fluctuations was positively skewed, which is consistent with large density structures propagating radially across the SOL in walls

direction[22].

The fourth central moment, also known as kurtosis measures the heaviness of the tails in the distribution. The kurtosis coefficients is given by:

$$k = \frac{\mu_4}{\sigma^4} \tag{2.32}$$

A positive kurtosis indicates that the distribution tails are heavier than in a normal distribution. A normal Gaussian distribution has a kurtosis of three. Usually, this moment is subtracted by three, the excess kurtosis due to the easy comparability with the Gaussian distribution.

From previous studies, data seems to suggest that vorticity follows a Q-Gaussian distribution, a specific form of Tsallis distribuition. The Q-Gaussian represents a continuous statistical distribution, supported over the interval $(0, \infty)$, defined by three parameters, a the normalization, λ called the scale parameter and a real number $q < 2$, which determine the behavior of the probability density function:

$$R_q(x) = a\left[1 + (q-1)\frac{x^2}{\lambda^2})\right]^{-\frac{1}{1-q}} \tag{2.33}$$

The results are compared to the histogram of the data. The histogram bin width is defined using the Freedman-Diaconis rule [48], that is designed to minimize the difference between the area under the empirical PDF and the area under the theoretical PDF. The general equation for the bin width is:

$$Binwidth = 2\frac{IQR(x)}{\sqrt[3]{n}} \tag{2.34}$$

where n is the number of observations in the sample x and $IQR(x)$ is the interquartile range, a measure of variability based on dividing the data set into quartiles.

The root mean square is used as evaluation criterion, allowing to plot error bars representing the mean squared deviation of a signal from a given baseline or fit. For a set of n values of a distribution can be written as:

$$x_{RMS} = \sqrt{\frac{1}{N}\sum_{n=1}^{N} {x_n}^2} \tag{2.35}$$

Despite very different geometry, the normalized PDF results are usually very similar in the linear and toroidal devices, implying a common origin for the convective transport[22].

2.1.6 Poloidal phase velocity

The experiment also involves computing the plasma poloidal phase velocity. Spatial Fourier transforms allow to compute quantities like the wave vector *k*, coherence between signals and even the phase velocity of these fluctuations near specific positions.

The presented method computes the plasma velocity with *S(k,w)* as the local wavenumber and frequency spectral density, estimated from two fixed probes[49]. The technique involves sampling the cross power spectrum from the probes separated at a known distance and reconstruct the wave number

frequency plane, which can be integrated to obtin the spatial spectrum[50].

Dividing the signal from each probe in intervals of length L, corresponding to a time interval T, and performing a *Fast Fourier Transform* allows the computation the sample discrete Fourier series coefficients:

$$\Phi^j(x,\omega) = \frac{1}{N}\sum_{l=1}^{N}\phi(x, l\Delta t)exp(-i\omega l\Delta t) \tag{2.36}$$

The sample cross power spectrum is not used directly, but it allows to compute the relationship between two time series as a function of frequency. The cross power spectrum is presented in a two-sided complex form and can be computed as:

$$H^j(\chi,\omega) = \Phi^{j*}(x_1,\omega)\Phi^j(x_2,\omega) \tag{2.37}$$

with χ the distance between the probes.

The phase angle can then be obtained :

$$\Theta^j(\omega) = tan^{-1}\left[\frac{Img[H^j(\chi,\omega)]}{Re[H^j(\chi,\omega)]}\right] \tag{2.38}$$

The sample local wavenumber is given by:

$$K^j(\omega) = \frac{\Theta^j(\omega)}{\chi} \tag{2.39}$$

The sample power value $S^j(w)$ from probe *n* is defined using the Fourier series coefficients of the signal, as introduced in Equation 2.36 and its conjugate:

$$S_n^j = \Phi^{j*}(x_1,\omega)\Phi^j(x_1,\omega) \tag{2.40}$$

Which allows to compute the local wavenumber and frequency spectrum $S_l(k,w)$ as the sum of the sample power values at a fixed frequency and with wavenumber in the range K to $K+\Delta K$ divided by the number of records:

$$S_l(k,w) = \frac{1}{M}\sum_{j=1}^{M} I_{0,\Delta K}[K - K^j(w)]\frac{1}{2}[S_1(w) + S_2(w)] \tag{2.41}$$

The averaging of the two sample powers introduces more statistical value. An example of the 2D map from a recent study at ASDEX[50] on strong plasma edge turbulence can be seen at Figure 2.6

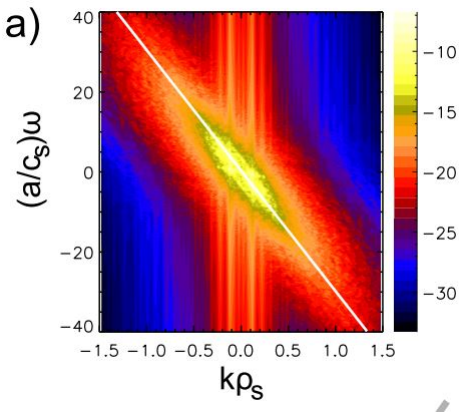

Figure 2.6: Wave number frequency power spectrum S(K,W) for density fluctuations[50]

The function $I_{0,\Delta K}$ at 2.41 correspond to an algorithm that computationally can be implemented as a weighted histogram where the bins are defined with the Freedman–Diaconis rule[48] to select the optimal bin width. A detailed presentation of the algorithm is presented in Chap. 3.

The poloidal phase velocity, which can be seen as a integration of the wavenumber-frequency plane, can finally be computed as:

$$v_{phase} = \frac{\sum S(k,w)(w/k)}{\sum S(k,w)} \tag{2.42}$$

Using data from two probes, varying its radial position allow to determine the radial variation of the poloidal phase velocity.

The poloidal phase velocity results obtained from the wavenumber and frequency spectra method will be compared with another procedure, recurring to correlation relations.

The cross-correlation is a measure of similarity of two time series as a function of the displacement of one relative to the other, given by:

$$G_{xy}(\tau) = \int_0^t x(t)y(t+\tau)dt \tag{2.43}$$

The cross correlation maximum indicates the point in time where the signals have a synchronous pattern, with the time delay between two signals determined by:

$$\tau_{delay} = arg\ max((f \star g)(t)) \tag{2.44}$$

In this case, the correlation is calculated between floating potentials acquired on a Langmuir probe.

Correlation techniques are widely used in plasma physics and allow to analyze several parameters as [51]:

- Calculate averages on unstable plasmas. Correlation measurements may be used effectively for averaging the signal reducing the effect of the noise, which allows obtaining quantities like mean square amplitude or the phase between two signals. The measurement of the phase between signals is particularly useful for obtaining the phase velocity of an oscillation.

- Statistics in turbulent plasmas. Correlation measurements are fundamental to the study of turbulent plasma. Turbulence is a complicated process, and the little understanding there is lies in statistical analysis. Measurements of the statistical characteristics of turbulence as correlation times and lengths and their relation with other plasma parameters are essential to further progress studies in turbulence.

- Comparisons between signals. Correlation techniques allow determining whether and to what extent different signals are related.

In this method, the poloidal phase velocity of the turbulent plasma is determined through two poloidally separated pins. Here the two-point cross-correlation between the two probes signals is calculated. The poloidal phase velocity is determined with the ratio of the mutual distance of two poloidally separated probes ΔX over the time delay of the signal $\Delta t = \tau_{delay}$. The velocity comes as $V = \frac{\Delta X}{\Delta T}$. The cross-correlation function determines the time that fluctuations take to propagate from one probe to another.

This technique is very powerful as averaging techniques, for measuring phase velocities, $E \times B$ drifts and the qualitative study of statistical effects. Although the method presents itself with some limits:

- The resolution of the analysis is defined by the sampling frequency of the acquisition system.

- The maximum velocity that can be calculated is limited by the distance between the probes.

2.1.7 Correlation length

The cross correlation is a measure of similarity of two series as a function of the displacement of one relative to the other, given by:

$$G_{xy}(\tau) = \int_0^t x(t)y(t+\tau)dt \tag{2.45}$$

In this case the correlation is obtained from electric potential signals deduced from floating potentials detected on a Langmuir probe.

With the coherence between two signals x(t) and y(t) defined as a real-valued function:

$$C_{xy}(\tau) = \frac{|G_{xy}(f)|^2}{G_{xx}(f)G_{yy}(f)} \tag{2.46}$$

with G_{xx} and G_{yy} the auto correlation relations, we can define the correlation length *L* as the $\frac{1}{e}$ Gaussian half-width as:

$$C_{xy}(f) \approx e^{\frac{-\Delta r^2}{L}} \tag{2.47}$$

with Δr the distance between the probes on the array. The radial correlation length of the turbulence was already measured with different diagnosis, the most common being standard correlation reflectometry. The measure of the correlation length is fundamental, leading to a better understanding of the spatial size of the turbulent perturbations. Many efforts have been made already in order to understand the relation between the radial electric field E_r, shear $\frac{\delta E_r}{\delta r}$ and correlation length [52][53].

2.1.8 Langmuir probes

Langmuir probes are a powerful tool widely used in experimental plasma physics studies, not only due to the simplicity associated with the method of operation but also because it allows measuring plasma parameters and temporal fluctuations in different positions simultaneously.

The Langmuir probe consists of a conducting filament inserted into plasma and electrically biased with respect to a reference electrode. The purpose of the probe is to collect electron/ion currents. A probe that is electrically floating collects no net current from the plasma, and thus its potential rises and falls to whatever potential is necessary to maintain zero net currents. The plasma potential is the potential with respect to the walls of the device V_p and not the potential on the probe relative to the electrodes. This last potential is called floating potential V_f, and it is related to the plasma potential V_p by:

$$V_p = V_f + \Lambda T_e \tag{2.48}$$

where:

$$\Lambda = log\sqrt{\left[\left(2\pi\frac{m_e}{m_i}\right)\left(1+\frac{T_i}{T_e}\right)\right]} \approx 3 \quad \text{(for hydrogen)} \tag{2.49}$$

Langmuir probes also allow measuring quantities like temperature and electron density. An array of probes with multiple pins allow measurements of other important plasma parameters such as radial and poloidal electric fields or electrostatic fluxes that can be used to estimate other relevant quantities like the vorticity or Reynolds stress mentioned above.

The interpretation of the Langmuir probe characteristics can be difficult, with the current collected by the probe consisting of a combination of ion and electron current from the plasma and secondary electron current produced by the electron, ion or photon bombardment on the probe. The difficulty also arises from the fact that probes are boundaries to a plasma, and near the boundary, the equations governing the motion of the plasma change their characteristics. In particular, the condition of quasineutrality is not valid near the boundary.

Electrons with smaller mass relative to the positive ions, have significantly higher thermal speeds, with the electrons usually having higher temperatures. This speed difference turns into an initial higher electron current on the probe with the electrons reaching the probe faster than the ions. Since the net current to the floating probe must be zero, the probe floats to a negative potential relative to the plasma which leads to an increase of ion current, with the floating potential becoming smaller than the plasma potential. The region where the plasma and the probe interact is called the Debye sheath. This sheath is a layer in the plasma characterized by an overall excess positive charge with an electron shielding cloud surrounding it, limiting the effect of the local potential on the bulk plasma. The thickness of such a layer is on the order of electron Debye length λ_{De}.

$$\lambda_{De} = \left(\frac{\epsilon_0 k T_e}{e^2 n_e}\right)^{\frac{1}{2}} \tag{2.50}$$

The electron current per unit area to a planar probe biased at V_B can be calculated as:

$$j_e(V_B) = e \int f(x,v,t) v_z dv_x dv_y dv_z \tag{2.51}$$

where $f(x,v,t)$ is the velocity distribution of the electrons.

As previously mentioned, a sufficiently negative bias voltage on the probe V_B with respect to the plasma potential V_P collects positive ions until the bias voltage reaches V_P. At this point, the positive ions start getting repelled. On other hand, for $V_B >> V_P$, the probes collect electron saturation current I_{es}. For nondrifting Maxwellian electron, the velocity distribution $f(x,v,t)$ its given by:

$$f(x,v,t) = ne\sqrt{\left(\frac{m_e}{2\pi T_e}\right)^3} exp\left[-\frac{m_e v^2}{2T_e}\right] \tag{2.52}$$

The expression for the probe current as function of V_B is given by:

$$I_e(V_B) = \begin{cases} I_{es} exp\left[-e\left(\frac{V_P - V_B}{kT_e}\right)\right] & \text{if } V_B \leq V_P, \\ I_{es} & V_B > V_P \end{cases} \tag{2.53}$$

with I_{es} the electron saturation current that can be obtained by integrating the equation A.9(in Appendix A) and its given by:

$$I_{es} = \frac{1}{4} e n_e v_e A_{probe} \tag{2.54}$$

where $v_e = \sqrt{\frac{8kT_e}{\pi m_e}}$ is the electron thermal speed, m_e the electron mass and n_e the plasma electron density. In the case of fusion plasmas, the ions temperature on plasma T_i is of the same order of magnitude of the electron temperature T_e, so the ion saturation current is given by the equation 2.54, where the electron's charge e should be replaced by i. In the case of $T_i << T_e$ this expression is not valid and the current is determined by the electron temperature, given by:

$$I_{is} = 0.5 e n_i \sqrt{\frac{kT_e}{m_i}} A_{probe} \tag{2.55}$$

The reason for this electron's temperature dependence lies in the formation of a sheath around the negatively biased probe, as explained before. The full derivation of the results can be seen at Appendix A. A Langmuir probe diagnosis has some limitations from being an intrusive method. The diagnosis is limited by the plasma temperature, being more suitable for cold plasmas and measures in the edge plasma $< 100eV$, the case that will be explored in this thesis.

Chapter 3

Implementation

3.1 ISTTOK tokamak

ISTTOK is a small tokamak with a circular cross-section, a poloidal graphite limiter and an iron core transformer[54].

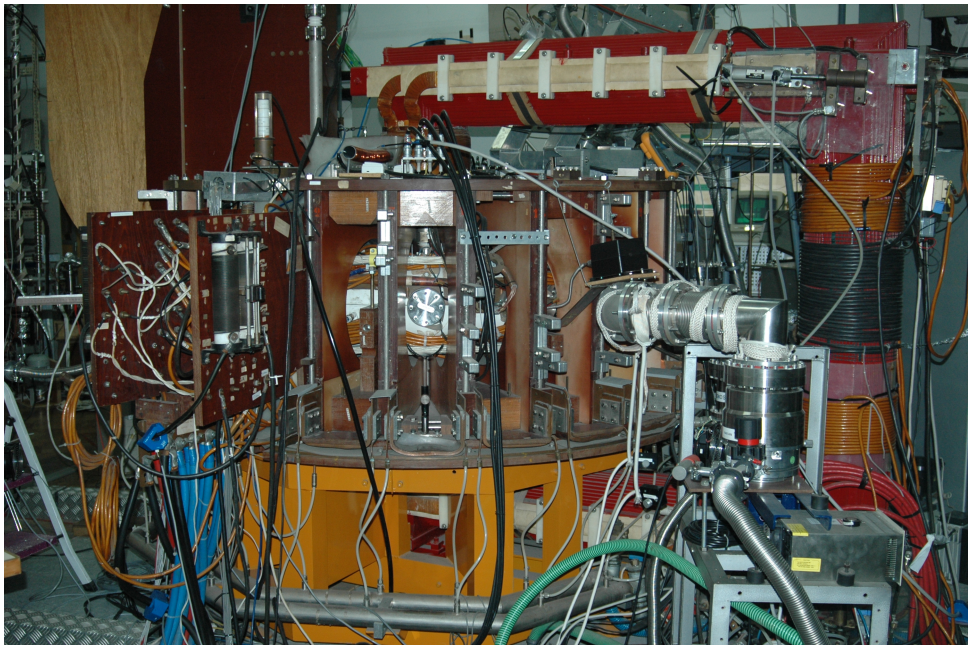

Figure 3.1: ISTTOK tokamak at IPFN

Small tokamaks like ISTTOK, have been proved as a flexible and quick way to test new ideas, with many experiments leading to advanced concepts, now being pursued in major tokamaks[55]. Previous measurements show that properties and parameters of the edge plasma are similar between large and small tokamaks, emphasizing the importance of the study of density and potential fluctuations in such devices, that play a key role in the overall confinement conditions. Small tokamaks provide active support for large tokamak programs like ITER, the world's largest fusion experiment.

ISTTOK main parameters are listed in table 3.1

Parameter	***Values***
Major radius	46 cm
Minor radius	8,5 cm
Maximum toroidal magnetic field	2.8 Tesla
Transformer flux swing	0,25 Vs
Plasma current	$\sim$7 kA
Discharge duration	$\sim$45 ms
Plasma density at r=0	5*10^{18} m^{-3}
Electron temperature at r=0	$\sim$120 eV
CIII ion temperature at r=0	$\sim$100 eV
Energy confinement time	$\sim$0.8 ms
Beta at r=0)	$\sim$0.6%
Safety factor	q(0) $\sim$1 q(a) $\sim$5

Table 3.1: Main parameters of ISTTOK

The tokamak is equipped with several diagnostics systems, as shown in Figure 3.2 that help carry out the scientific program.

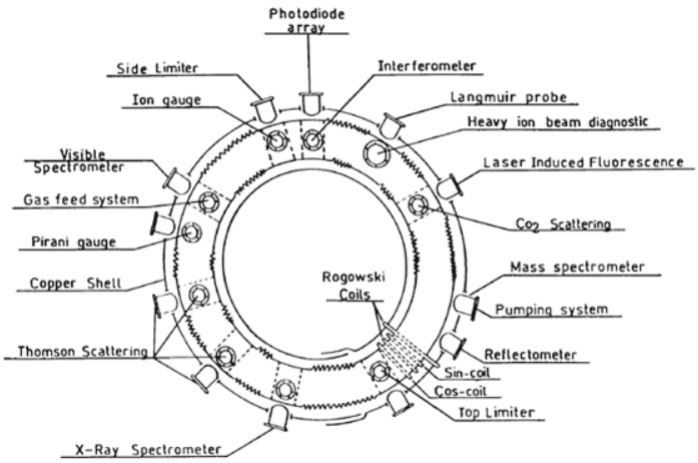

Figure 3.2: Main ISTTOK diagnostics

The Langmuir probe array used will be inserted in the equatorial plane. The density is acquired through interferometry and the plasma position is inferred with the help of four probes(two measuring the vertical position and two measuring the horizontal).

ISTTOK provides more than 100 acquisition channels and a real time control of the plasma current magnitude and centroid position, retrieved by a twelve Mirnov coil poloidal set, represented in Figure 3.2. [1]

[1] More info at: `https://isttok.tecnico.ulisboa.pt/~isttok.daemon/index.php?title=ISTTOK_-_Wiki`

3.2 Vorticity probe array design/Experimental set-up

As mentioned in Chapter 2, Langmuir electrostatic probes consist of insulated wires exposed to the plasma, a simple and inexpensive diagnostic to analyze tokamak edge plasmas. The design of the multi-pin probe array can have a variety of different arrangements, depending on the problem under study. The diagnostic system was designed on Autodesk Fusion360 and the manufacturing was in charge of Núcleo de Oficinas (NOF) at IST.

Equation 2.15b clearly suggests a design that involves a diamond shape pattern, with three different poloidally located tips at the same radial position and two tips separated radially for the vorticity measurement. Another pin is then needed to obtain the ion saturation current. The schematic of the probe is shown in figure 3.17 and 3.4.

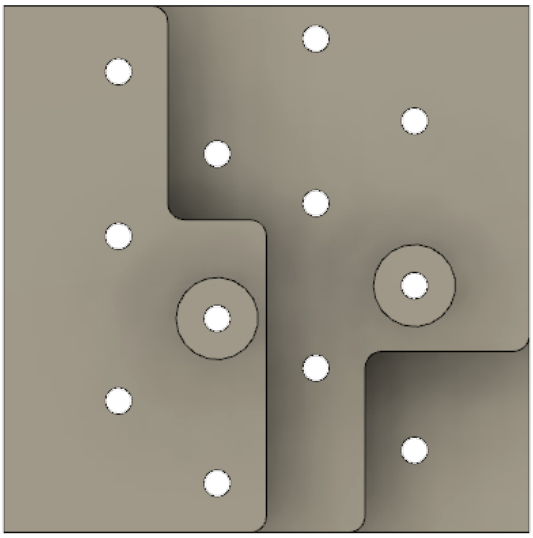

Figure 3.3: Vorticity probe top view.Tungsten filament not included

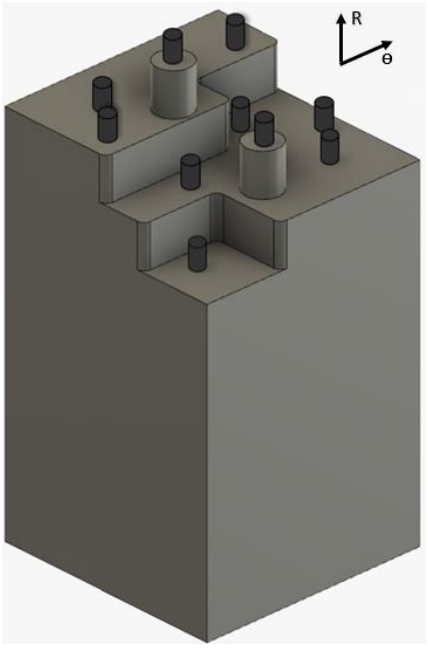

Figure 3.4: Vorticity probe side view.

The probe array was designed to prevent the appearance of shadows between pins. The body of the probe is built in Boron Nitrate, an insolating chemical compound characterized by its hardness (only inferior to diamond), excellent thermal and chemical stability and high conductivity. These features make the material ideal for enduring the hostile ambient inside the tokamak. The probe tips are made of tungsten filaments, a material with remarkable robustness associated with a high melting point [2]. The probe array was designed as small as possible in order to cause the minimum interference with the plasma, with a poloidal separation Δ_θ of 5mm and a radial separation Δ_r of 3mm, as shown in figure 3.17 and 3.4. The tungsten pins have a 0.7mm diameter.

The design of the Langmuir probe array had some challenges due to limitations regarding the available machinery. The machinery could only perform drills with a diameter:length ratio of 1:10. For a diameter of 0.7mm mentioned above, a length of 7mm would not be enough to carve all the pins neces-

[2]Tungsten has the highest melting point of all elements, 3422°

sary on the Boron Nitrate block. The probe also need to have some extra length in order to be coupled to a support system. The solution found is presented in figure 3.5 :

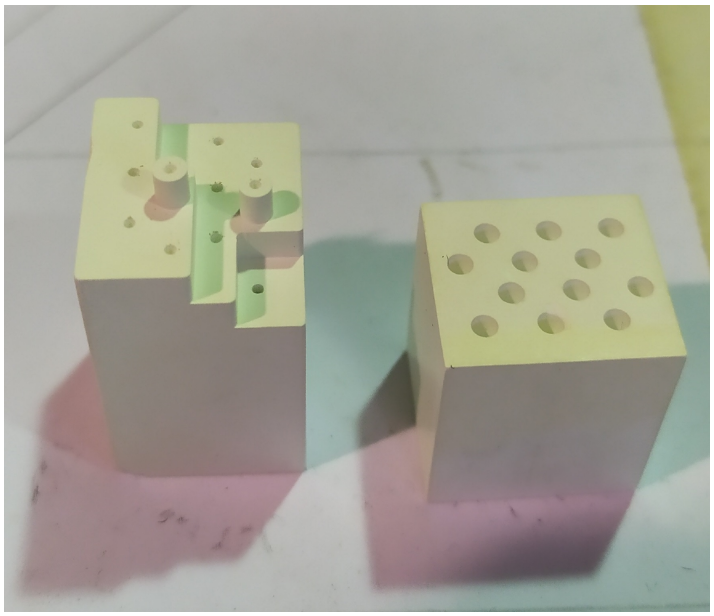

Figure 3.5: Solution to the lack of length on the probe. Two block of Boron Nitrate where drilled. The left block was drilled with the design presented in figures 3.17 3.4. The right one was drilled in the same plane positions but with a diameter of 2mm

The left block was drilled with a 0.7mm diameter from the top and with a 2mm diameter from the bottom. The right one was drilled with a 2mm diameter. Both blocks combined allow to have a probe with 40mm length, enough to the experiment.

Joining the 2 blocks also presented some difficulties. First, the glue had to be resistant to the low pressure tokamak conditions. Second, the blocks had to be joined in such a way that there is no glue exposed to the outside of the probe, which later translates into glue exposed to the plasma and would lead to contamination. The solution to the first problem was to use *Torr Seal*, a epoxy resin specially designed to work on any type of Ultra High Vacuum (UHV) system. Regarding the question of joining the blocks, *Torr Seal* was applied to the holes at the same time as the tungsten filaments where placed. Due to the thickness of the glue, it had a certain resistance, which allows to maintain the right position of the filaments even before curing. The curing process was accelerated placing the probe inside a oven at $100^{\circ}\,C$. The final result is presented in figure 3.6.

Figure 3.6 shows a probe used in previous experiments at ISTTOK. The previous probe had a less complex design, allowing to perform only 1 vorticity computation per shot. Some of the results presented on this thesis will be compared to the ones obtained with that probe. The probe got destroyed during the experimental campaign.

Figure 3.6: Vorticity probe array

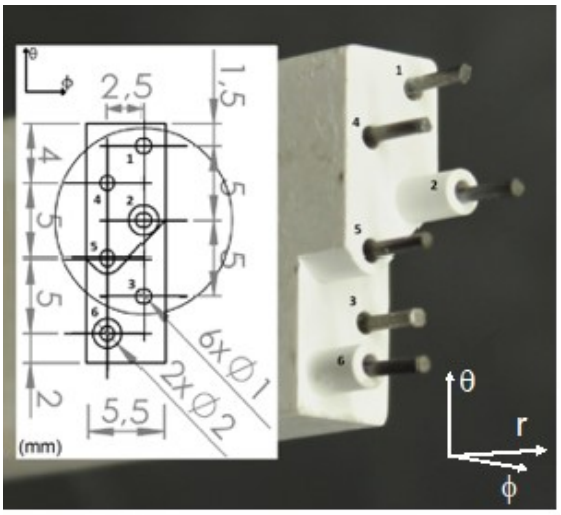

Figure 3.7: Previous vorticity probe array

The pins of the probe are connected to the acquisition system with wires specially designed to the vacuum conditions. Common cable insulation materials could not be used in the tokamak environment, due to the out-gassing phenomena that would negatively affect the vacuum level. The connectors, placed on the ends of the wires, which connect them to the probe pins and the flange are also insulated, preventing contacts between them. This isolation is achieved using a Polymide material, also known as *Kapton*, a thermoplastic material with high temperature and radiation resistant and extremely low out-gassing.

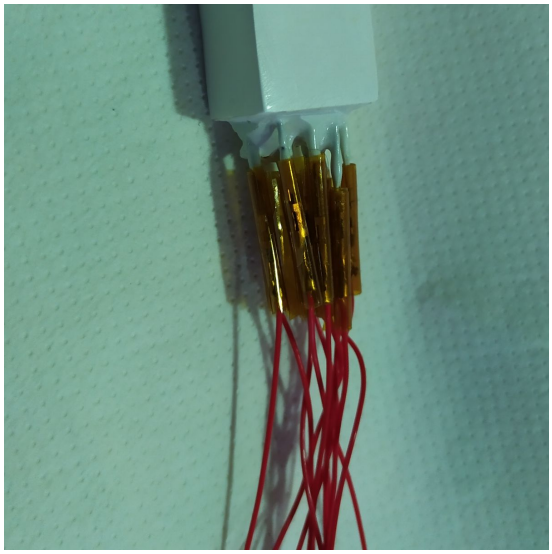

Figure 3.8: Vorticity probe wiring. The *Kapton* assures the isolation between the connectors.

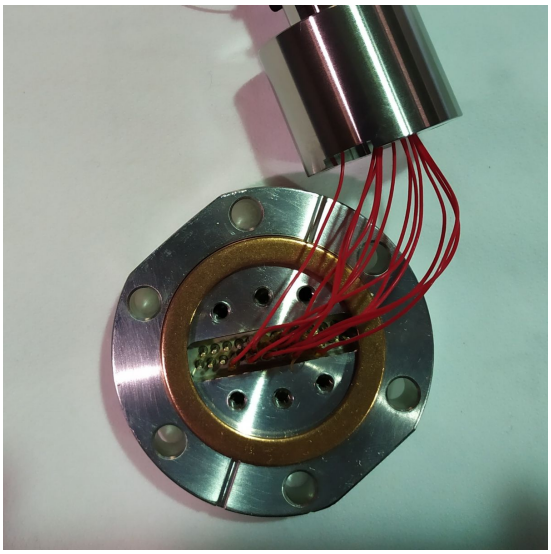

Figure 3.9: Flange wiring.The support structure shown in the figure rests on the o-ring and is then fixed with screws on the flange.

The probe is then connected to a handler by a support structure, also designed during this work. The handler allows moving the probe radially across the Scrape off Layer region. The experimental apparatus is shown in figures 3.10 3.11.

Figure 3.10: Back view of the apparatus.

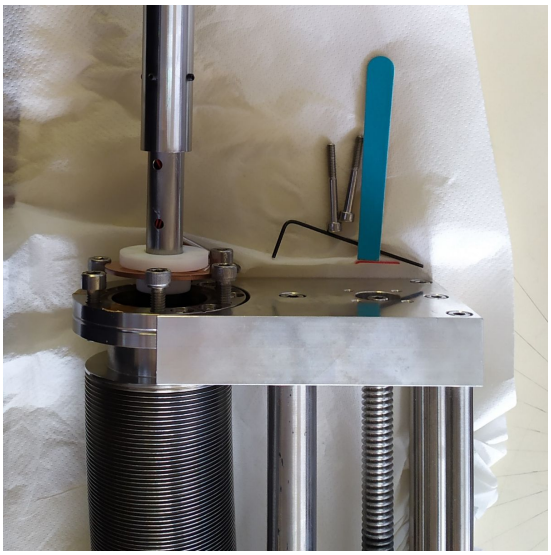

Figure 3.11: Front view of the apparatus.

To ensure a straight position of the probe, a O-ring is placed along the support as shown in figure 3.12.

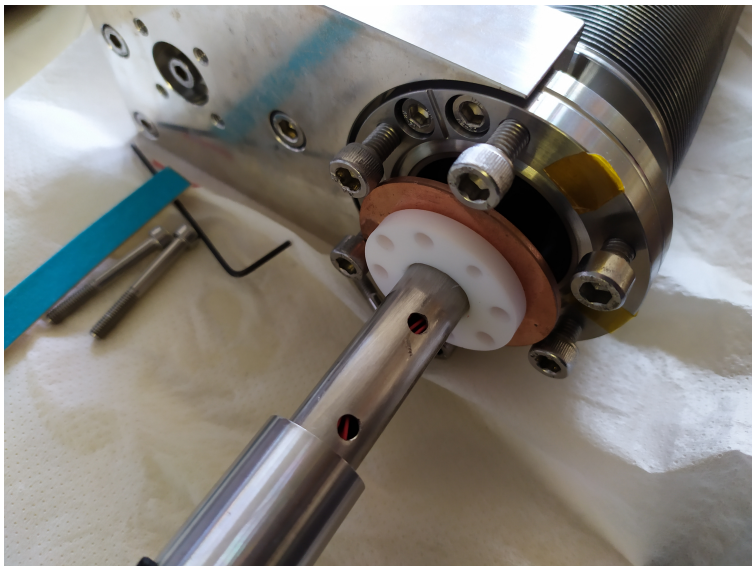

Figure 3.12: O-ring and Teflon apparatus that ensures a straight position of the probe when moving into the tokamak.

All components that will be subjected to a vacuum environment are previously cleaned, using an ultrasound bath to prevent contamination of the environment and problems in the vacuum system.

An experimental setup schematic allows defining the initial position of the probe when the handler is in the ”minimum position”. The probe should be located before the second vacuum valve in order to do changes if needed to the experimental set-up without affecting the tokamak vacuum conditions.

The experiment involves the acquisition of signals to a maximum of $35mm$ depth after the limiter. This maximum value is related with the limitations of the experimental method. Going further into the plasma would expose the probe to temperature conditions that would damage it. With a handler that allows moving the probe $300mm$ from the minimum position. Taking into account the dimensions of the support system (that was designed to be adjustable) and the probe array, the "zero position" of the probe when the handler is in the minimum position is presented in figure 3.13.

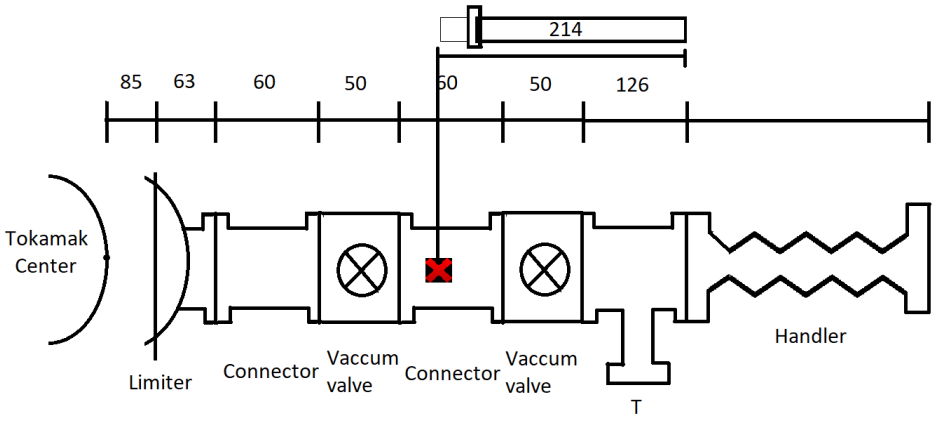

Figure 3.13: Experimental set-up schematic. The distance values are presented in millimeters. The zero position of the probe when the handler is at the minimum position os represented by the red cross

The final experimental set-up is shown if figure 3.14

Figure 3.14: Experimental set-up.

The vorticity probe is tilted with a four degrees angle to match the magnetic field lines orientation of the tokamak.

3.3 Verification and Validation

3.3.1 Vorticity probe

The vorticity probe described previously, acquires floating potentials and ion saturation current signals.

The radial and poloidal electric field can be respectively deduced from the gradient of floating potential signals by the following relations:

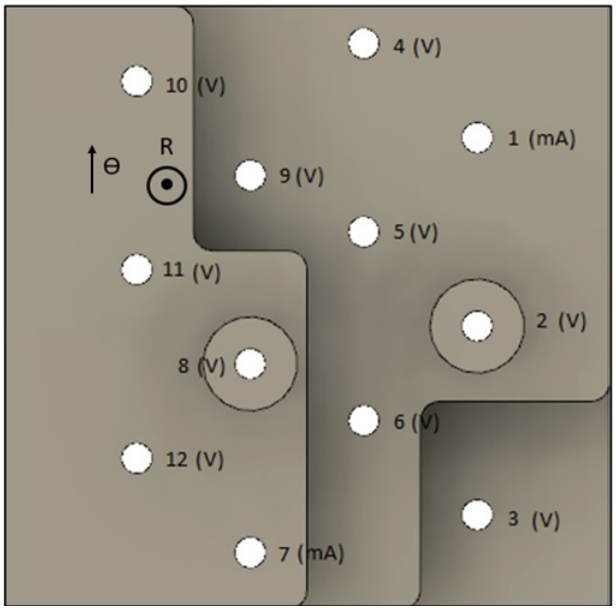

$$\begin{aligned}\tilde{E}_{r1} &= -\frac{\tilde{\phi}_3 - \tilde{\phi}_2}{\Delta r} \\ \tilde{E}_{r2} &= -\frac{\tilde{\phi}_9 - \tilde{\phi}_8}{\Delta r}\end{aligned} \tag{3.1}$$

$$\begin{aligned}\tilde{E}_{\theta 1} &= \frac{\tilde{\phi}_4 - \tilde{\phi}_5}{\Delta\theta} \\ \tilde{E}_{\theta 2} &= \frac{\tilde{\phi}_5 - \tilde{\phi}_6}{\Delta\theta} \\ \tilde{E}_{\theta_{T1}} &= \frac{\tilde{E}_{\theta 1} + \tilde{E}_{\theta 2}}{2} \\ \tilde{E}_{\theta 3} &= \frac{\tilde{\phi}_{12} - \tilde{\phi}_{11}}{\Delta\theta} \\ \tilde{E}_{\theta 4} &= \frac{\tilde{\phi}_{11} - \tilde{\phi}_{10}}{\Delta\theta} \\ \tilde{E}_{\theta_{T2}} &= \frac{\tilde{E}_{\theta 3} + \tilde{E}_{\theta 4}}{2}\end{aligned} \tag{3.2}$$

From equations 2.5 and 2.6, the radial and poloidal velocities due to the $E \times B$ drift can be inferred, and the particle fluxes due to the electrostatic fluctuations, expressed at equation 2.7 can be rewritten as:

$$\begin{aligned}\Gamma_{r1} &\propto < \tilde{n}.\tilde{V}_{E_r} > \propto \frac{\tilde{I}_{sat1}.\tilde{E}_{\theta_{T1}}}{B} \\ \Gamma_{r2} &\propto \frac{\tilde{I}_{sat2}.\tilde{E}_{\theta_{T2}}}{B}\end{aligned} \tag{3.3}$$

assuming that the ion saturation current is proportional to the density fluctuation[56].

The Reynolds stress, stated at equation 2.23 can be formulated as:

$$\begin{aligned}Re_1 &\propto \frac{1}{B^2}\left\langle \tilde{E}_r \tilde{E}_\theta \right\rangle = \frac{1}{B^2}\left(\left\langle \frac{\frac{\tilde{\phi}_4 - \tilde{\phi}_5}{\Delta\theta} + \frac{\tilde{\phi}_5 - \tilde{\phi}_6}{\Delta\theta}}{2} . \frac{-(\tilde{\phi}_3 - \tilde{\phi}_2)}{\Delta r} \right\rangle\right) \\ Re_2 &\propto \frac{1}{B^2}\left(\left\langle \frac{\frac{\tilde{\phi}_{12} - \tilde{\phi}_{11}}{\Delta\theta} + \frac{\tilde{\phi}_{11} - \tilde{\phi}_{10}}{\Delta\theta}}{2} . \frac{-(\tilde{\phi}_9 - \tilde{\phi}_8)}{\Delta r} \right\rangle\right)\end{aligned} \tag{3.4}$$

The floating potential signals allow to calculate the vorticity derived in section 2.1.2:

$$\begin{aligned}\tilde{w}_1 &= \frac{1}{B}\left(\frac{\tilde{\phi}_2 - 2\times\tilde{\phi}_5 + \tilde{\phi}_3}{(\Delta r)^2} + \frac{\tilde{\phi}_6 - 2\times\tilde{\phi}_5 + \tilde{\phi}_4}{(\Delta r)^2}\right) \\ \tilde{w}_2 &= \frac{1}{B}\left(\frac{\tilde{\phi}_8 - 2\times\tilde{\phi}_{11} + \tilde{\phi}_9}{(\Delta r)^2} + \frac{\tilde{\phi}_{10} - 2\times\tilde{\phi}_{11} + \tilde{\phi}_{12}}{(\Delta r)^2}\right)\end{aligned} \tag{3.5}$$

The vorticity result allow to rewrite the vorticity flux expressed at equation 2.17 as:

$$\begin{aligned}
\Gamma_w &= \langle \tilde{v}_r . \tilde{w} \rangle \propto \frac{\left\langle -\tilde{E}_\theta . \tilde{w} \right\rangle}{B} \\
\Gamma_{w1} &= \frac{1}{B}\left(\left\langle \frac{\frac{\tilde{\phi}_4 - \tilde{\phi}_5}{\Delta\theta} + \frac{\tilde{\phi}_5 - \tilde{\phi}_6}{\Delta\theta}}{2} . \frac{1}{B}\left(\frac{\tilde{\phi}_2 - 2\times\tilde{\phi}_5 + \tilde{\phi}_3}{(\Delta r)^2} + \frac{\tilde{\phi}_6 - 2\times\tilde{\phi}_5 + \tilde{\phi}_4}{(\Delta r)^2}\right)\right\rangle\right) \\
\Gamma_{w2} &= \frac{1}{B}\left(\left\langle \frac{\frac{\tilde{\phi}_{12} - \tilde{\phi}_{11}}{\Delta\theta} + \frac{\tilde{\phi}_{11} - \tilde{\phi}_{10}}{\Delta\theta}}{2} . \frac{1}{B}\left(\frac{\tilde{\phi}_8 - 2\times\tilde{\phi}_{11} + \tilde{\phi}_9}{(\Delta r)^2} + \frac{\tilde{\phi}_{10} - 2\times\tilde{\phi}_{11} + \tilde{\phi}_{12}}{(\Delta r)^2}\right)\right\rangle\right)
\end{aligned} \tag{3.6}$$

3.4 Data analysis methods

The tokamak acquisition system stores the data after each shot at IPFN database. Its important to analyze several parameters other than the probe signals itself. The information about the plasma position and orientation inside the tokamak is retrieved through fours probes located at the top, bottom inner and outer position. During each shot its also important to analyze the plasma density since it can change dramatically during each cycle, which can affect the results. Each discharge can have a different number of cycles, and these can be positive or negative depending on the direction of the plasma current applied.

Selecting the right time interval for each radial position is a crucial step in order to get meaningful results. This ”stable region” selection is not always obvious working with 12 probes simultaneously, and must be done carefully.

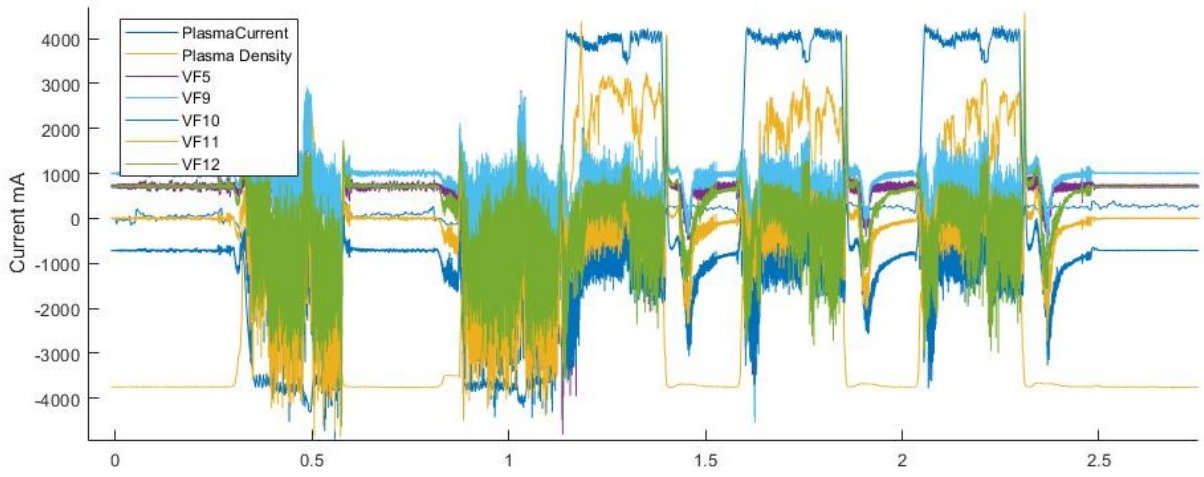

Figure 3.15: Overview of Shot 48967. The signals presented correspond to one saturation current and one floating potential for each probe, density and plasma current.

After defining the interest time interval, the signal must be preprocessed in order to remove the DC offset. Since the offset has a constant value for each probe, removing the signal mean over a time interval without plasma to the original signal gives the intended result.

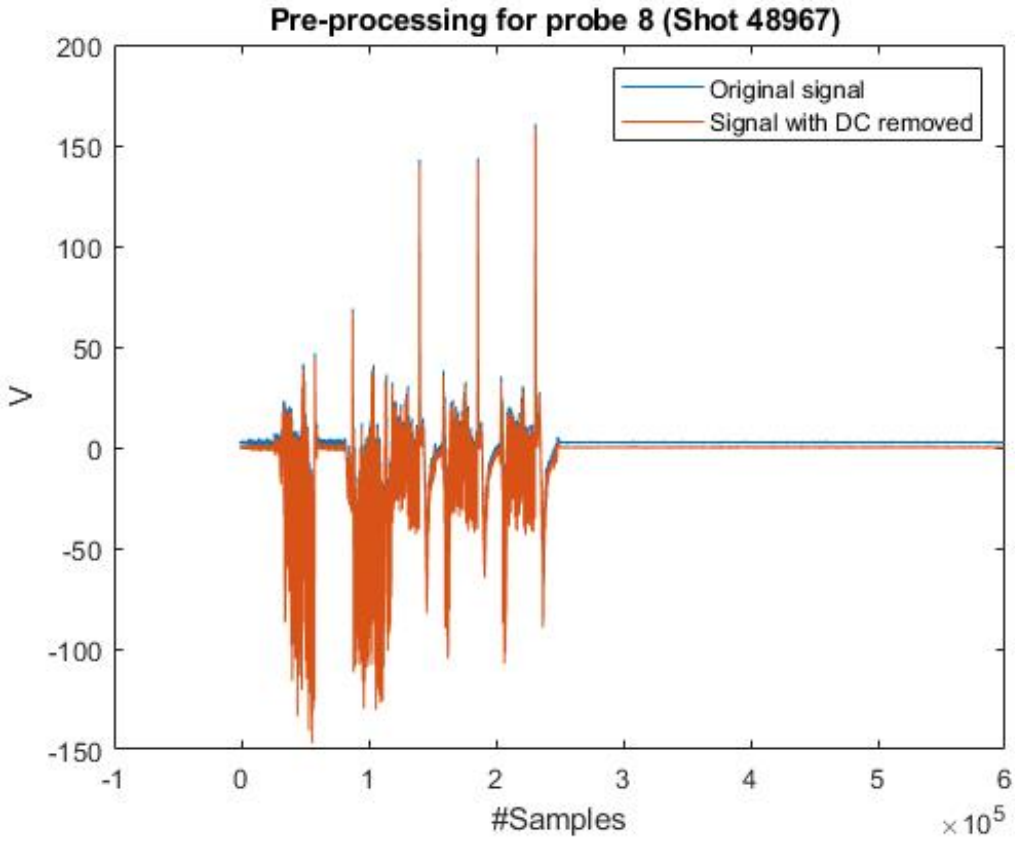

Figure 3.16: Example of a raw signal from probe 8 before and after removing the offset.

Each probe signal for the analysis is the concatenation of selected time intervals for each cycle. Most of the experiments consisted of shots with two negative cycles at the beginning, followed by three positive cycles as in figure 3.15. The analysis presented in this thesis will ignore the data from the first cycle (positive and negative) in each shot since it frequently showed a different behavior relative to the next ones, with results that from a physics point of view do not make sense.

The radial floating potential and ion saturation current profiles, consisting of the signals mean across all the radial positions also provide valuable information before proceeding with the analysis. Outliers in radial profiles, computed with the raw signals, are frequently associated with either pour data selection or with experimental problems during the shot.

After selecting the data, the signals are ready for the statistical analysis that involve the computation of quantities presented in Chap. 2. Each calculation is performed both using the individual signal from each cycle and the concatenated signal of the available cycles.

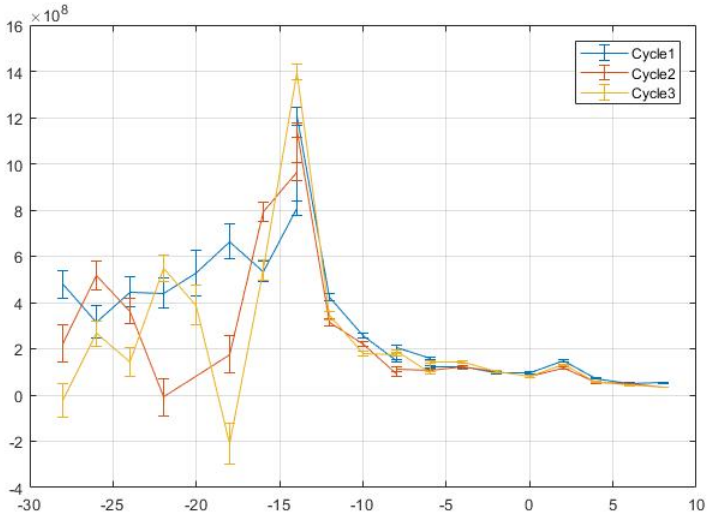

Figure 3.17: Vorticity radial profile example computed at each cycle.

After individually analyzing the cycles, the data is concatenated and processed.

The power spectrum of the vorticity, vorticity flux, Reynolds stress and E×B flux is computed using the already processed signals. The power spectrum analysis start with a spectogram of the signal, using the *spectrogram* function. The parameters for the fast Fourier transform are: a window of 256 data points, with a 50% overlap between sections and a sample rate, the number of samples per unite of time, of $2 \times 10^6 Hz$. The algorithm divides de signal into segments with length equal to the window value and compute discrete Fourier transform, presenting the spectogram of the signal.

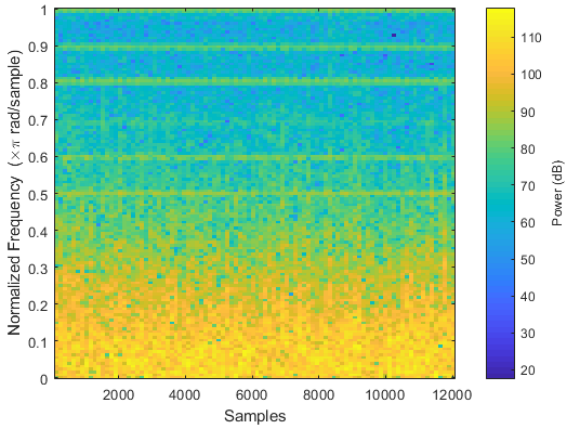

Figure 3.18: Example of a vorticity signal spectogram.

The spectogram is a two-dimensional graph, with the third dimension represented by colors. It is a visual way to represent the signal strength over all frequencies, with darker areas where the frequencies have very low intensity and yellow areas representing high intensity intervals. Averaging the values returned by the spectogram, the power spectrum of the signal is visualized with a logarithmic scale plot as function of the frequency.

The data acquisition system introduces noise in the signals that affect the power spectrum of the

signals. A segment of a signal from the vorticity probes without plasma is analyzed, revealing the noise interference in the original signals:

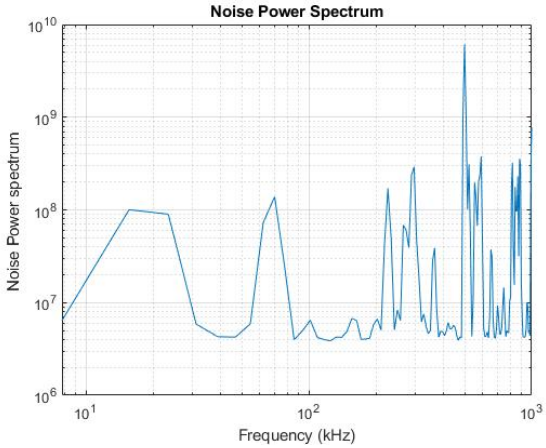

Figure 3.19: Average signal power spectra from an interval without plasma.

In the high frequencies, the noise is dominant over the signal power spectrums. The signals from the Langmuir probes are filtered with a low pass with a cutoff frequency of 400 kHz. The noise in lower frequencies could not be removed with such a method. For the low frequencies, the noise signal has a power spectrum much lower than the signal itself and the analysis can proceed without losing scientific valid results.

The signals allow to compute de probability distribution function (PDF) of the relevant quantities. The histogram is performed with the *histograma.m* script, that group the data into bins. The script analyses the maximum and minimum limits of the signal and defines the bin width as uniform using the Freedman–Diaconis rule as shown in 2.1.6. The normalization of the plot was done with the probability density function *PDF* estimate, where the area of each bar is the relative number of observations.

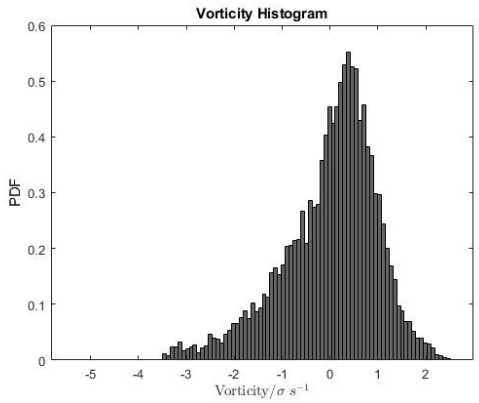

Figure 3.20: Histogram example.

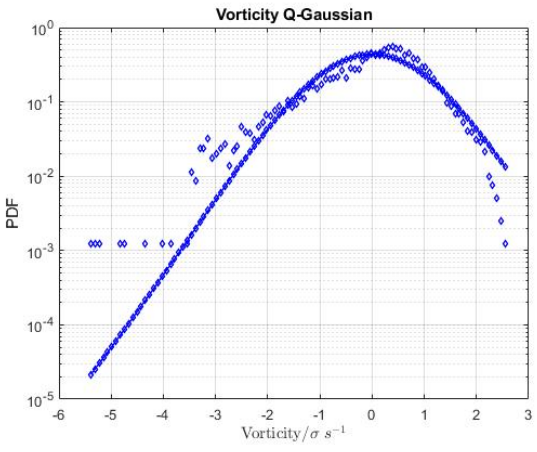

Figure 3.21: Q-Gaussian associated to the histogram plot example.

The data is fitted to a Q-Gaussian distribution through a MATLAB script *q_gaussian_fit.m*, that plot the result in a logarithmic scale on the *y* axes.

$$R_q(x) = a\left[1 + (q-1)\frac{x^2}{\lambda^2})\right]^{-\frac{1}{1-q}} \tag{3.7}$$

with x the corresponding to the bin value and R_q the associated height of the bin. The fit uses an auxiliary vector $x0$ that initialize the values for λ, called the scale parameter and a real number $q < 2$, which determine the behavior of the probability density function as presented in 2.1.5.

3.4.1 Poloidal phase velocity estimation

The method presented in section 2.1.6 is implemented using Matlab. The verification and validation of the algorithm is performed using two 50kHz sinusoidal waves as probes input as in Figure 3.22. The signals are separated by a time interval of 2μs. The expected velocity in this specific case should then be of 2500ms^{-1}, assuming that the probes are separated by a 5mm distance.

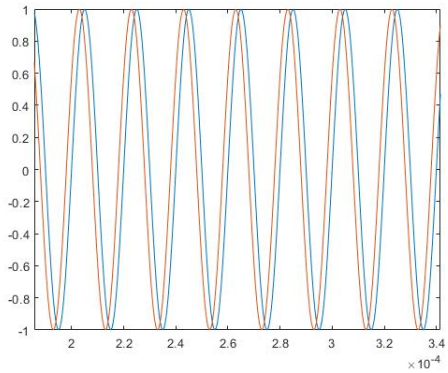

Figure 3.22: Input wave signals using to test the algorithm

Signals are changed to the frequency domain by the Fast Fourier Transform algorithm, and the power spectra computed. Only information regarding half of the frequencies of the signals will be available due to the Fast Fourier Transform properties. Since the power of the signal should be located at the low frequencies(comparing to the sampling frequency), no information is lost.

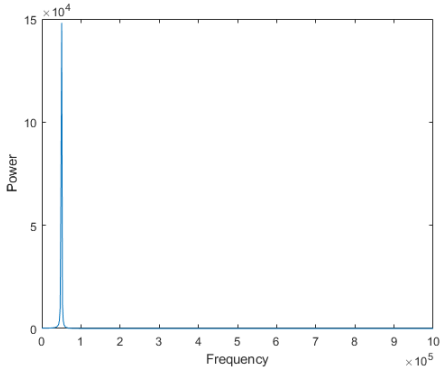

Figure 3.23: Example of the power spectra of one of the input signals, showing all signals power at the 50Khz frequency as expected.

The statistical description described in section 2.1.6 requires the allocation of the wavenumber val-

ues k's into bins like a histogram. Instead of counting the occurrences in that bin (summing 1's) like in a regular histogram, the average of the respective sample power values $S^j(w)$ associated with that wavenumber is summed. The allocation of the wavenumbers is performed with boolean masks that compare the $K^j(w)$ value to the bin edges, previously defined. When there is one bin edge value immediately before and one after simultaneously, the logic returns a true value allocating the corresponding average sample power from the two probes there. The function $I_{0,\Delta K}$ at equation 2.41 corresponds to this algorithm, giving 1 when the conditions are met and zero otherwise.

Performing this algorithm in the sinusoidal waves presented before gives the following $S(k, w)$ profile:

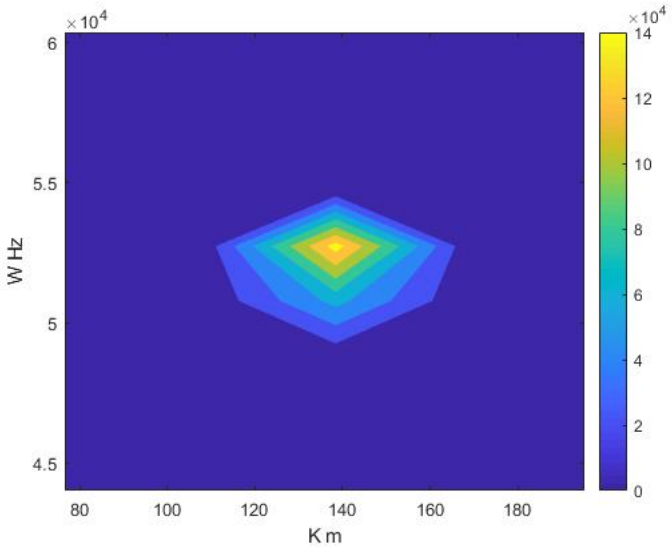

Figure 3.24: $S(k, w)$ profile using two sinusoidal two 50kHz sinusoidal signals

As expected, the output is characterized by high-density regions around the frequency of the input waves. The velocity estimated from the method, by equation 2.42 was about 2600 m/s, which agrees with the expected value from the conditions declared before.

The other presented method to validate the results obtained for the velocity estimation is based on correlation between signals. By default, the cross-correlation equation 2.43 gives the result without normalization. In order to produce an accurate normalized estimate, with the cross correlation at zero lag equal to one, the following equation should be implemented:

$$\hat{G_{xy}}(\tau) = \frac{1}{\sqrt{G_{xx}(0)G_{yy}(0)}} G_{xy}(\tau) \tag{3.8}$$

where G_{xx} and G_{yy} correspond to the auto correlations at zero lag.

Applying the algorithm on two sinusoidal signals presented at figure 3.22, the correlation results come as:

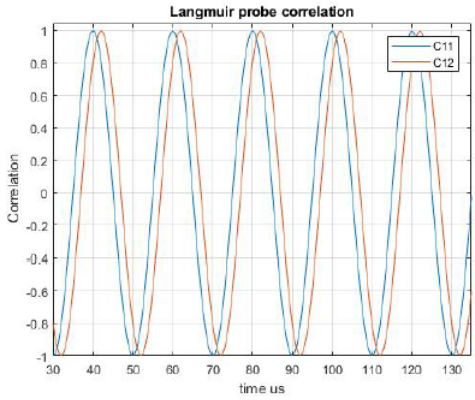

Figure 3.25: Auto correlation of signal from probe 1 in blue, and cross correlation between signals at orange

Plotting the lag between probes in function of the distance between probes and fitting the data points with a linear regression:

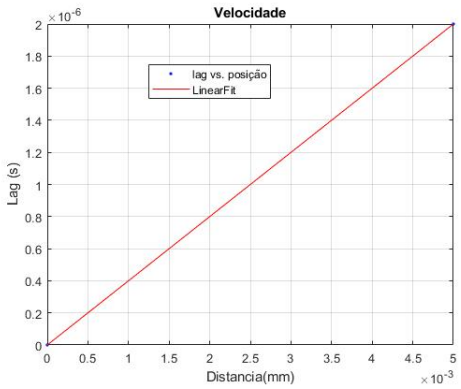

Figure 3.26: Linear regression for the data points

The linear regression slope corresponds to the propagation velocity of the signal. Obviously, in the presented case this step was not required since we are only talking about two signals. The velocity estimated from the correlation method was 2500 m/s, which was exactly what we should expect from the input signals. For a well-behaved set of input signals, both methods seem to give good results, with the cross-correlation being more precise, at least for non-fluctuating signals as the sinusoidal wave presented in this example.

Chapter 4

Results

4.1 Data analysis

The experiments were performed with 3 different tokamak configurations. The first one, which will be presented in detail through this section, consists of experiments with a magnetic field of 0,5 Tesla where PID controllers were used to control the plasma. The second configuration was similar, but the polarization device was removed. The third has a higher magnetic field, with a value of 0.6 Tesla. Signals from probe array 2 will be presented for this experiment in particular.

The designation probe 1 and probe 2 refer to the array of probes 1 to 6 and 7 to 12 respectively. The limiter position corresponds to the value of x=0 in all figures exhibited, with negative x values inside the limiter and positive in the SOL region.

4.1.1 Floating potential and ion saturation current profiles

Results obtained on ISTTOK indicate that floating potential measurements by Langmuir probes overestimate the amplitude of the plasma potential fluctuations due to the influence of the electron temperature fluctuations, but potential fluctuations measured by Langmuir Probes and Ball Pen Probes were found to be well correlated and roughly in phase.

The presented floating potential and ion current profiles are obtained averaging the regions of the cycles under study for each probe. The figures at left are the overlap of the polarized and non polarized signals, for the magnetic field configuration of 0,5T. The right figures correspond to the third experiment with a B=0.6T.

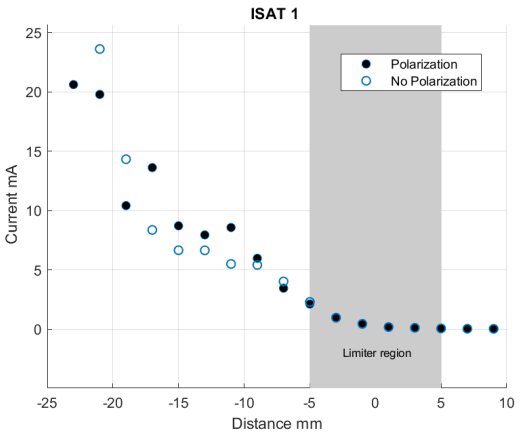

Figure 4.1: Ion saturation current profile from pin 1. Positive Cycle.

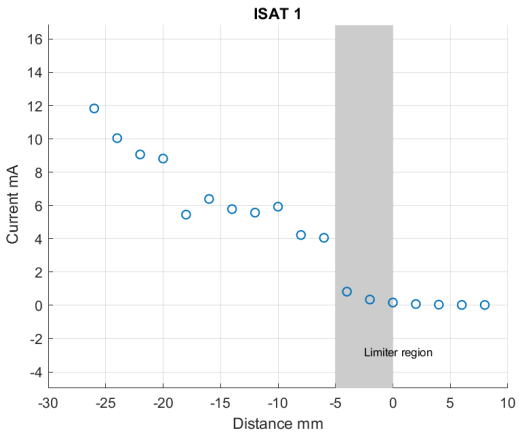

Figure 4.2: Ion saturation current profile from pin 1 for B=0.6T. No polarization applied.

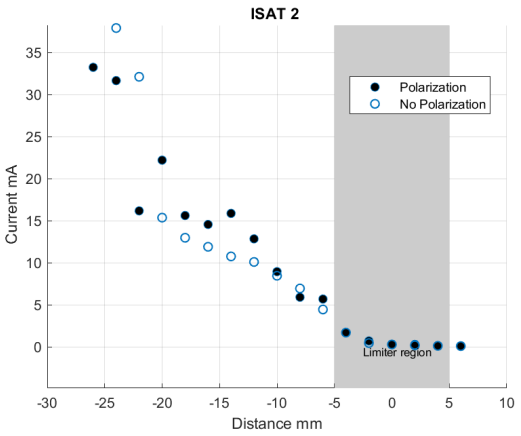

Figure 4.3: Ion saturation current profile from pin 7. Positive Cycle.

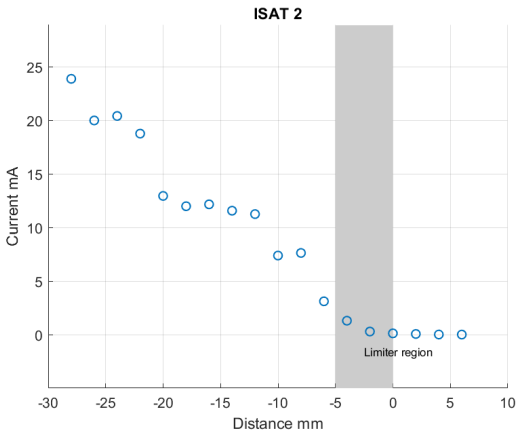

Figure 4.4: Ion saturation current profile from pin 7 for B=0.6T. No polarization applied.

Both ion saturation current values show an increase as we move towards the tokamak inner positions. The probe starts to collect current around the position 5 millimeters inside the limiter, with a stronger variation observed in both probes around the position 20 millimeters. Signals with polarization have saturation currents slightly smaller, compared with signals without polarization. The current for probe 1 is systematically smaller than the current for probe 2. This fact may be connected to the probe design. This result may suggest shadowing cast by probe 2 on probe 1. The ion saturation current suffers some changes due to the high magnetic field applied, with lower ion saturation current along the radial positions under analysis.

The floating potential profiles for the remaining probes are also computed. These results were computed for all the cycles under study, and the presented figures correspond to the mean of these results:

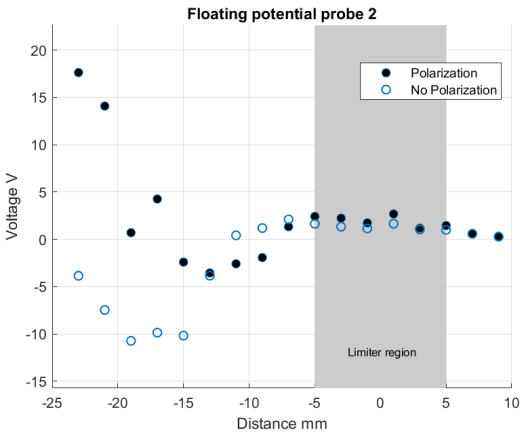

Figure 4.5: Floating potential radial profile from pin 2. Positive Cycle.

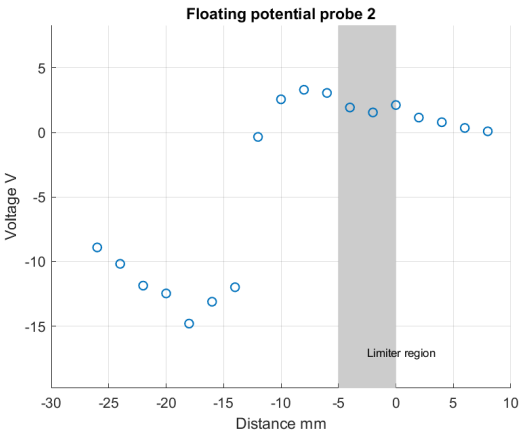

Figure 4.6: Floating potential radial profile from pin 2 for B=0.6T. No polarization applied.

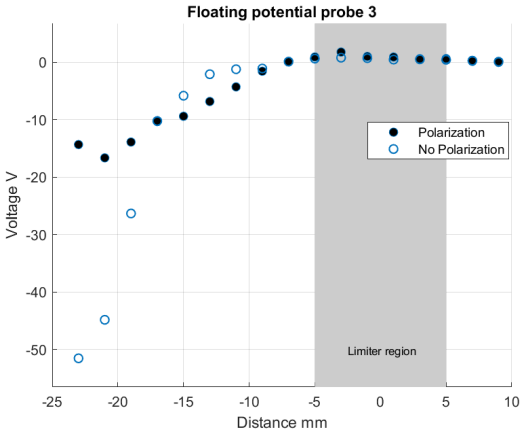

Figure 4.7: Floating potential radial profile from pin 3. Positive Cycle.

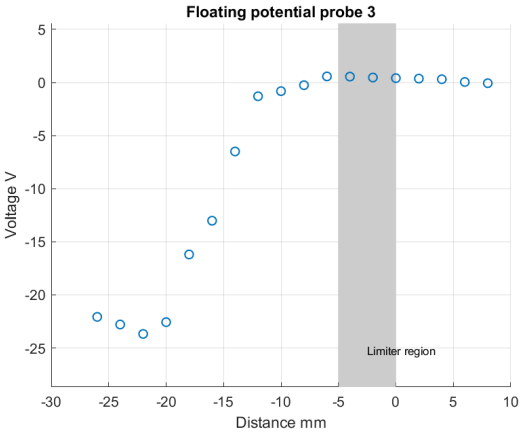

Figure 4.8: Floating potential radial profile from pin 3 for B=0.6T. No polarization applied.

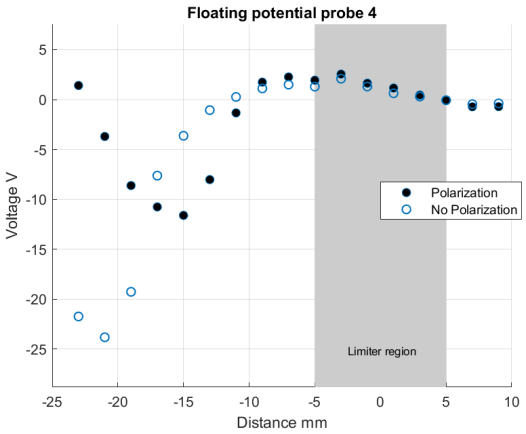

Figure 4.9: Floating potential radial profile from pin 4. Positive Cycle.

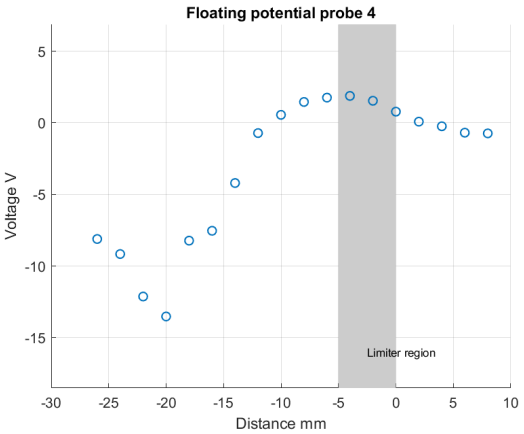

Figure 4.10: Floating potential radial profile from pin 4 for B=0.6T. No polarization applied.

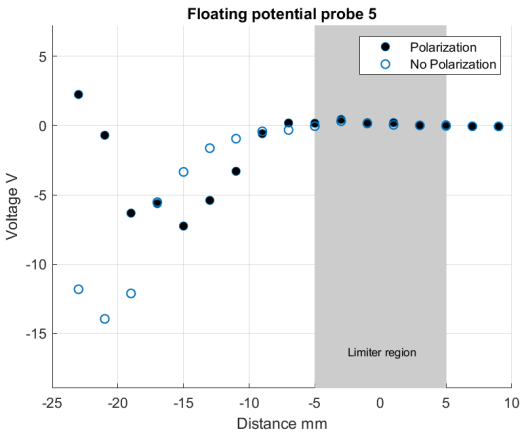

Figure 4.11: Floating potential radial profile from pin 5. Positive Cycle.

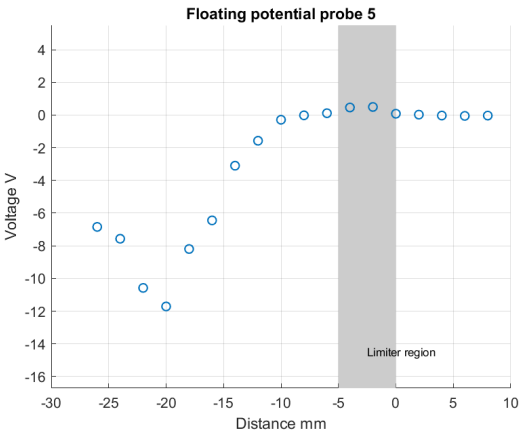

Figure 4.12: Floating potential radial profile from pin 5 for B=0.6T. No polarization applied.

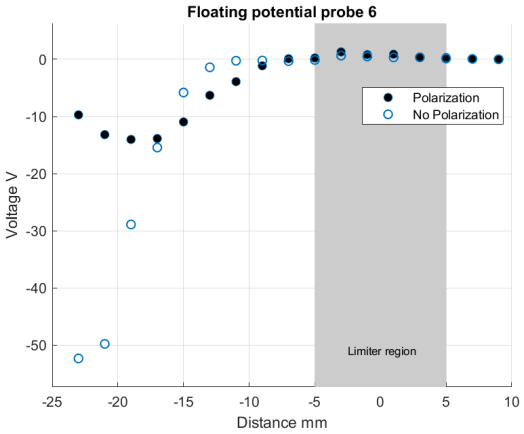

Figure 4.13: Floating potential radial profile from pin 6. Positive Cycle.

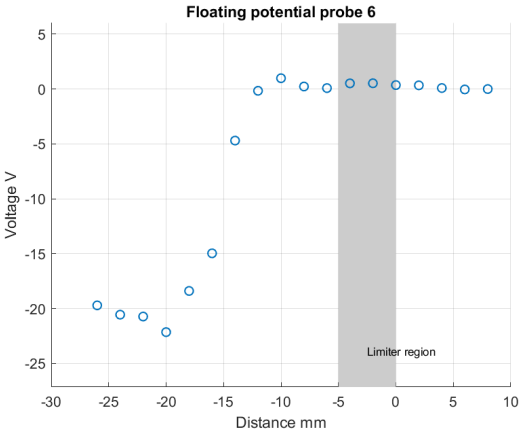

Figure 4.14: Floating potential radial profile from pin 6 for B=0.6T. No polarization applied.

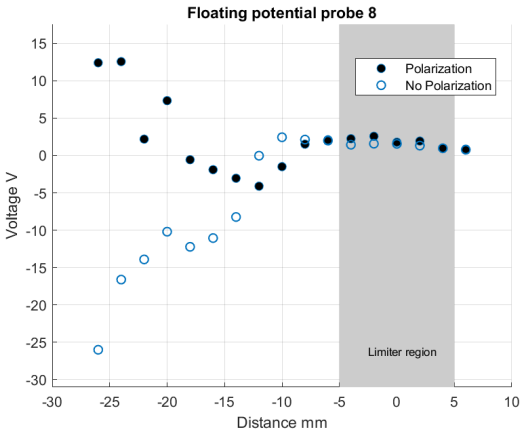

Figure 4.15: Floating potential radial profile from pin 8. Positive Cycle.

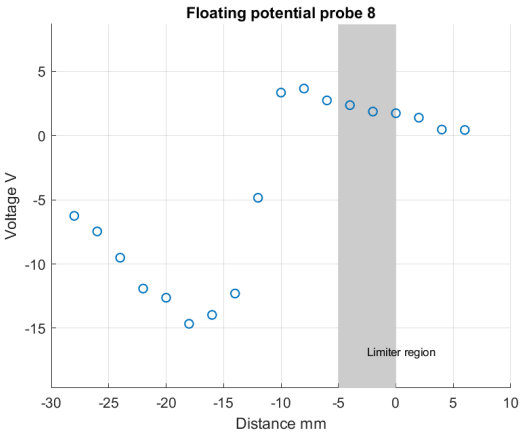

Figure 4.16: Floating potential radial profile from pin 8 for B=0.6T. No polarization applied.

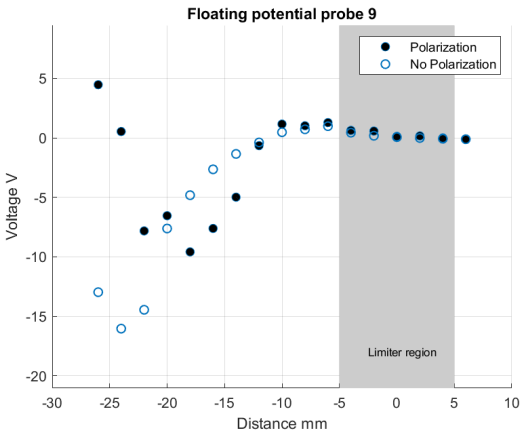

Figure 4.17: Floating potential radial profile from pin 9. Positive Cycle.

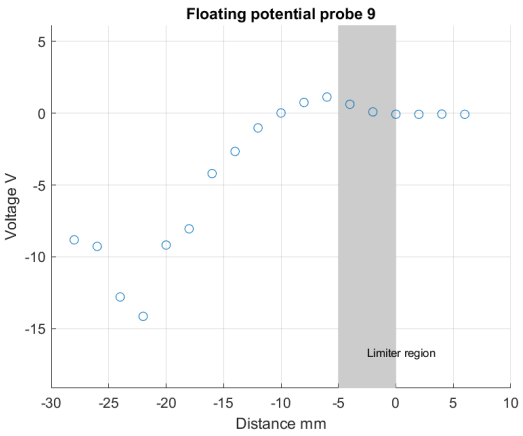

Figure 4.18: Floating potential radial profile from pin 9 for B=0.6T. No polarization applied.

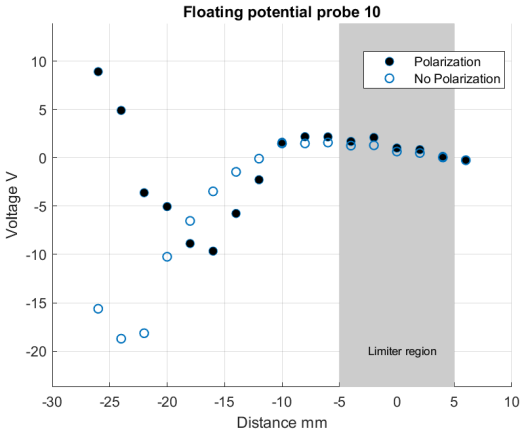

Figure 4.19: Floating potential radial profile from pin 10. Positive Cycle.

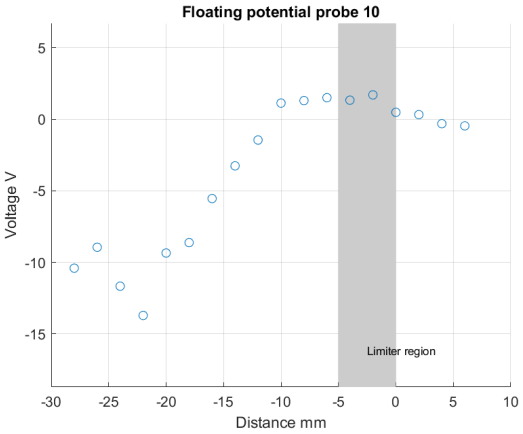

Figure 4.20: Floating potential radial profile from pin 10 for B=0.6T. No polarization applied.

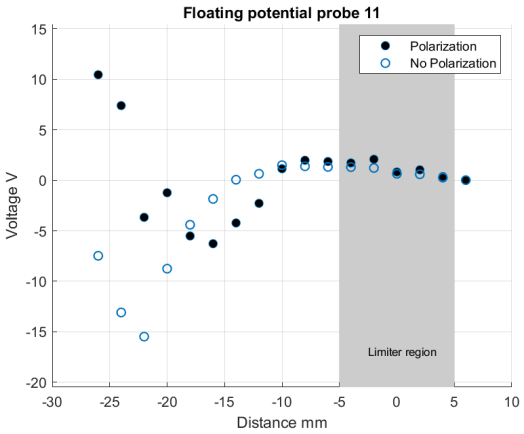

Figure 4.21: Floating potential radial profile from pin 11. Positive Cycle.

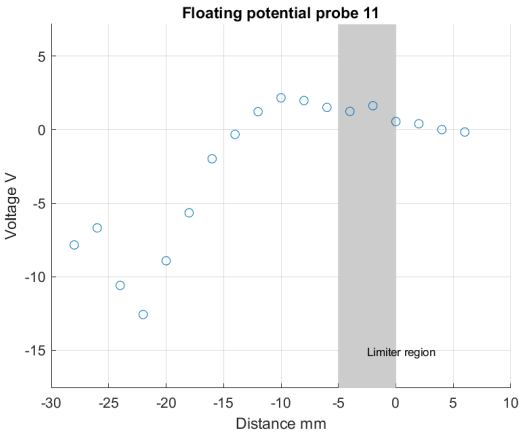

Figure 4.22: Floating potential radial profile from pin 11 for B=0.6T. No polarization applied.

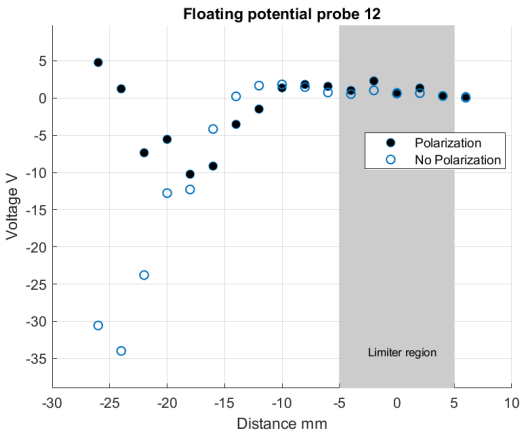

Figure 4.23: Floating potential radial profile from pin 12. Positive Cycle.

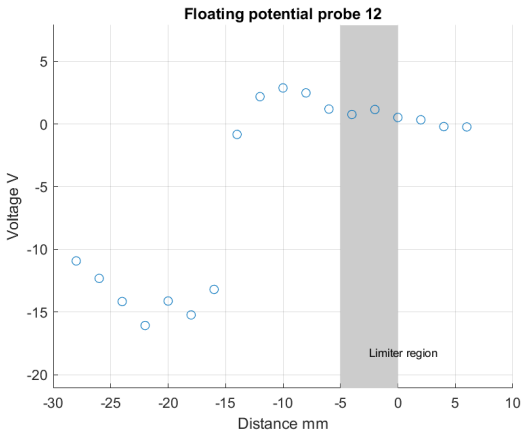

Figure 4.24: Floating potential radial profile from pin 12 for B=0.6T. No polarization applied.

From previous experiments and knowledge of plasma behavior in tokamaks, a constant increase in the floating potentials, and ion current, moving to the inland regions of the tokamak, is expected. Some floating potential profiles show strange behavior, especially in the innermost regions of the tokamak. A clear example of it is the floating potential radial profile from probe 2, which drops until 15 millimeters but suddenly starts to increase when moving into the plasma. The profiles for the polarization results show floating potential profiles close to zero before 10 millimeters, dropping continuously until 15 millimeters, increasing in the inner regions of the tokamak. Commonly, all probes show this kind of profile, except for probe 3, with a profile that resembles a result without polarization. The results for the higher magnetic field experiment show values close to the ones obtained for the polarization in the first experiment.

The reason for this possibly unexpected behavior in the non-polarized signals is not evident. The plasma control methods are the same from previous experiments. The presence of the electrode that polarizes the plasma is the only factor that was changed, and that may induce some perturbations in the plasma. The second series of experiments, this time without the electrode inside the tokamak were performed. Some of the radial profiles obtained from this new sweep are presented from Figure 4.25 to 4.36 :

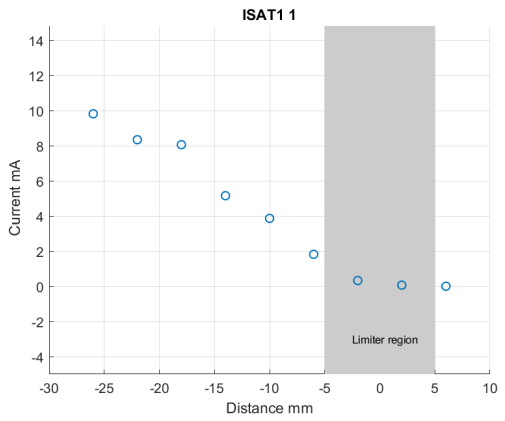

Figure 4.25: Ion saturation current profile from pin 1. Positive Cycle.

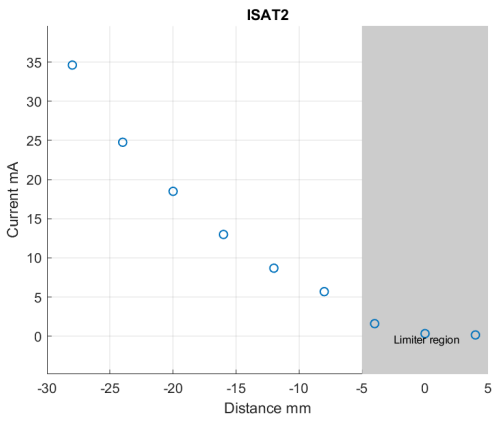

Figure 4.26: Ion saturation current profile from pin 7. Positive Cycle.

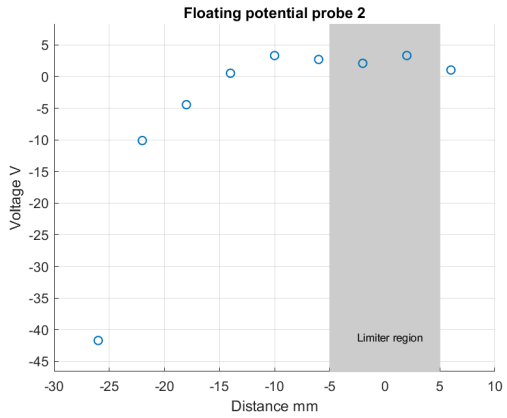

Figure 4.27: Floating potential radial profile from pin 2. Positive Cycle.

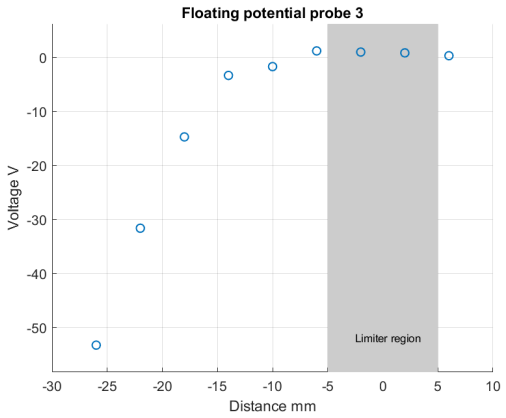

Figure 4.28: Floating potential radial profile from pin 3. Positive Cycle.

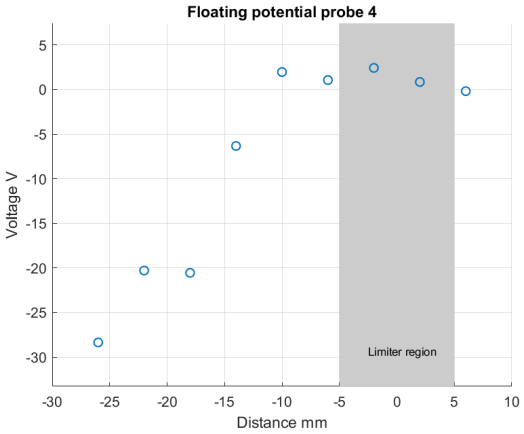

Figure 4.29: Floating potential radial profile from pin 4. Positive Cycle.

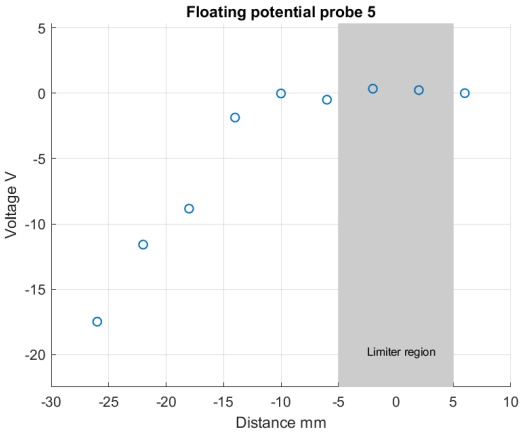

Figure 4.30: Floating potential radial profile from pin 5. Positive Cycle.

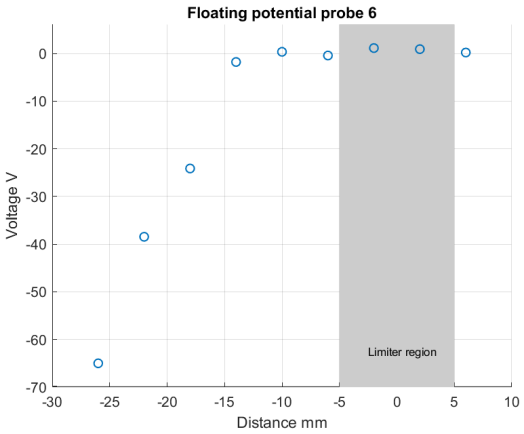

Figure 4.31: Floating potential radial profile from pin 6. Positive Cycle.

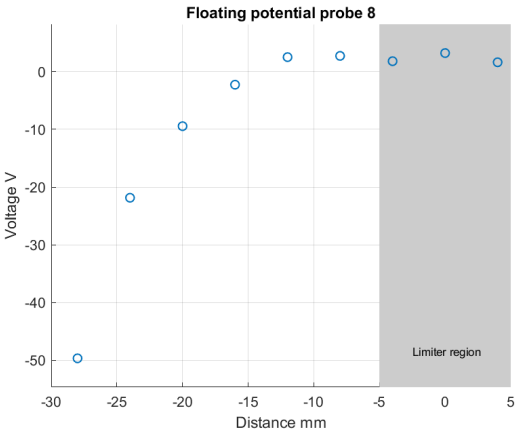

Figure 4.32: Floating potential radial profile from pin 8. Positive Cycle.

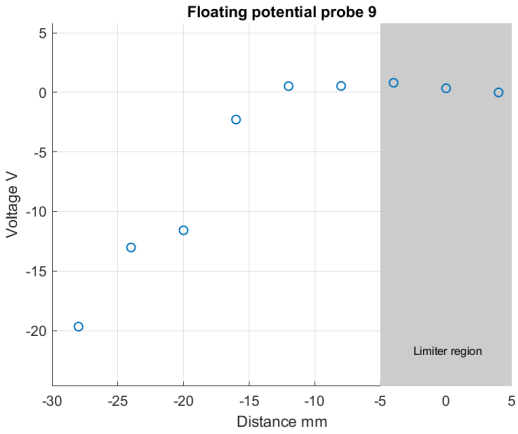

Figure 4.33: Floating potential radial profile from pin 9. Positive Cycle.

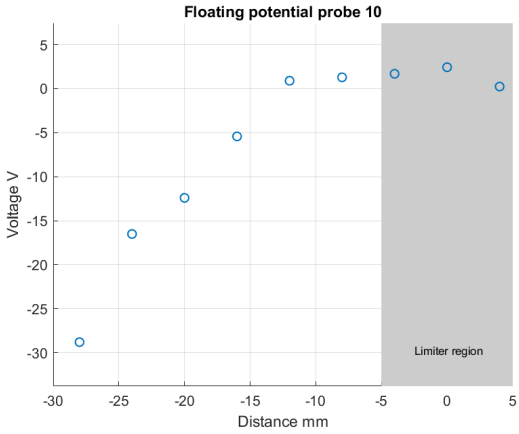

Figure 4.34: Floating potential radial profile from pin 10. Positive Cycle.

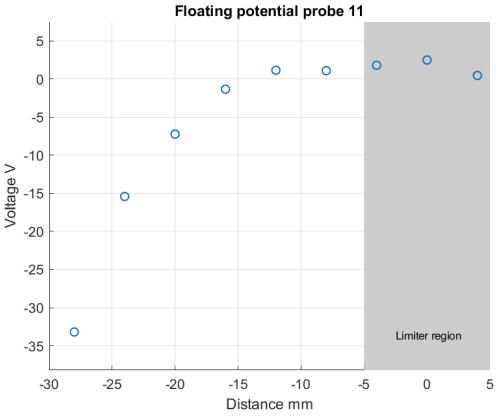

Figure 4.35: Floating potential radial profile from pin 11. Positive Cycle.

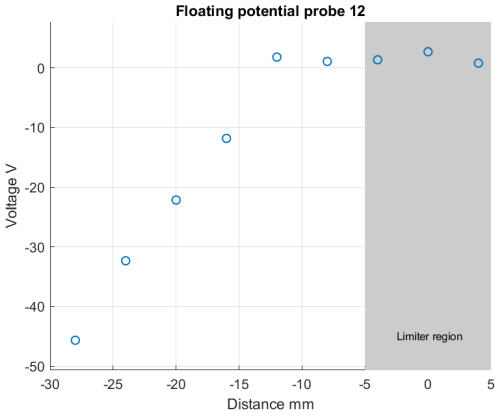

Figure 4.36: Floating potential radial profile from pin 12. Positive Cycle.

The unexpected mean values of floating potential and ion saturation current from the first experiment, with the polarization electrode, do not necessarily mean that the fluctuations used to compute the relevant quantities studied in this thesis are incorrect. The signals from the second experiment without the electrode are processed and the same quantities are determined. If the results are equivalent, the first experiment can be validated, and the results from the polarization can be assumed as accurate, despite the mean values used to compute the floating potential radial profiles not agreeing. The results for the second experiment show floating potentials constantly decreasing as the probe move into the inner regions of the tokamak. No signs of a sudden increase after the 15 millimeters mark. Going forward, all the analysis will be compared to the results associated with the second experiment, in an attempt to validate the results.

4.1.2 Electric Fields

The radial and poloidal electric fields are computed recurring to the equations presented in Section 3.3. The results are are presented from Figure 4.37 to 4.40:

Radial Electric Field

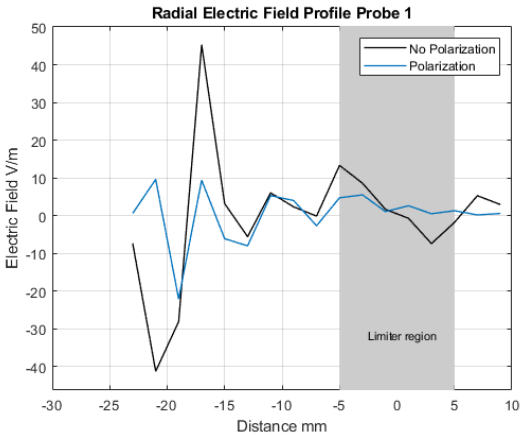

Figure 4.37: Radial electric field profile for probe 1. Positive Cycle.

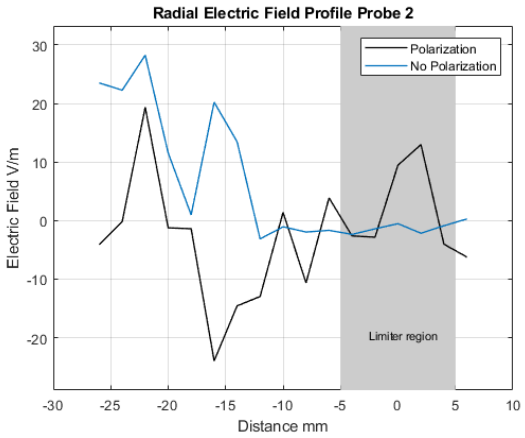

Figure 4.38: Radial electric field profile for probe 2. Positive Cycle.

Poloidal Electric Field

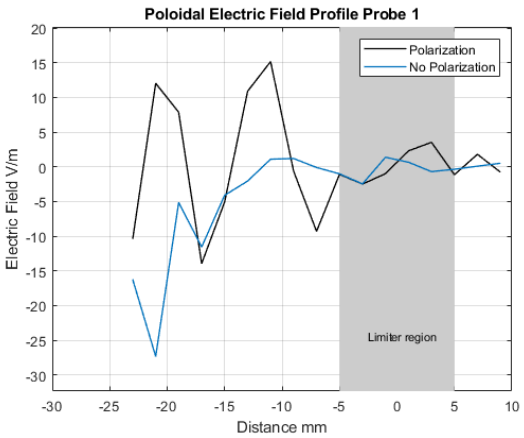

Figure 4.39: Poloidal electric field profile for probe 1. Positive Cycle.

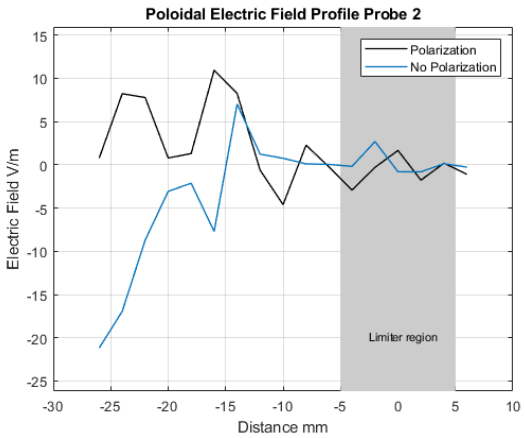

Figure 4.40: Poloidal electric field profile for probe 2. Positive Cycle.

The electric field for both probes is close to zero in the SOL region for the nonpolarized signals analyzed. Polarization increases the oscillation of the electric field in this region.

There is evidence of a shear layer around the region 10/15 millimeters with the strong electric field variations. These variations are amplified by the polarization.

4.1.3 Poloidal Velocity estimation with S(k,w)

Estimating the velocity of the plasma from Langmuir probes should not be a problem. Although, this probe in particular may face some problems. A langmuir probe with several pairs of pins in different radial positions would be more suitable, since it would allow to compute the velocity profile using only 1 discharge.

The poloidal velocity is computed across all the radial positions for both probes. Since the results are redundant, only the velocity for probe 1 will be presented. The estimation is obtained using the method described in Chapter 2.1.6. The wavenumber and frequency mapping, associated with the S(k,w) values are presented for some radial positions. Polarized and no polarized mapping are presented side by side for easier comparison.

Starting with signals from the SOL region, the results are presented from Figure 4.41 to 4.44:

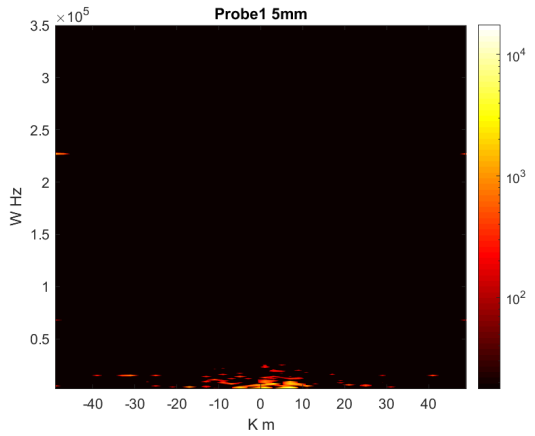

Figure 4.41: S(K,W) profile for probe 1, position 5 millimeters.Estimated velocity of 501.3m/s.

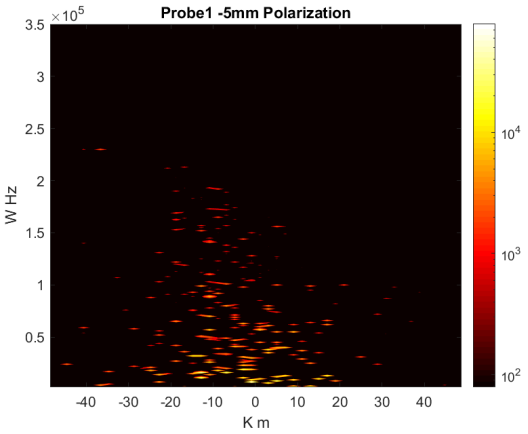

Figure 4.42: S(K,W) profile for probe 1 with polarization, position 5 millimeters.Estimated velocity of -720.4.2m/s.

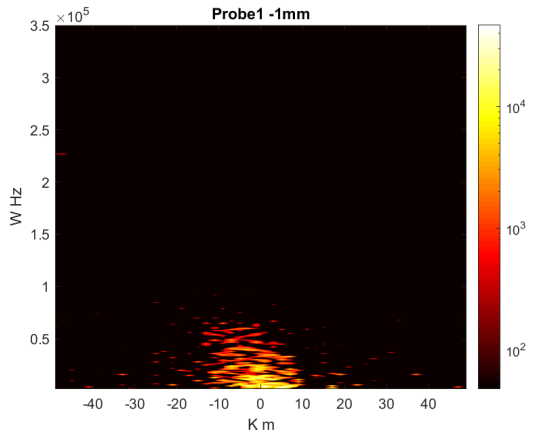

Figure 4.43: S(K,W) profile for probe 1, position 1 millimeters.Estimated velocity of -980.3m/s.

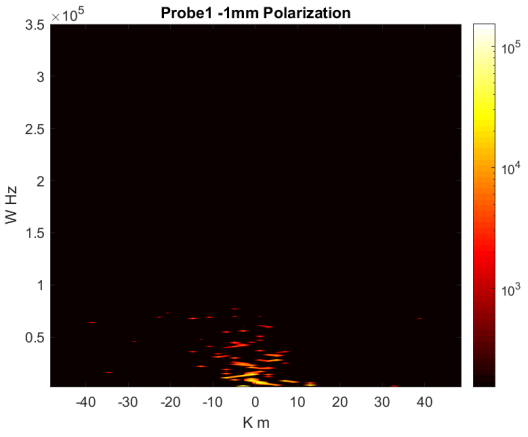

Figure 4.44: S(K,W) profile for probe 1 with polarization, position 1 millimeters.Estimated velocity of -1985.3m/s.

The poloidal velocity calculation, based on this matrix, is computed using equation 2.42. The map-

ping in the SOL region shows a low dispersion on S(k,w) values for the non polarized plasma, with most of the data located at the low frequencies. After polarizing the plasma, the distribution becomes more disperse through frequencies up to 200kHz. There is evidence of polarization increasing the velocity in this region. The poloidal velocity estimated in the radial position 5 millimeters outside of the limiter, in the SOL region, is 501.3m/s and -720.4m/s for the nonpolarized and polarized plasma respectively. For position 1 mm inside the limiter, values of -980.3m/s and -1985.3m/ are estimated.

Analyzing now signals from the middle range of the radial scan from Figure 4.45 4.48:

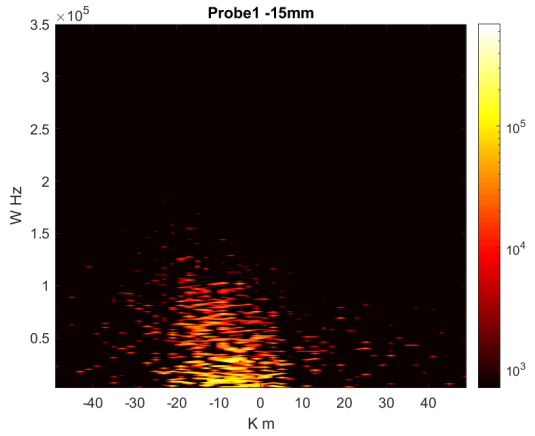

Figure 4.45: S(K,W) profile for probe 1, position -15 millimeters without polarization.Estimated velocity of -3278.6m/s.

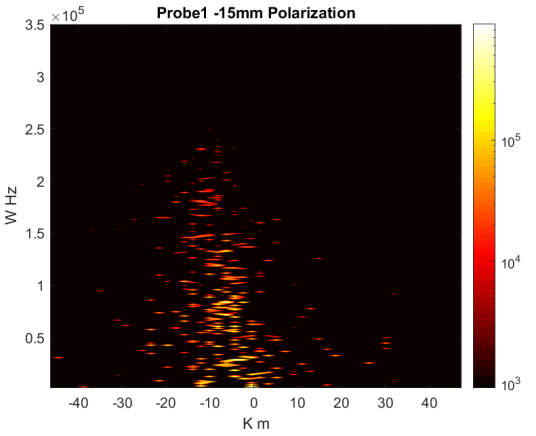

Figure 4.46: S(K,W) profile for probe 1 with polarization, position -15 millimeters.Estimated velocity of -11785.3m/s.

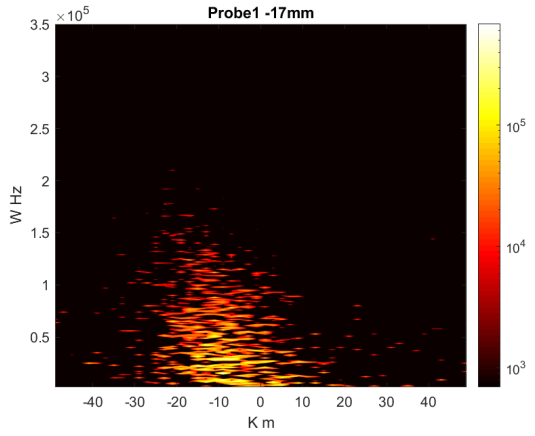

Figure 4.47: S(K,W) profile for probe 1, position -17 millimeters without polarization.Estimated velocity of 3698.4m/s.

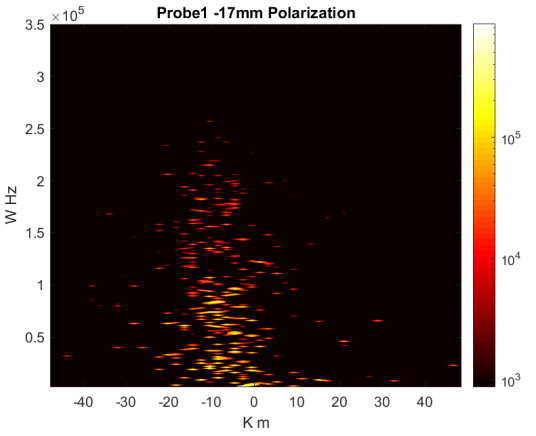

Figure 4.48: S(K,W) profile for probe 1 with polarization, position -17 millimeters.Estimated velocity of -11015.9m/s.

The S(k,w) mapping has values predominantly on the left side with a clear slope. This slope, which basically gives the velocity, is much more defined comparing to the previously presented positions, with a less disperse S(k,w) distribution. The low to medium range of frequencies concentrate most of the data.

For the first presented position, the poloidal velocity is -3278.6m/s and -11785.3m/s for the nonpolarized and polarized signals respectively. For the position 17 millimeter inside the limiter, the results

yield -3698.4m/s and -11015.9m/s. Similarly to the last example, there is a trend with velocity increasing while going into the plasma. Higher values of velocity for polarized signals are also observed for this radial positions.

For the inner positions analyses in the experiment, the results yield:

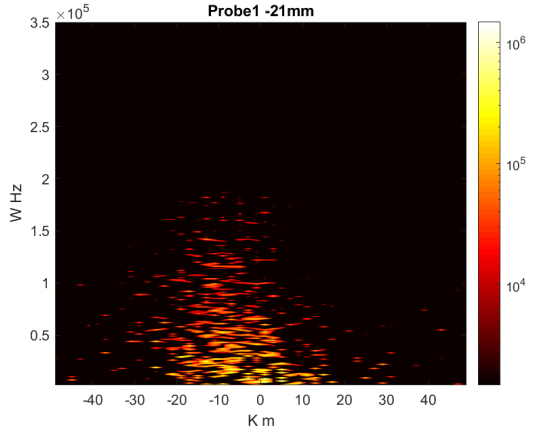

Figure 4.49: S(K,W) profile for probe 1, position -21 millimeters without polarization.Estimated velocity of -1894.3m/s.

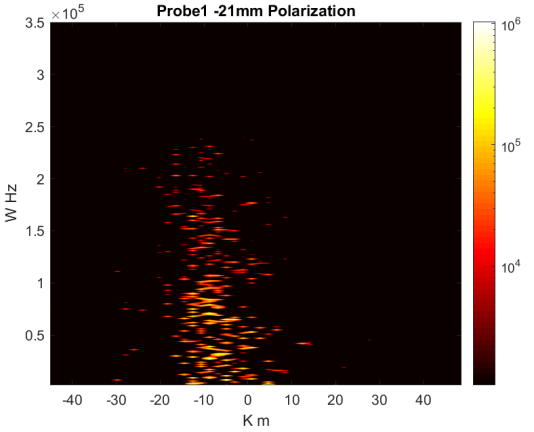

Figure 4.50: S(K,W) profile for probe 1 with polarization, position -21 millimeters.Estimated velocity of -4872.3m/s.

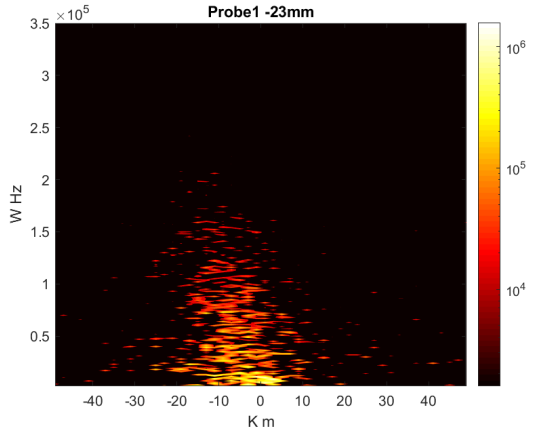

Figure 4.51: S(K,W) profile for probe 1, position -23 millimeters without polarization.Estimated velocity of -3786.9m/s.

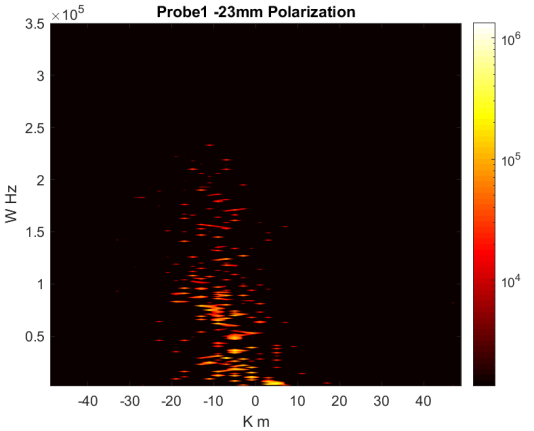

Figure 4.52: S(K,W) profile for probe 1 with polarization, position -23 millimeters.Estimated velocity of -8256.1m/s.

At this region, the velocities tend to be lower than the last ones presented. Although, the polarization still leads to a massive increase in the poloidal velocity, comparing to the results without polarization. With all the velocities computed, the full poloidal velocity radial profile is presented in Figure 4.53 and 4.54::

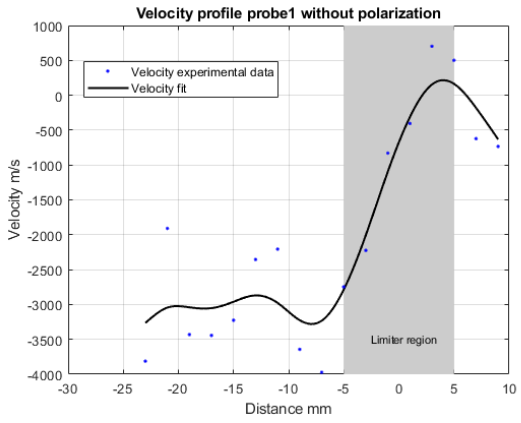

Figure 4.53: Plasma Poloidal velocity for probe 1. Positive Cycle

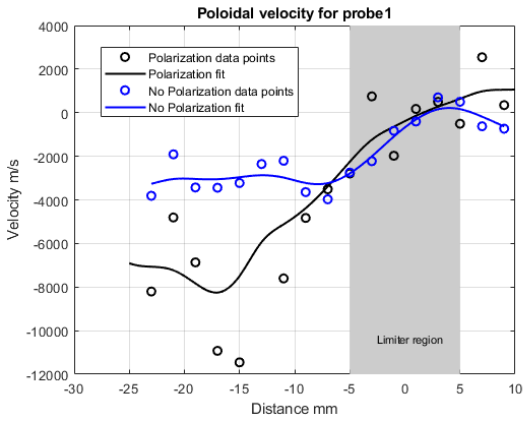

Figure 4.54: Plasma Poloidal velocity for probe 1. Polarization vs no Polarization. Positive Cycle

The radial profile confirms the increase in poloidal velocity as we start to move into the innermost regions of the tokamak. Both polarized and nonpolarized signals show this profile, with polarization being characterized by much higher speeds. The poloidal velocity varies slowly in the SOL region. Strong velocity gradients are observed after the limiter, which can be explained by a strong shear layer. This shear is stronger in the polarization experiment, which is why the poloidal velocitis during polarization are usually much higher.

The analysis of probe 1 suggests that the poloidal velocity stabilizes after the 10/15mm mark inside the limiter, for both polarized and no polarized plasma, with osculating values of velocity.

The signals from the experiment with a higher magnetic field configuration are also presented in Figure 4.55.

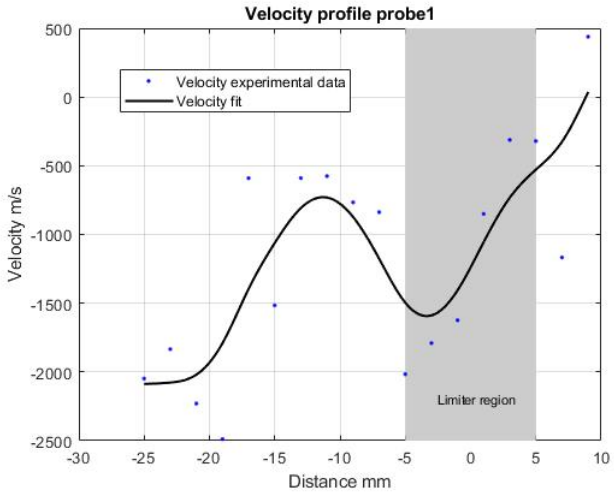

Figure 4.55: Plasma Poloidal velocity for probe 1. B=0.6T

The same profile is observed, with the poloidal velocity increasing after the limiter region. The velocity decreases between the 10 and 15 millimeter region, with values around 500m/s. After this, the velocity increases again, with values up to 2000m/s.

All quantities analyzed through this work, with the exception of poloidal velocity, show big variations

between the radial positions 10/15 millimeters inside the limiter, which would suggest that the shear layer is around that radial position. From the results of the poloidal velocity, using the S(k,w) method, that shear layer seem to be located right after the limiter, with velocity increasing fast.

The same analysis will be done using the correlation method, which may help corroborate these findings.

4.1.4 Poloidal Velocity estimation with correlation method

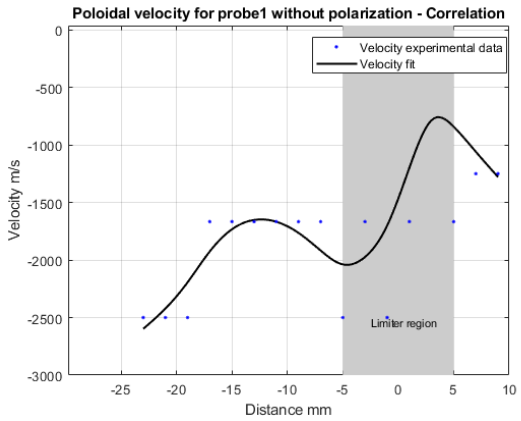

Figure 4.56: Plasma Poloidal velocity for probe 1. Correlation method

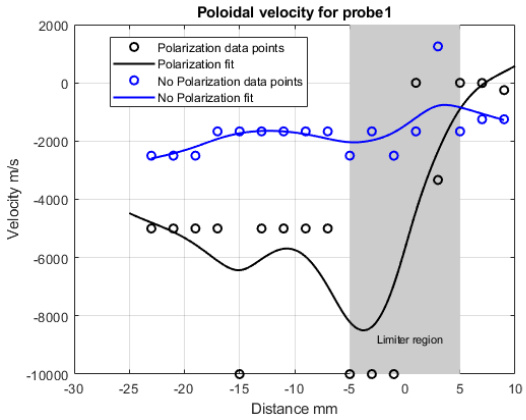

Figure 4.57: Plasma Poloidal velocity for probe 1, Polarization vs no Polarization. Correlation method

The correlation method, which results are presented in Figure 4.56 and 4.57, confirm the increasing plasma poloidal velocity moving into the inner regions of the tokamak. In this analysis, the velocity do not vary much moving from the SOL to the limiter, as we have seen in the previous method.

The sobreposition between the results obtained for the experiment 1 using both methods is presented in Figures 4.58 and 4.59:

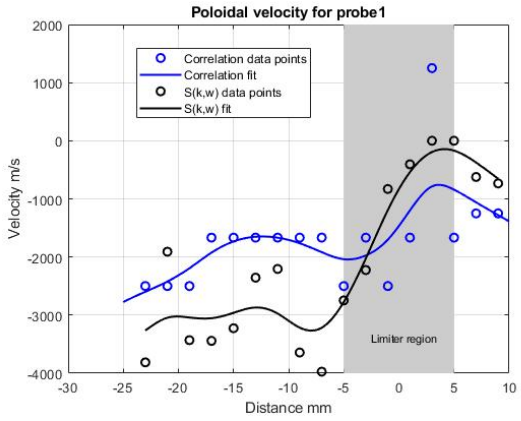

Figure 4.58: Plasma Poloidal velocity for probe 1 with B=0.5T.

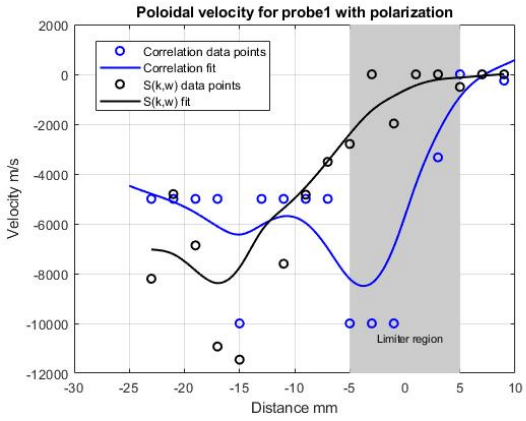

Figure 4.59: Plasma Poloidal velocity for probe 1 with B=0.5T .

As observed from previous results, both methods estimate similar radial profiles for the poloidal velocity. The magnitude of the velocity also agree with the one observed in the previous method.

The poloidal velocity results seem to agree in both methods. The results for the higher magnetic field configuration are also explored in Figure 4.60 and Figure 4.61 :

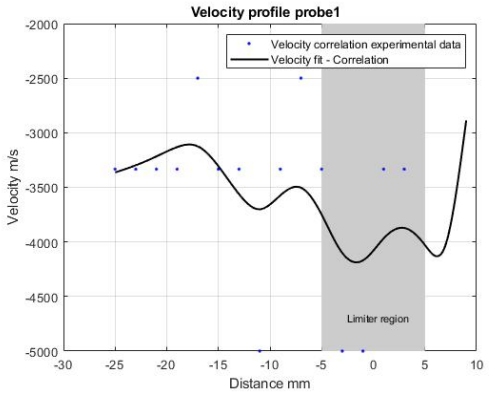

Figure 4.60: Plasma Poloidal velocity for probe 1 with B=0.6T. Correlation method

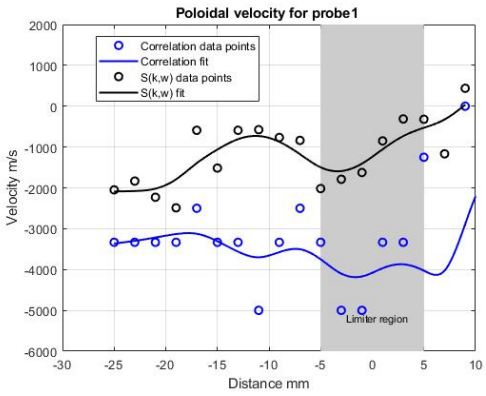

Figure 4.61: Plasma Poloidal velocity for probe 1 with B=0.6T . Sobreposition of both methods

4.1.5 Correlation Length

Measurements at RFX show a maximum of the turbulent transport close to the shear layer and a reduction at the plasma edge[57]. Structure absorption amplifies the shear flow. Assuming the same principle, operating near the edge of confined toroidal plasmas should lead to amplification of the shear flows at the reactor's boundary. Studies have also shown that an increase in the shear can suppress density fluctuations, leading to a decrease in the correlation length and stabilization in the plasma[58].

The correlation length is computed from the coherency via a statistical description. Floating potential signals gathered from pin two and five of the probe are grouped in several intervals with 50 points each, with an overlap of 25 points per interval analyzed, in order to get better statistical results. Measuring the coherence between floating potential signals from probe 2 and 5(located at the same poloidal position), at different radial positions, the correlation length can be inferred. For each interval of points, the maximum value of coherence is calculated. With this maximum and assuming a exponential decaying behavior, the correlation length of the fluctuations is determined.

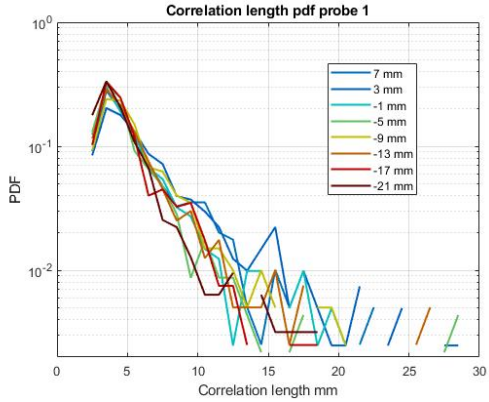

Figure 4.62: Correlation length for probe 1. B=0.5T.

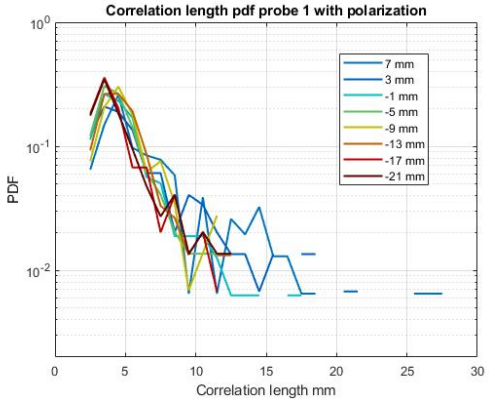

Figure 4.63: Correlation length for probe 1 with polarization. B=0.5T.

The correlation length can be seen as the typical length scale on which the deviations from the mean values stop being similar. Figures 4.62 and 4.63 present the results obtained for the correlation length of experiment 1, with and without polarization correspondingly. The PDF shows clear variations of the correlation length as function of the probe position. Polarization effects on the correlation length are also observed, with a strong reduction in the large correlated events, compared to the non polarization results. This result was expected due to a more pronounced decorrelation of events originated by the self generated shear layer. This effect is also expected as the polarization increase the shear velocity as observed in Figure 4.58 and 4.59.

The mean of the correlation length PDF results is computed for the experiment 1 and 3, and plotted in function of the radial position. The results are presented in Figure 4.64.

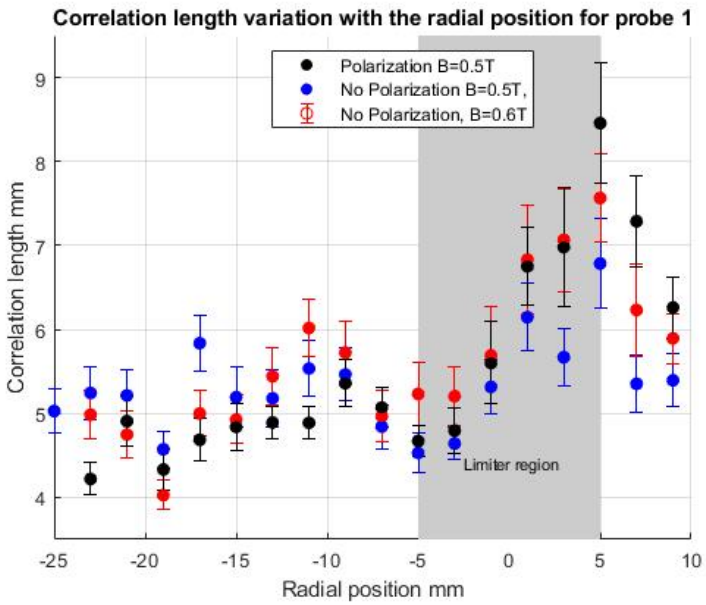

Figure 4.64: Correlation length mean PDF values as function of the radial position for probe 1. Comparison between B=0.5T with and without polarization and B=0.6T.

Strong variations of the correlation length are observed around the limiter position. The clear variation of this correlation length with the radial position strongly confirms that the correlation lengths is affected by the presence of a self generated shear layer on the Tokamak as previously observed at JET[59]. It would be interesting to perform these measurements with ion saturation probes. However the present probe configuration do not allow that since the ion saturation current pins of the probe have a poloidal separation.

4.1.6 Reynolds Stress

The Reynolds Stress, also known as a turbulent flux of momentum, introduced in section 2.1.3 is explored using the signals from the Langmuir probe array. This mechanism is intrinsically related to the generation of shear flows by turbulence, so the values around the SOL are expected to be close to zero. The results for both polarization and no polarization are presented. The results for the experiment

without the electrode are also presented from Figure 4.65 to 4.68:

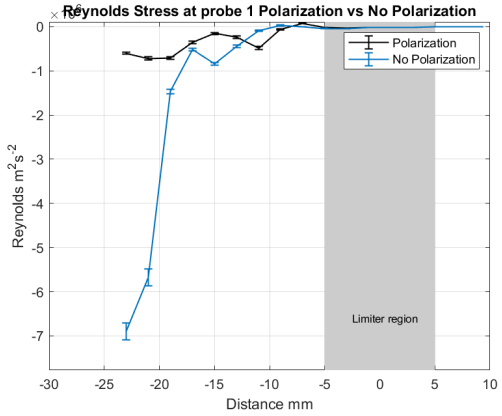

Figure 4.65: Reynolds Stress radial profile for probe 1.

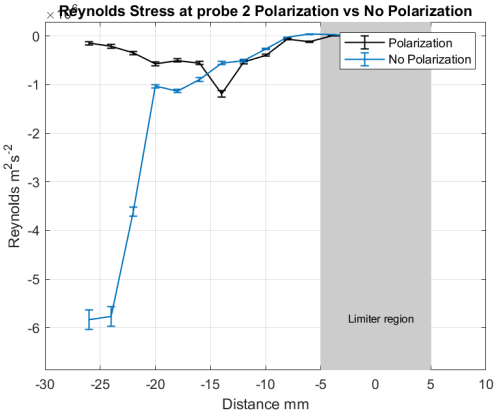

Figure 4.66: Reynolds Stress radial profile for probe 2.

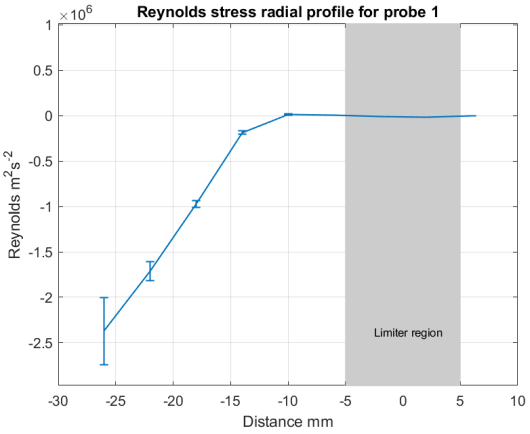

Figure 4.67: Reynolds Stress radial profile for probe 1. Second experiment without the electrode

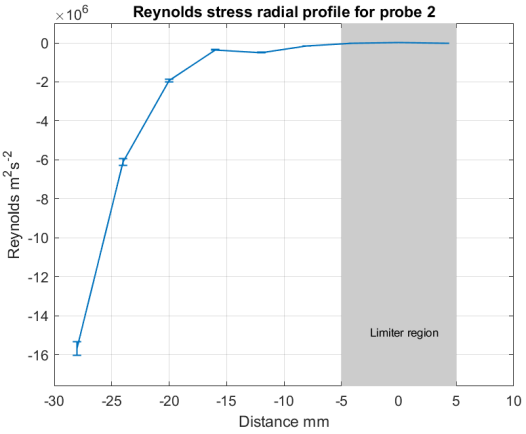

Figure 4.68: Reynolds Stress radial profile for probe 2. Second experiment without the electrode

The Reynolds stress results stay around zero until the position 10/15 millimeters inside the limiter. After, the nonpolarized results for the Reynolds Stress increase rapidly. Unfortunately, due to the lack of points in inner regions, due to limitations when working with Langmuir probes, there is no way to tell if the Reynolds keeps decreasing or not after the 26-millimeter mark. These results show a clear effect of the polarization on turbulence mechanisms, suppressing the Reynolds stress, keeping this flux of momentum almost constant at all radial positions. The Reynolds stress profiles can be compared with results with a higher magnetic field configuration and with previous results found in ISTTOK, presented in Figures 4.69 and 4.70 respectively:

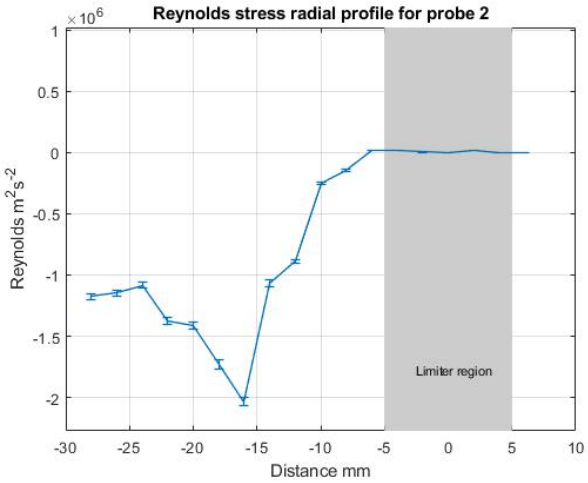

Figure 4.69: Reynolds Stress for probe 2. B=0.6T.

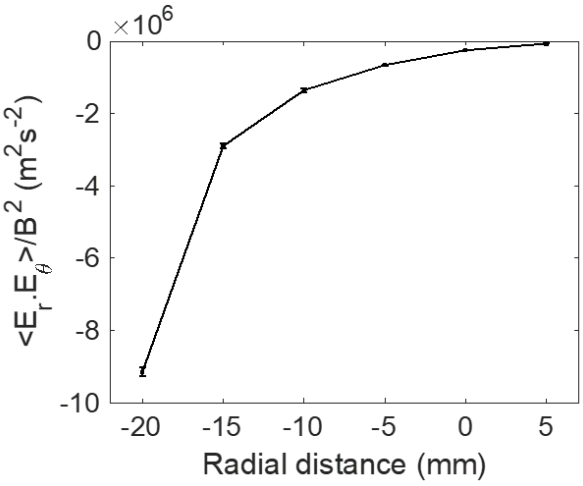

Figure 4.70: Reynolds Stress from previous experiments at ISTTOK [60].

Again, the higher magnetic field seem to increase the shear, decorrelating the turbulent events. The effect is not so visible as in the case of applying polarization, but there is a clear decrease in the Reynolds stress, comparing to Figure 4.68. The results also agree with previous experiments, exhibiting a strong gradient inside the limiter with orders of magnitude within the expected values.

Following the statistical analysis, the Reynolds Stress power spectrum is calculated and the results are presented in Figure 4.71 and 4.72:

Reynolds Power Spectrum

The results obtained for the Reynolds Power Spectrum during the experiments are presented from Figure 4.71 to 4.77.

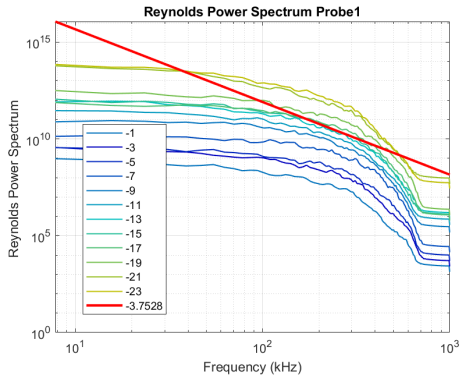

Figure 4.71: Reynolds power spectrum for probe 1. Positive Cycle

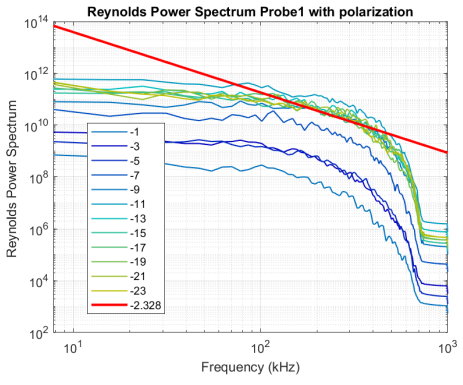

Figure 4.72: Reynolds power spectrum for probe 1 with polarization. Positive Cycle

The Reynolds stress show consistently through all experiments a strong regions in the inner region of the limiter.

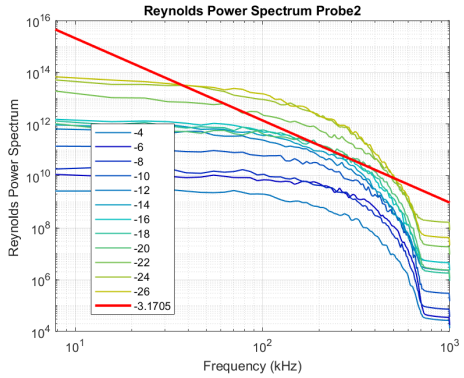

Figure 4.73: Reynolds power spectrum for probe 2. Positive Cycle

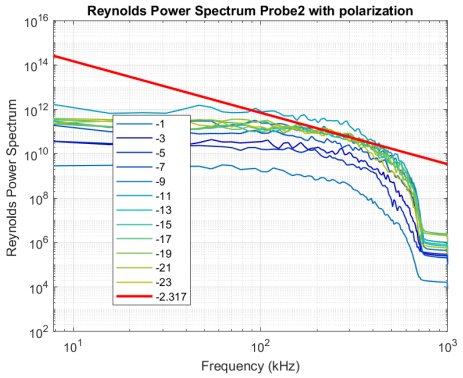

Figure 4.74: Reynolds power spectrum for probe 2 with polarization. Positive Cycle

The Reynolds Stress for the non polarized plasma show a spectral index of about 3.8. The polarization seem to slow down the exponential decay on the power spectra with spectral indexes values 20% and 27% lower than the ones without polarization.

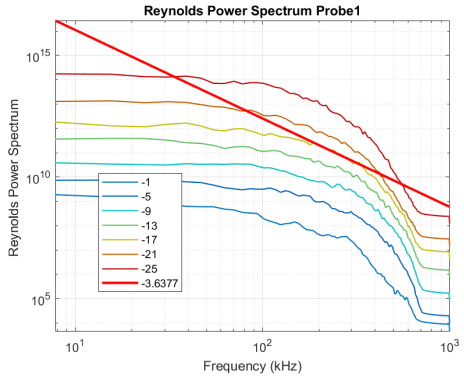

Figure 4.75: Reynolds power spectrum for probe 1. Second experiment without the electrode

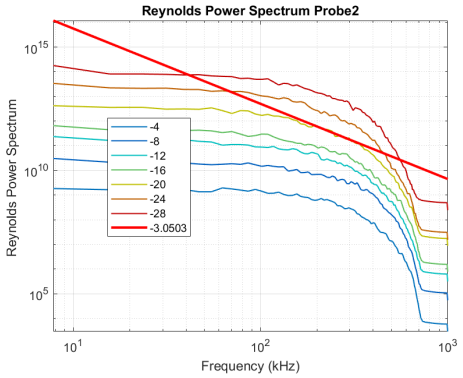

Figure 4.76: Reynolds power spectrum for probe 2. Second experiment without the electrode

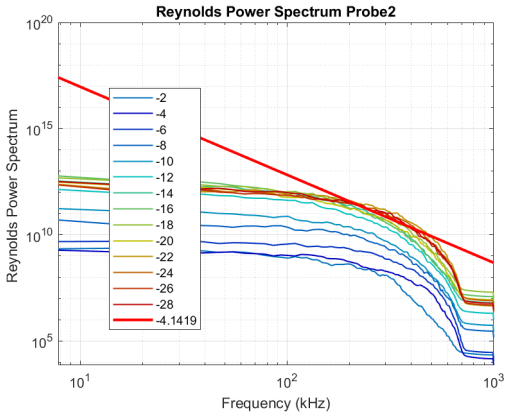

Figure 4.77: Reynolds Stress power spectrum for probe 2. B=0.6T.

4.1.7 $E \times B$ particle flux

The particle flux computation, introduced in 3.3 is presented from Figure 4.78 to Figure 4.82:

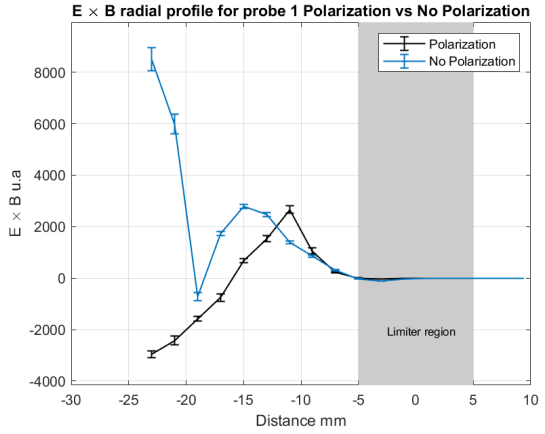

Figure 4.78: $E \times B$ flux radial profile for probe 1. Positive Cycle.

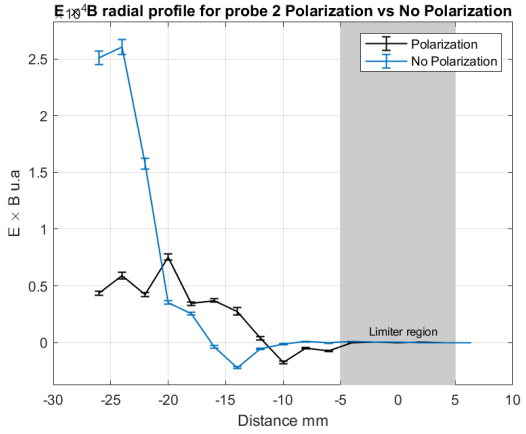

Figure 4.79: $E \times B$ flux radial profile for probe 2. Positive Cycle.

The results for probe 1 tend to be smaller than the values for probe 2. This fact is confirmed by the second experiment. The lower values can be explained with shadows projected by probe 2, that influence the readings. The particle flux is computed from the ion saturation current acquired in pin 1 of probe 1. The ion saturation current profile clearly shows lower values for the same radial positions between the pin 1 and pin 7, the ion saturation current pin for probe 2.

The absolute values for particle transport for the radial position can not be taken as accurate for probe 1, but the variations with the radial profile itself seem to be concordant in both probes. Values of particle transport close to zero in the SOL and limiter region, where plasma is less dense, with values increasing in the inner regions. Just like in the case of the Reynolds profiles, the particle flux seems to be suppressed after applying polarization to the plasma. The radial profiles from the second experiment are presented:

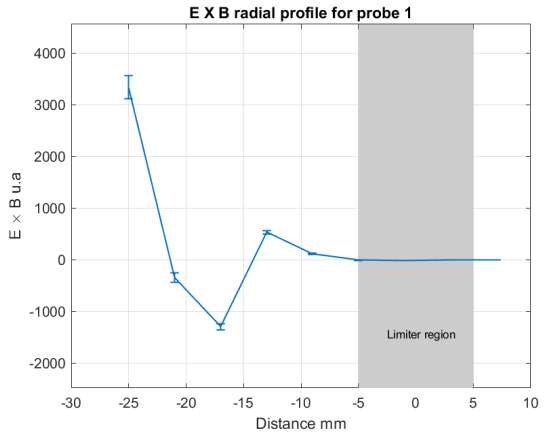

Figure 4.80: $E \times B$ flux radial profile for probe 1.Second experiment without the electrode.

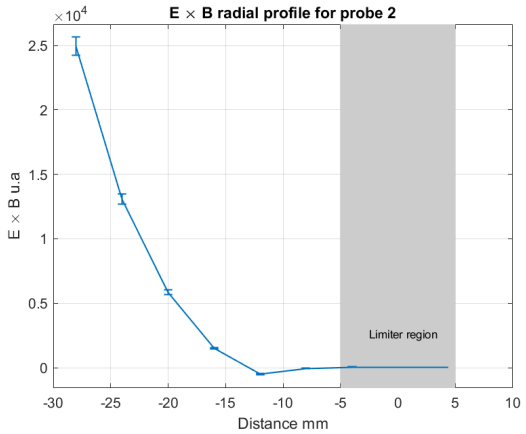

Figure 4.81: $E \times B$ flux radial profile for probe 2. Second experiment without the electrode.

The results for the experiment with higher magnetic field are computed in Figure 4.82.

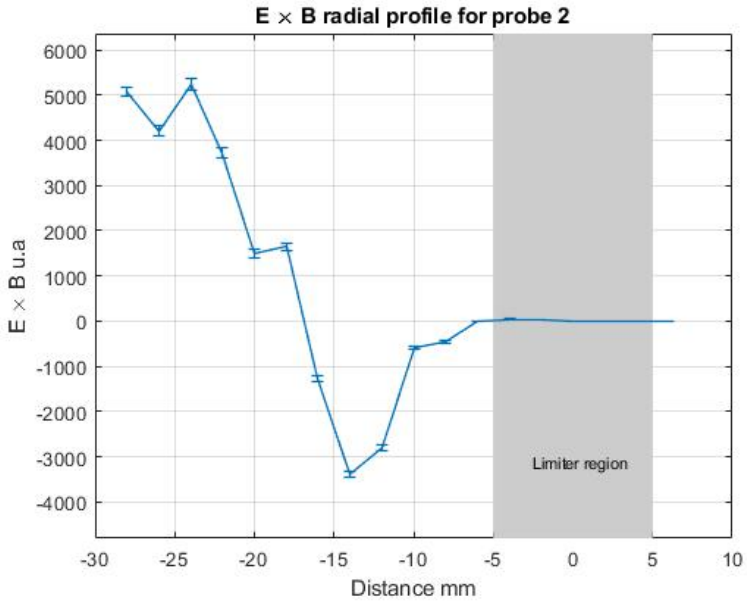

Figure 4.82: Particle flux probe 2. B=0.6T.

The increasing particle flux moving inwards is still visible. Although, the absolute values of the particle flux show a major decrease, comparing to the results obtained for B=0.5 Tesla.

$E \times B$ particle flux power spectrum

The particle flux power spectrum results are presented from Figure 4.83 to Figure 4.89.

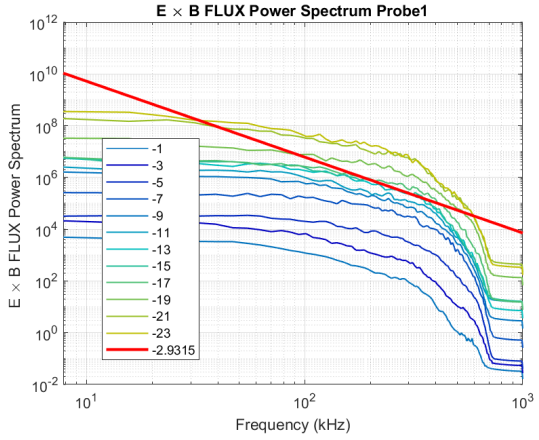

Figure 4.83: E × B flux for probe 1. Positive Cycle

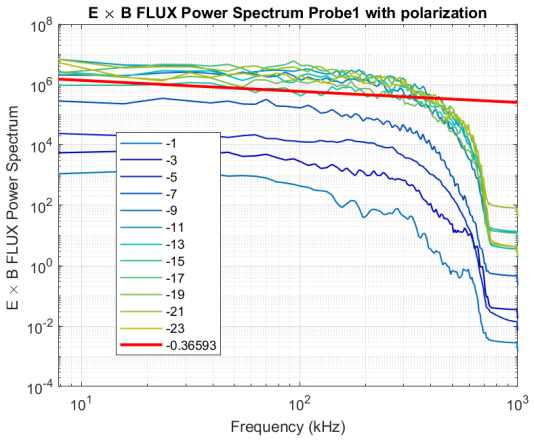

Figure 4.84: E × B flux for probe 1 with polarization. Positive Cycle

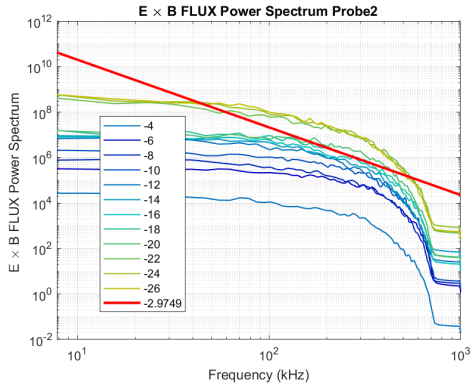

Figure 4.85: E × B flux for probe 2.Positive Cycle

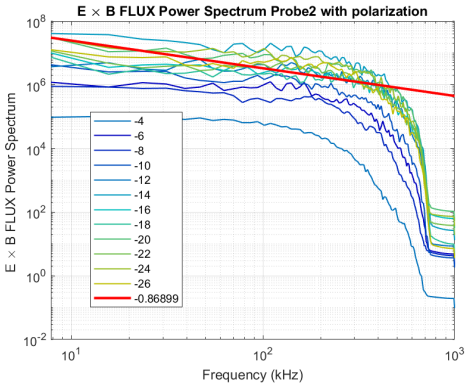

Figure 4.86: E × B flux for probe 2 with polarization.

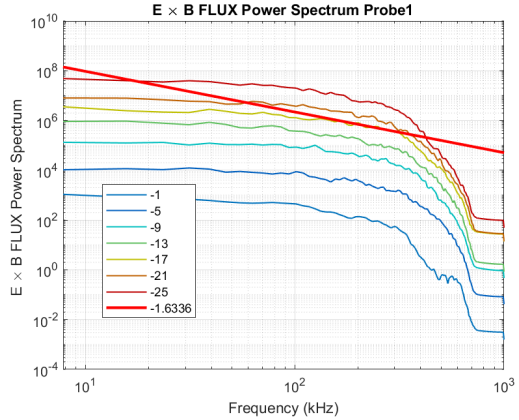

Figure 4.87: E × B flux for probe 1. Second experiment without the electrode.

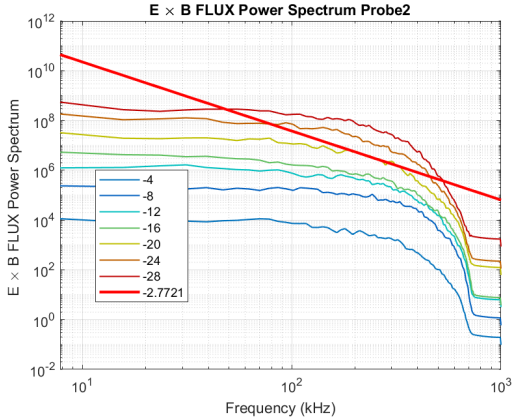

Figure 4.88: E × B flux for probe 2. Second experiment without the electrode.

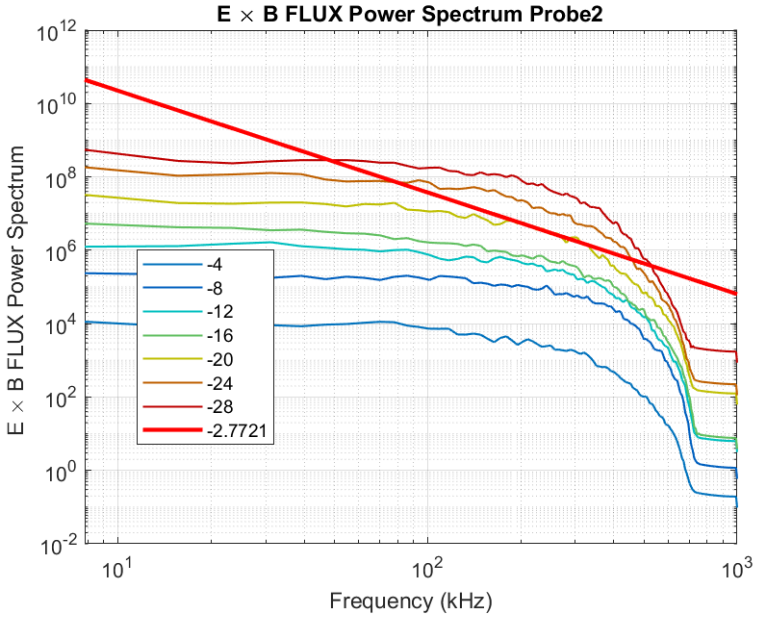

Figure 4.89: E × B flux for probe 2. Second experiment without the electrode

The results show consistently a decrease in the spectral index for the polarization results. This variation is specially evident in the last results for the particle flux. The experiment with higher magnetic field applied, shows a comparable behavior with the polarization results.

4.1.8 Vorticity

The importance of energy and moment transfer between flows and turbulence in fusion plasmas is a topic that has increased in importance recently [61, 62] and the simultaneous existence of multiple scales in turbulence and fluctuations was observed [63, 64]. The experimental measurement of vorticity and vorticity flux in a fusion device is an important achievement since vorticity plays a key role in the transport of energy and particles in plasmas and fluids. The rate of change of vorticity, has its origin in the divergence of the plasma polarization current that provides the main perpendicular part of the charge balance in the quasineutral plasma. Therefore, experimentally measuring vorticity is essential.

The vorticity results obtained during the experiment are presented from Figure 4.90 to Figure 4.95.

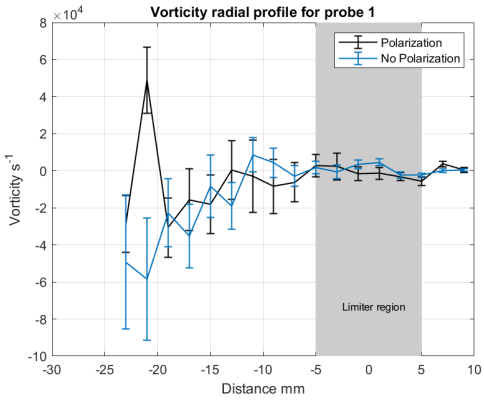

Figure 4.90: Vorticity radial profile for probe 1. Positive Cycle.

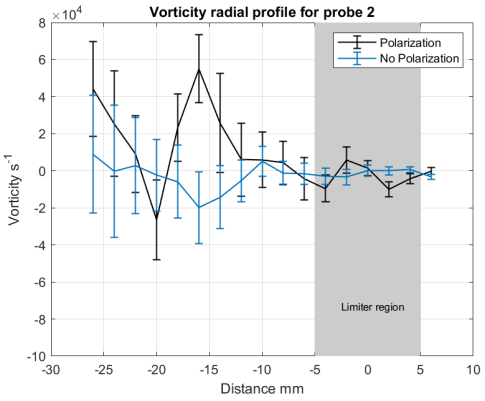

Figure 4.91: Vorticity radial profile for probe 2. Positive Cycle.

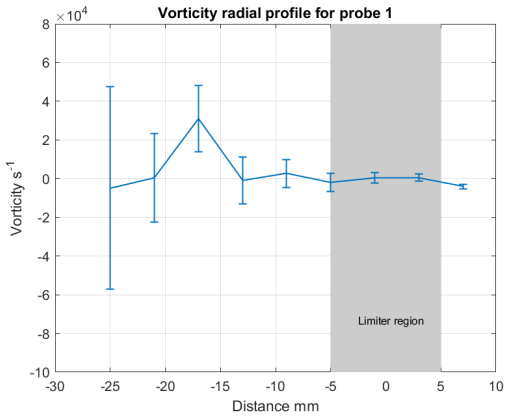

Figure 4.92: Vorticity radial profile for probe 1 without the electrode. Positive Cycle.

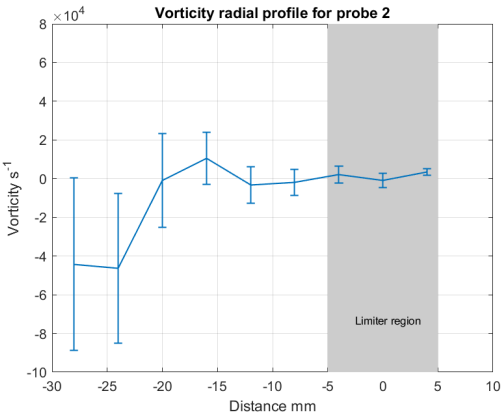

Figure 4.93: Vorticity radial profile for probe 2 without the electrode. Positive Cycle.

The vorticity in the plasma outer region is characterized by fluctuations around zero, and strong variations after the 10/15 millimeter mark. Both profiles from the first experiment and the second one,

without the influence of the electrode, show similar behavior. The vorticity is computed with floating potential signals as introduced in equation 2.16 and it is directly related to turbulence. Inner regions of the tokamak, with higher turbulence, are associated with stronger variations in vorticity as expected. The polarization introduces even bigger variations, which may be associated with a stronger shear layer generated by it. For probe 1, the vorticity grew from $-3 \times 10^4 s^{-1}$ to about $5 \times 10^4 s^{-1}$ between the radial positions [-20mm -22mm]. This result can be compared with the bigger variation during the nonpolarized interval, which occurred between the same positions and has values between $-2.5 \times 10^4 s^{-1}$ to about $-5.8 \times 10^4 s^{-1}$. The variation with the introduction of polarization is 40% times bigger in this specific interval. In general, all radial variation on vorticity where much stronger for the polarized intervals. The vorticity is also computed for a higher magnetic field configuration, presented in Figure 4.94. Results for previous experiments are also showed for comparison in Figure 4.95.

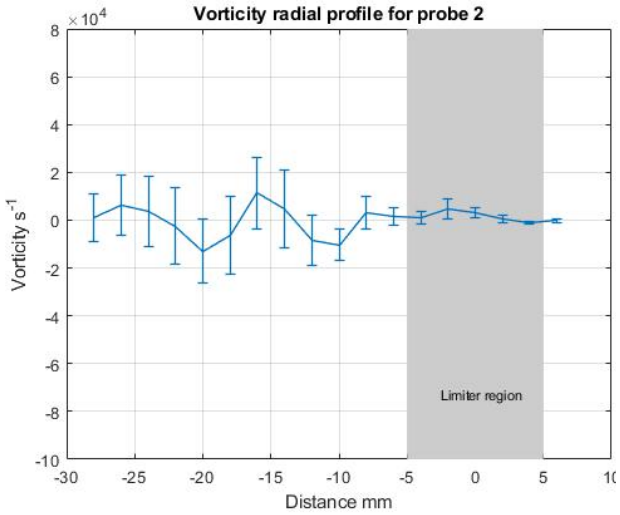

Figure 4.94: Vorticity radial profile for probe 2 without the electrode. B=0.6T.

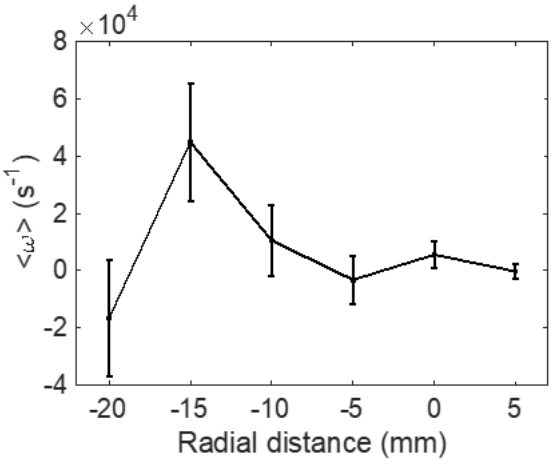

Figure 4.95: Vorticity radial profile from previous experiments[60].

A higher magnetic field is associated with lower fluctuations on vorticity. The stronger variations in vorticity for the third experiment can be detected between 10 and 20 millimeter region inside the limiter. Previous studies agree with constant vorticity values in the SOL and limiter, and a large dispersion in the plasma edge.

The Kurtosis and Skewness of vorticity are computed and presented from Figure 4.96 to 4.99:

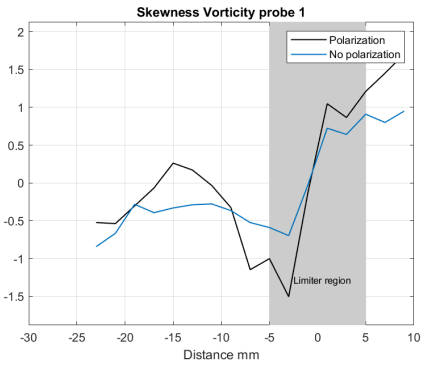

Figure 4.96: Vorticity Skewness for probe 1. Polarization vs No Polarization.

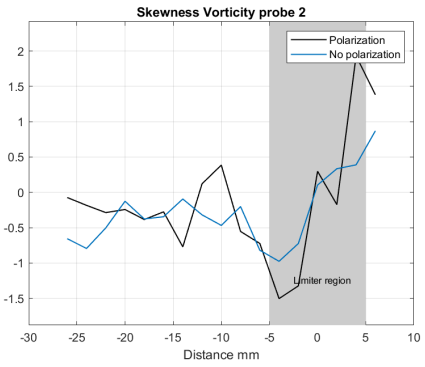

Figure 4.97: Vorticity Skewness for probe 2. Polarization vs No Polarization.

As mentioned in Chapter 2, the skewness is a measure of symmetry of the distribution. For a normal distribution, it is zero. Positive values of skewness are observed in outer positions of the limiter, indicating that the data is skewed to the right, which means that the right tails of the data distribution are long relative to the left ones. As we move from the SOL into the limiter, the values for skewness drop and stays negative for nonpolarized signals, with values close to -0.5. The vorticity measured with polarization applied to the plasma shows stronger variations in the skewness, with a minimum value of -1.5 in the position $4mm$ inside the limiter. In the polarization case, the skewness does not remain always negative as we walk into the plasma, but generally speaking, the values are also negative. Similarly, the negative skewness values are associated with bigger left tails in the distribution.

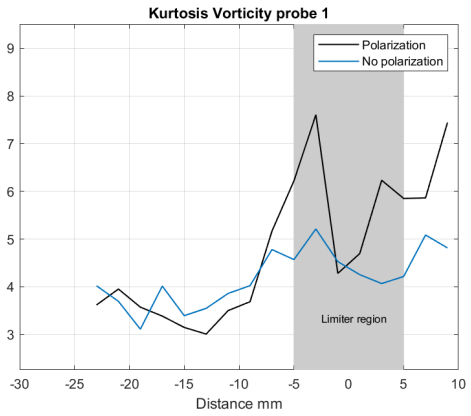

Figure 4.98: Vorticity Kurtosis for probe 1. Polarization vs No Polarization.

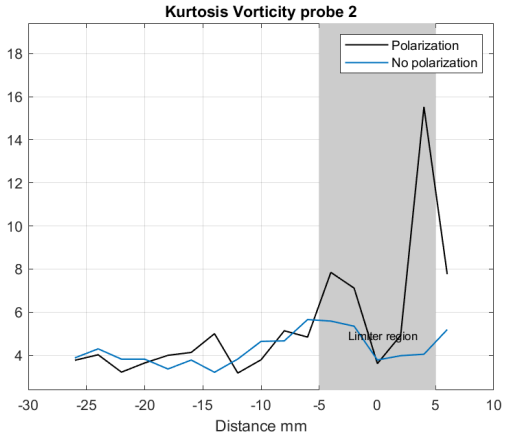

Figure 4.99: Vorticity Kurtosis for probe 2. Polarization vs No Polarization.

The kurtosis is another tool in statistical analyses, that measure how outlier-prone a distribution is, in other words, how much height the data has in the tails of the distribution. The kurtosis value for a standard normal distribution is 3. Kurtosis greater than 3 characterizes distributions more outlier prone, indicating heavy tails. High values of kurtosis are observed near the limiter region, especially for the polarization intervals. Both probes show values greater than 3 during all the radial positions. From the 10 millimeters inside the limiter to the inner regions of the plasma, the kurtosis values seem to be similar between the polarization and no polarization signal.

Vorticity power distribution function

Among various non-Gaussian distributions that emerge from consistent thermodynamical and statistical frameworks [65–67], q-Gaussians, based on the so-called non-extensive statistical mechanics introduced by Tsallis [68], are appealing for their simplicity. Many experimental measurements of distribution functions of particle systems and other physical quantities can be described by non-Gaussian distributions. Q-Gaussians have been employed in the study of probabilistic models [69], space plasmas[70], earthquakes [71] and the solar wind[72]. The q-Gaussian distribution is specified by the pdf:

$$R_q(x) = a\left[1 + (q-1)\frac{x^2}{\lambda^2})\right]^{-\frac{1}{1-q}} \tag{4.1}$$

For $1-(1-q)(x/x0)^2 \geq 0$ and $R_q(x) = 0$ otherwise. Results from Figure 4.100 to 4.122 show the probability distribution function of vorticity obtained from the experimental measurements obtained at different radial positions. The PDFs of the vorticity exhibit fat tails with a q-Gaussian shape typical of a non-equilibrium process. The results are presented from Figure 4.100 to 4.122.

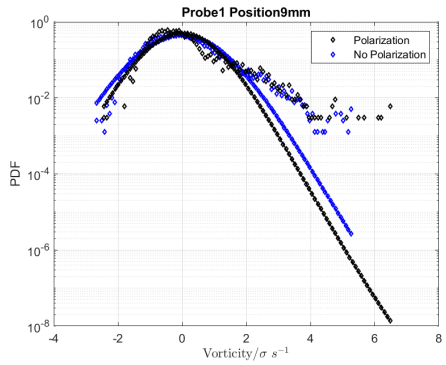

Figure 4.100: Q-Guassian for probe 1 at +9mm position. Positive cycle.

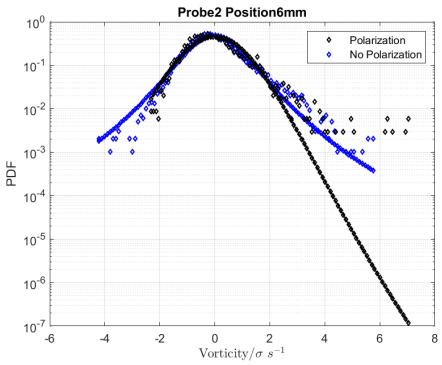

Figure 4.101: Q-Guassian for probe 2 at +6mm position. Positive cycle.

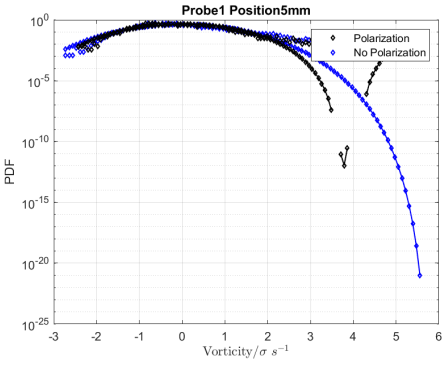

Figure 4.102: Q-Guassian for probe 1 at +5mm position. Positive cycle.

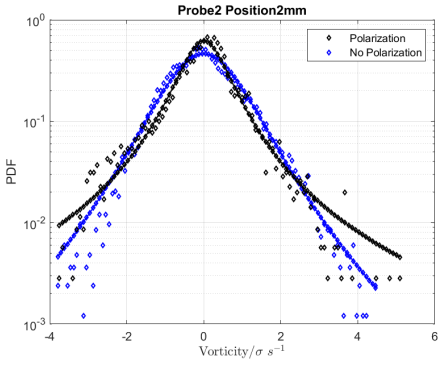

Figure 4.103: Q-Guassian for probe 2 at +2mm position. Positive cycle.

The first set of data fits presented above are the expected result from the vorticity in the SOL region, with a distribution skewed to the right, that could be predicted from the positive values of skewness. The presented distribution is also characterized by heavy tails to the right, especially for the polarized

signals, a result that is expected from the high kurtosis value. After the limiter, the vorticity skewness, for both polarized and nonpolarized signals decreases substantially. In the limiter region, both probes have skewness close to zero, characteristic of a normal distribution. The fits for these regions are presented:

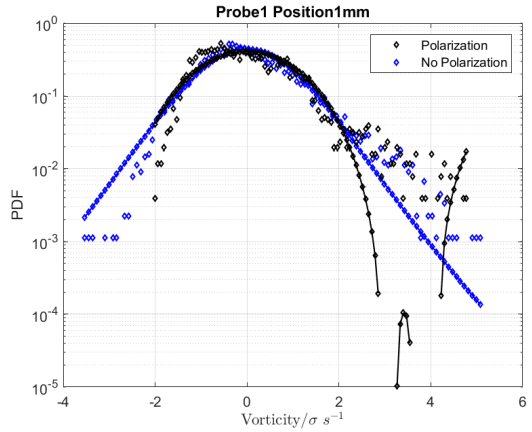

Figure 4.104: Q-Guassian for probe 1 at 1mm position. Positive cycle.

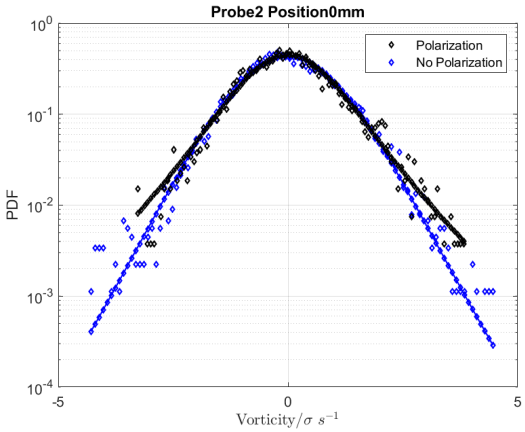

Figure 4.105: Q-Guassian for probe 2 at 0mm position. Positive cycle.

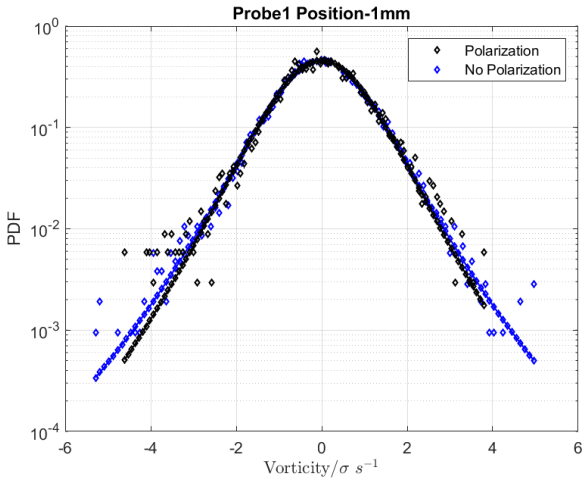

Figure 4.106: Q-Guassian for probe 1 at -1mm position. Positive cycle.

The three positions presented above are clear examples of regions where the vorticity distribution looks like a symmetric normal distribution. Inside the limiter, with the skewness turning negative, and kurtosis values around 4, distributions without symmetry and skewed to the left are expected. The results respecting to some of these inner positions are presented:

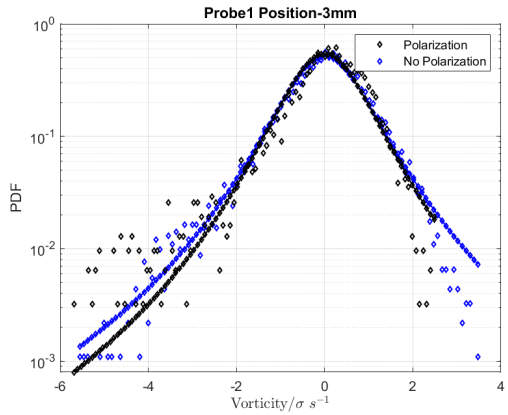

Figure 4.107: Q-Guassian for probe 1 at -3mm position. Positive cycle.

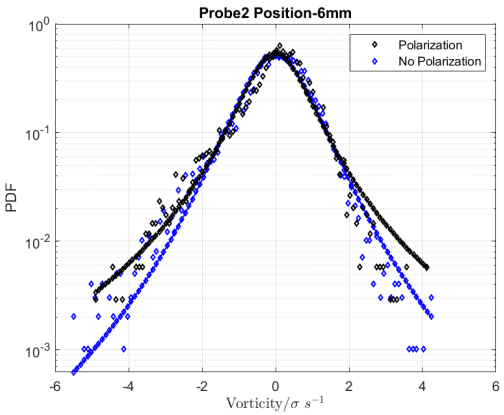

Figure 4.108: Q-Guassian for probe 2 at -6mm position. Positive cycle.

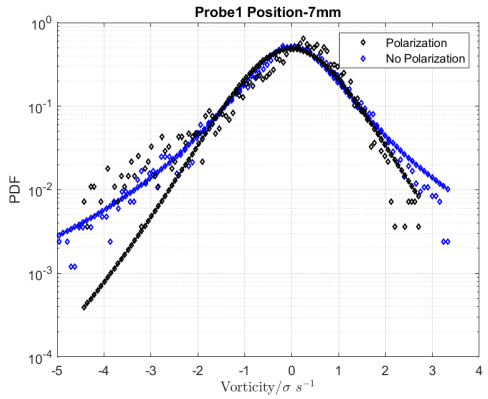

Figure 4.109: Q-Guassian for probe 1 at -7mm position. Positive cycle.

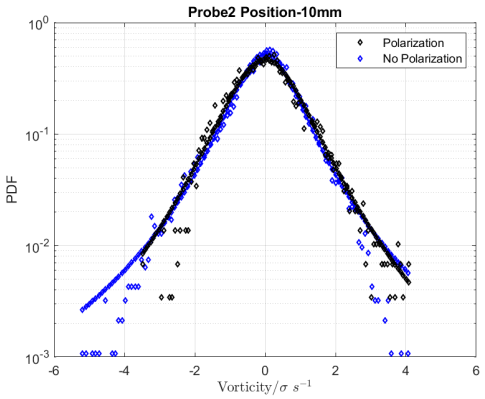

Figure 4.110: Q-Guassian for probe 2 at -10mm position. Positive cycle.

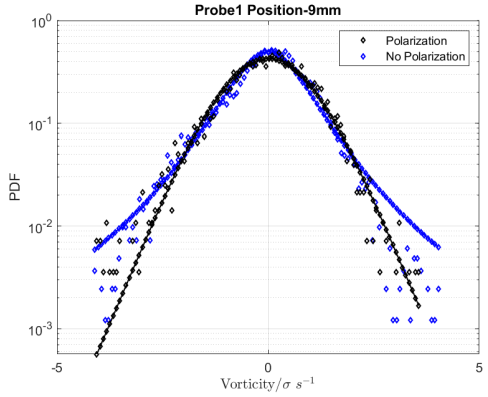

Figure 4.111: Q-Guassian for probe 1 at -9mm position. Positive cycle.

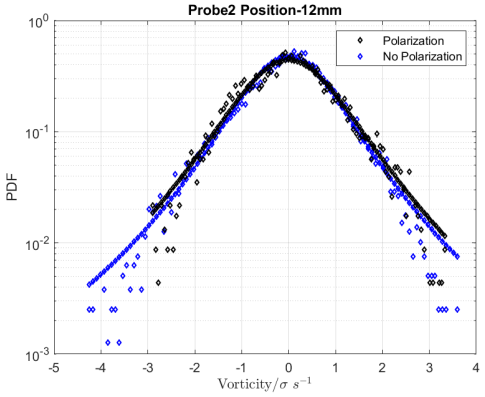

Figure 4.112: Q-Guassian for probe 2 at -12mm position. Positive cycle.

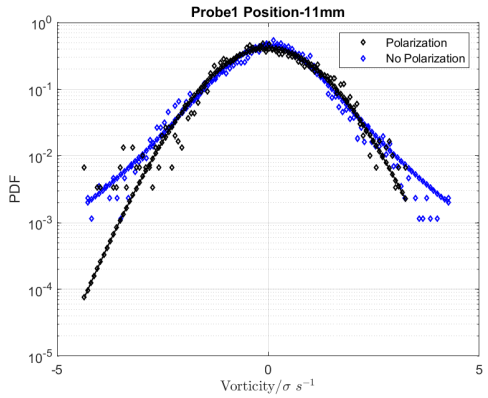

Figure 4.113: Q-Guassian for probe 1 at -11mm position. Positive cycle.

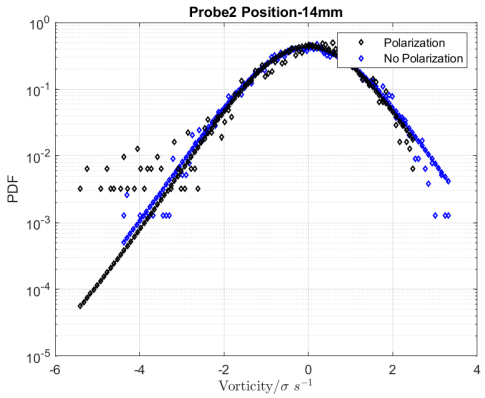

Figure 4.114: Q-Guassian for probe 2 at -14mm position. Positive cycle.

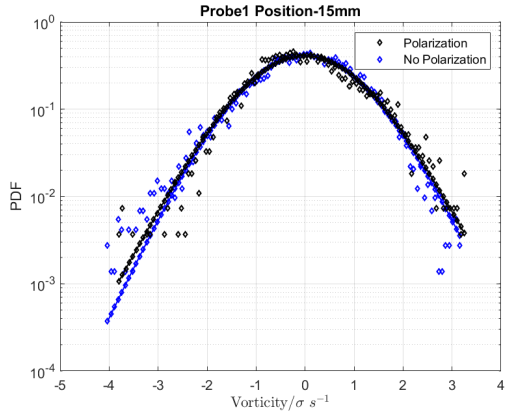

Figure 4.115: Q-Guassian for probe 1 at -15mm position. Positive cycle.

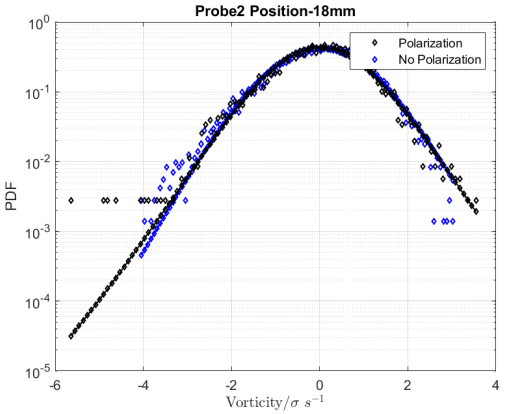

Figure 4.116: Q-Guassian for probe 2 at -18mm position. Positive cycle.

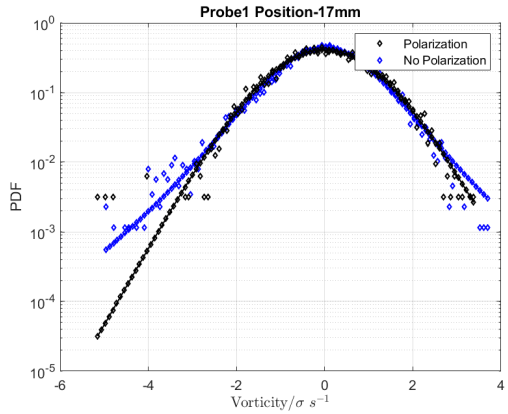

Figure 4.117: Q-Guassian for probe 1 at -17mm position. Positive cycle.

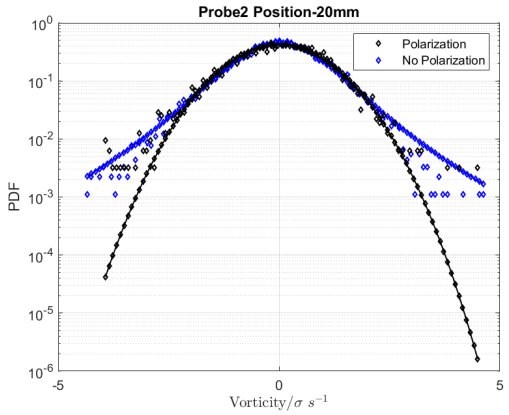

Figure 4.118: Q-Guassian for probe 2 at -20mm position. Positive cycle.

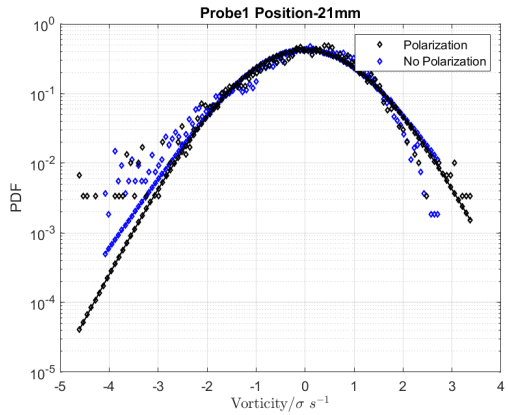

Figure 4.119: Q-Guassian for probe 1 at -21mm position. Positive cycle.

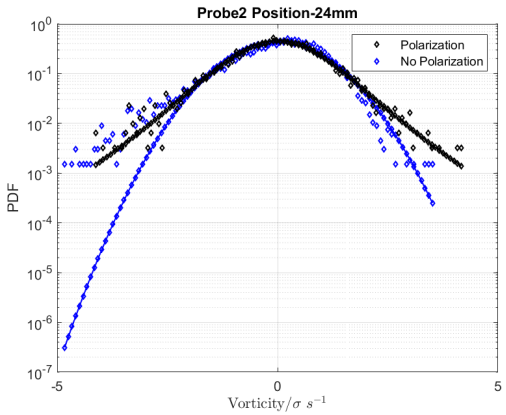

Figure 4.120: Q-Guassian for probe 2 at -24mm position. Positive cycle.

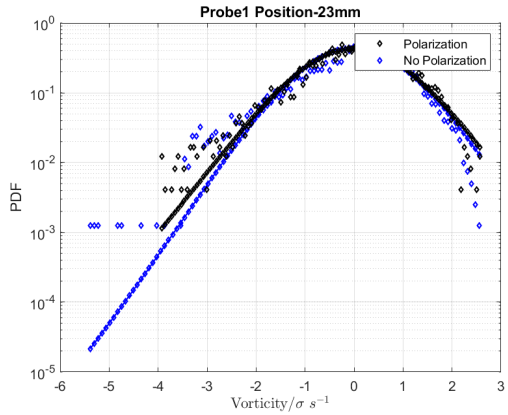

Figure 4.121: Q-Guassian for probe 1 at -23mm position. Positive cycle.

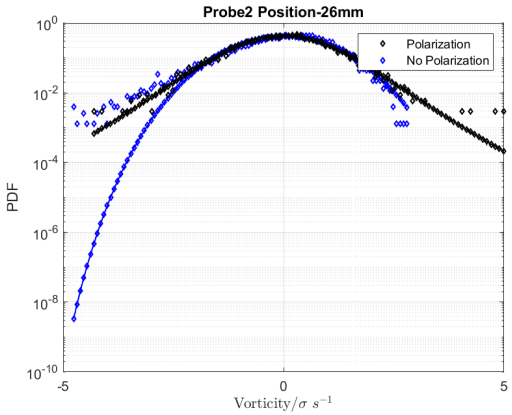

Figure 4.122: Q-Guassian for probe 2 at -26mm position. Positive cycle.

The results show most of the distributions skewed to the left as expected. For easier visualization, the plot of all signals acquired along the radial scan is presented from Figure 4.123 to Figure 4.131:

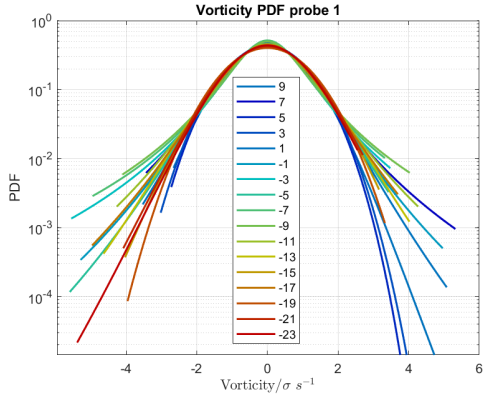

Figure 4.123: Q Gaussian for probe 1. Normalized values.

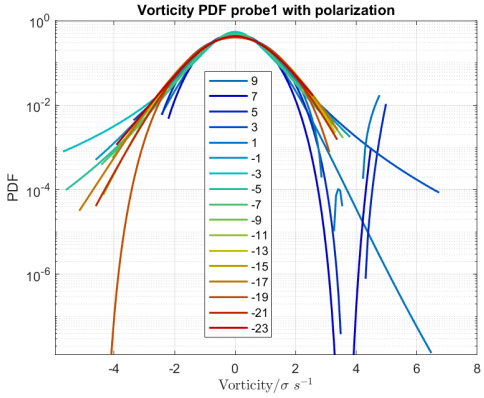

Figure 4.124: Q Gaussian for probe 1 with polarization. Normalized values.

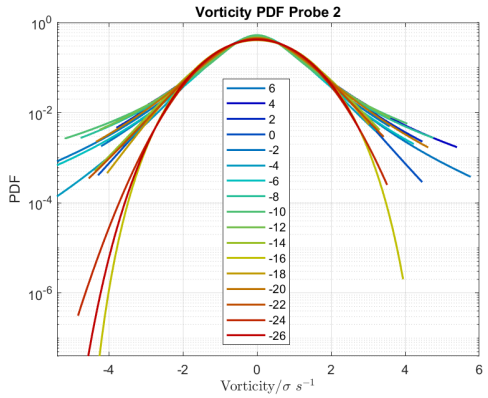

Figure 4.125: Q Gaussian for probe 2.Normalized values.

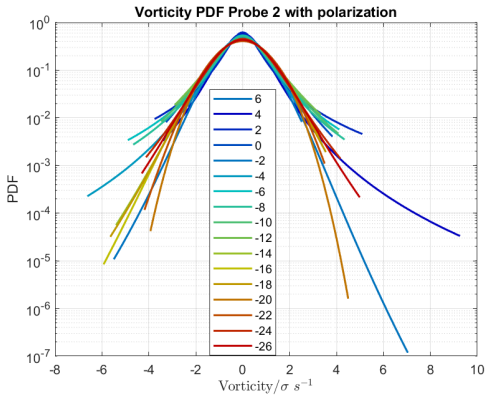

Figure 4.126: Q Gaussian for probe 2 with polarization. Normalized values.

The darker blue fits, representing the PDF of vorticity in the SOL region have pronounced tails to the right. The distribution tails move to the left as we move into the inner regions of the tokamak. A Q-Gaussian without normalization is also presented:

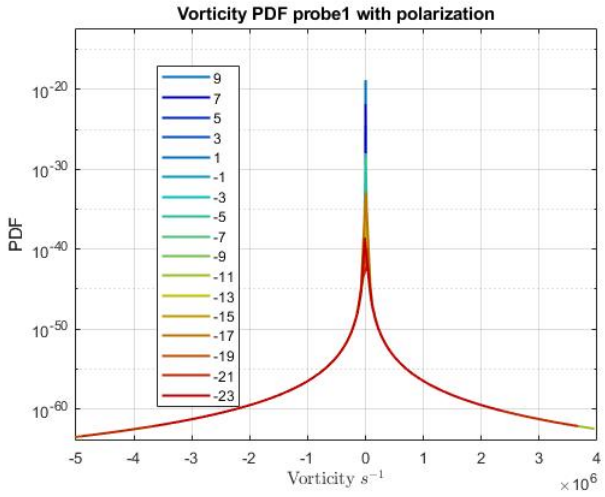

Figure 4.127: Q-Gaussian for probe 1 with polarization and no normalization.

Both probes, with and without polarization show this distribution for the vorticity without normalization. The outer positions represented by blue have distributions more peaked, while inner positions have flattened PDF's with bigger tails. Following with the vorticity PDF for the second and third experiment experiment:

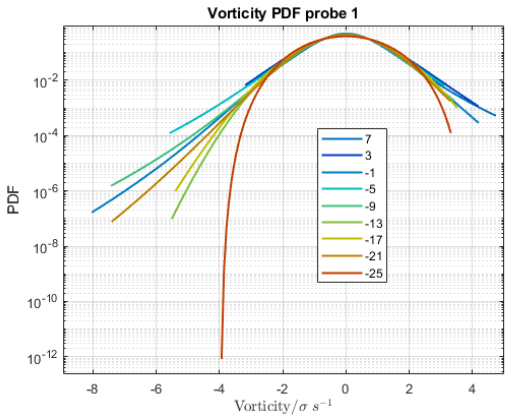

Figure 4.128: Q Gaussian for probe 1.Second experiment without polarization.

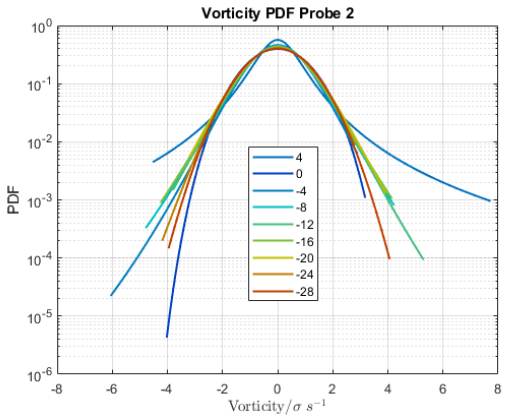

Figure 4.129: Q Gaussian for probe 2. Second experiment without polarization.

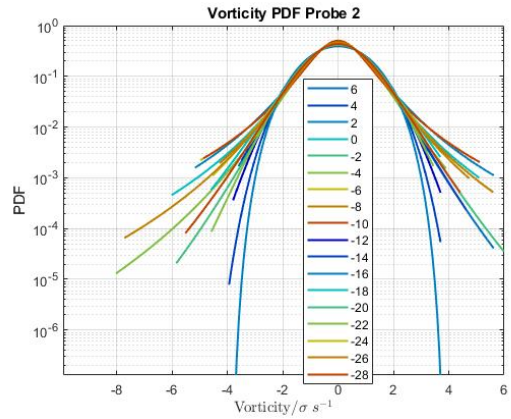

Figure 4.130: Q-Gaussian for probe 2. B=0.6T.

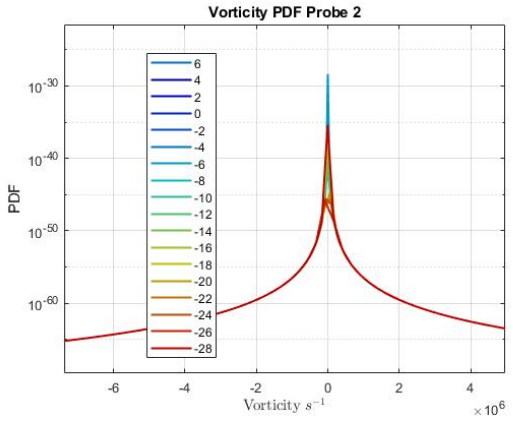

Figure 4.131: Q-Gaussian for probe 2 without normalization. B=0.6T.

The existence of positive tails in pdf distribution is also interesting, because as shown in [73] a similarity exists between transport statistics, particularly for positive transport events, during ELM H-mode and L-mode, where the transport is known to be mediated by radially propagating blob structures. Although the magnitude of the transport varies by a large factor, the results indicate a strong similarity of the underlying joint transport mechanisms.

The experimental study of vorticity is an important achievement in the plasma studies, since it is known to exist in turbulent plasmas, and allows direct comparison with theoretical models. The results show no morphological change in the coherent structures in the plasma boundary region and that the fluctuations in the Reynolds stress, vorticity and vorticity flux can be described by a probability distribution that tends to a universal shape. It was shown that the probability distribution function of the vorticity can be fitted by a q-Gaussian distribution typical of a non-equilibrium process. The similarity of transport mechanisms during ELMy H-mode and L-mode previously observed in [73] make these results also highly relevant.

The factor q on equation 2.33 controls how ”peaked” the distribution is, being closely related to the kurtosis. A q factor close to 1 characterizes a distribution close to a Gaussian, while values greater than

1 are associated with flattened tails with tails.

The vorticity PDFs become broader as we move from the SOL to the edge regions of the plasma. The PDF tails are typical of strongly correlated systems, implying the existence of intermittent coherent structures.

The Q-factor, obtained as a fit parameter from the adjusts previously presented, is computed as a function of the radial position. The results are presented from Figure 4.132 to Figure 4.137:

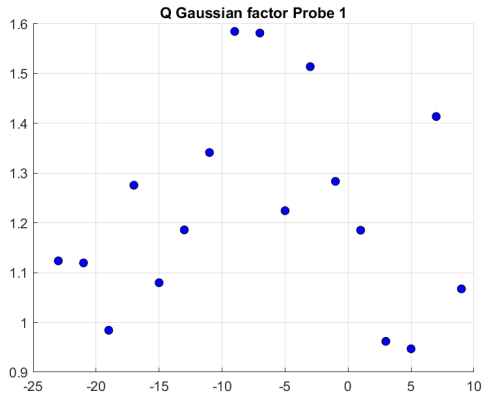

Figure 4.132: Q Factor for probe 1. Positive cycle.

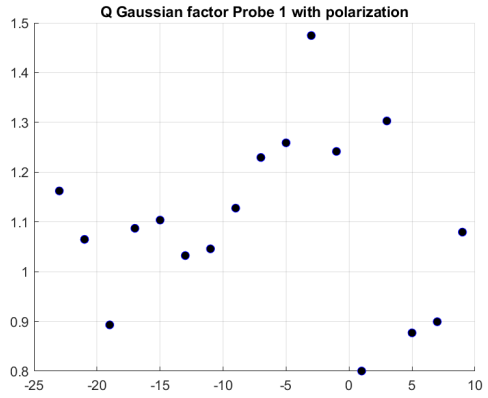

Figure 4.133: Q Factor for probe 1 with polarization. Positive cycle.

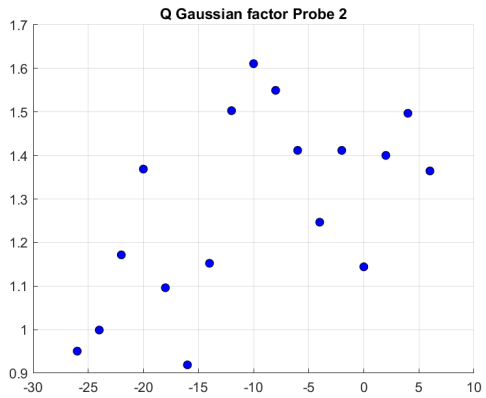

Figure 4.134: Q Factor for probe 2. Positive cycle.

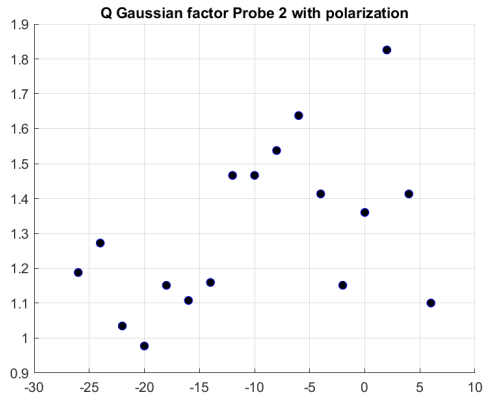

Figure 4.135: Q Factor for probe 2 with polarization. Positive cycle.

The factor q varies through the radial positions. The behavior of this variation is not exactly clear but, for both probes, the distribution of vorticity seems to have a maximum value of q around the position -10mm, that can be related to the spiked value of kurtosis on that same point. The value grows from the limiter until this position, decaying then to smaller values in the inner regions. For the polarization case, the maximum value occurs in outer regions of the plasma, but also decaying when moving to inner positions.

For the second experiment, without the electrode, the q factor variation with the radial position yields:

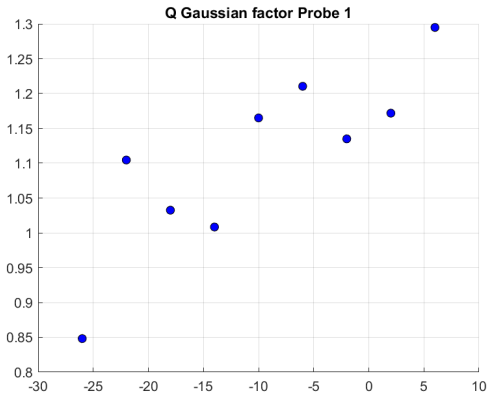

Figure 4.136: Q Factor for probe 1.Second experiment without the electrode.

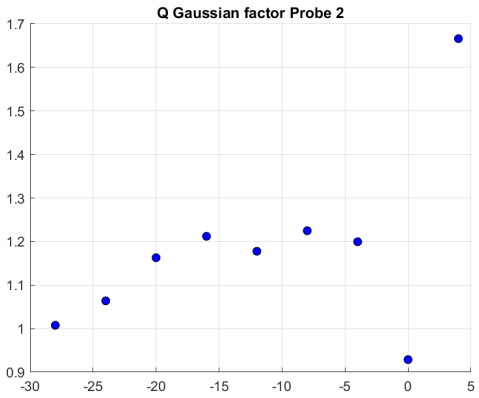

Figure 4.137: Q Factor for probe 2. Second experiment without the electrode.

In this case the same decreasing trend for the q adjust factor of the gaussian is obtained, but this time, the decaying behavior is more clear, with the distribution tending to a normal Gaussian(q=1) as we move into inner regions of the plasma. The results for the third experiment resemble results from polarization on probe 2, with a strong decrease in the q-Gaussian factor after the position 10 millimeter inside the limiter. This is the same radial position where strong variations of vorticity are observed, as shown in Figure 4.94.

Figure 4.138 shows results from the previous experiment at ISTTOK:

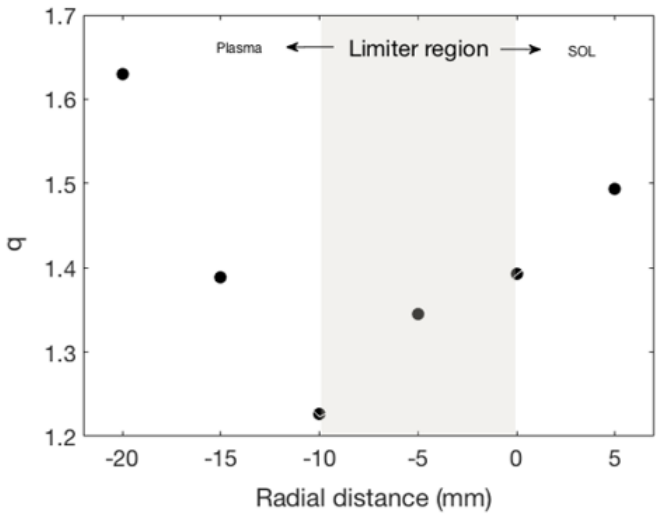

Figure 4.138: Radial profile of the q parameter resulting from the fit of a q-Gaussian to the probability distribution function of the vorticity. Results from a previous experiment at ISTTOK

In this case, a dip is observed in the radial profile, close to the limiter position with a minimum q value of 1.2 closer to that of a Gaussian distribution. Values of q around 1.2 in this position were also obtained during the experiment without the electrode, but in this case, there was evidence of a decaying trend for the q factor, while moving into the inner regions of the plasma, contrary to the increase showed in Figure 4.138.

Vorticity Power Spectra

The vorticity power spectrum is performed through all signals after the limiter. The power spectrum in SOL is weaker and more affected by the acquisition system noise, not being represented here. The results for the vorticity power spectra are presented from Figure 4.139 to Figure 4.142. Worth noticing that the results are plotted in a logarithmic scale, so the fitted line corresponds to the decay factor, also known as spectral index:

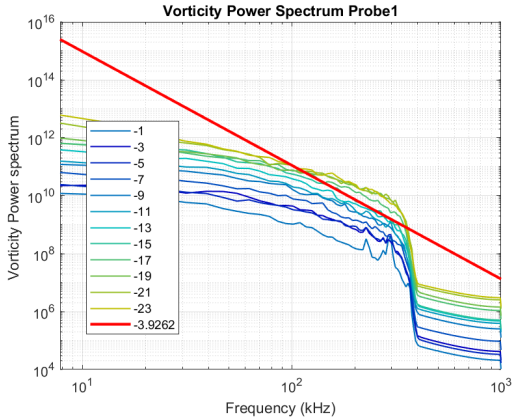

Figure 4.139: Vorticity power spectrum for probe 1. Positive Cycle

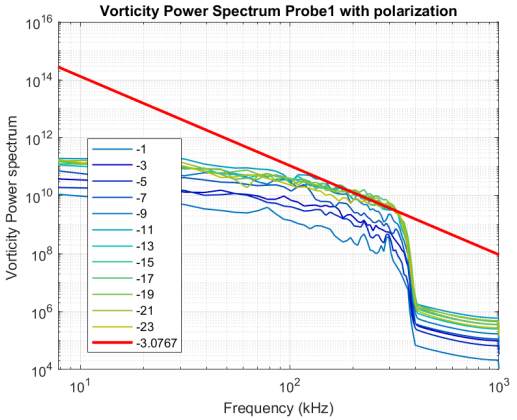

Figure 4.140: Vorticity power spectrum for probe 1 with polarization. Positive Cycle

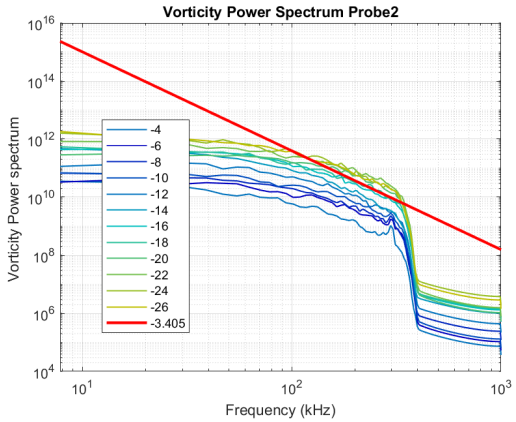

Figure 4.141: Vorticity power spectrum for probe 2. Positive Cycle

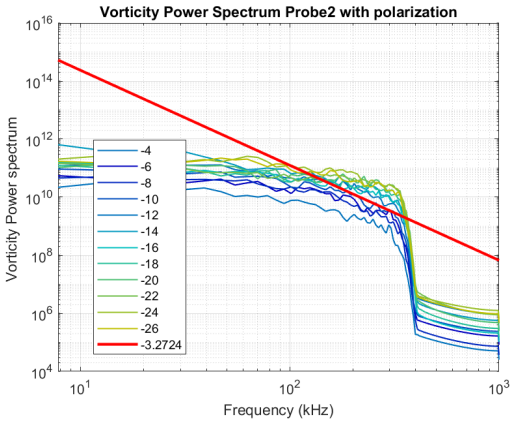

Figure 4.142: Vorticity power spectrum for probe 2 with polarization. Positive Cycle

The exponential decay is confirmed in the previous results, giving a spectral index for vorticity around -4 for probe 1 and -3.4 for probe 2. There is some evidence that the polarization decreases the decay rate of the presented turbulent process, with decays of -3 and -3.2 for probe 1 and probe 2 respectively.

The results can be compared to the ones obtained from previous experiments at different facilities and from simulations, presented in Figure 4.143.

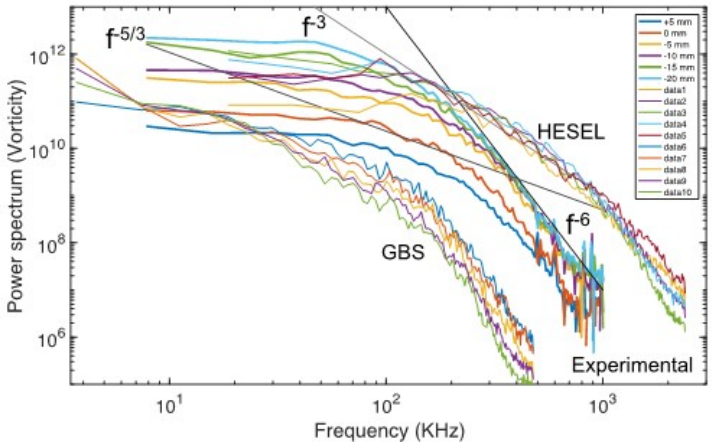

Figure 4.143: Vorticity Power spectrum from previous experiments. The ”Experimental” result correspond to previous experiences at ISTTOK

x

During this work, the exponential decay is obtained with linear regression, at a fixed range of frequencies, in this case, from 300kHz to 400kHz. From a simple visual analysis, the decay has a dependency on the position. After some testing, this was confirmed, with the slope of the curve varying. A three-dimensional analysis of the vorticity power spectrum is presented in Figure 4.144:

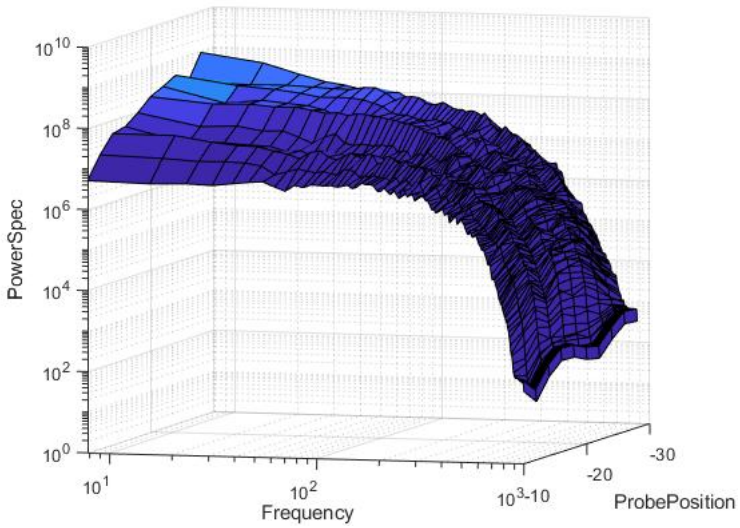

Figure 4.144: 3 Dimensional Vorticity Power Spec for probe 1

The frequency inflection point where the power spectrum starts to decay varies with the radial position. Outer positions start to decay at lower frequencies, comparing to inner positions. Since the linear regression is performed over a constant frequency interval, this explains the dependency of the spectral index with the position. All the spectral indexes during this experiment are then calculated for a fixed radial position, 18 and 15 millimeters inside the limiter, respectively for probe 1 and probe 2.

The vorticity power spectrum for the other two experiments are presented from Figure 4.145 to Figure 4.147:

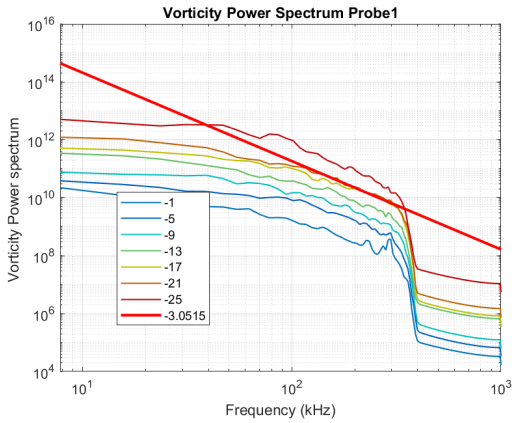

Figure 4.145: Vorticity power spectrum for probe1 .Second experiment without polarization.

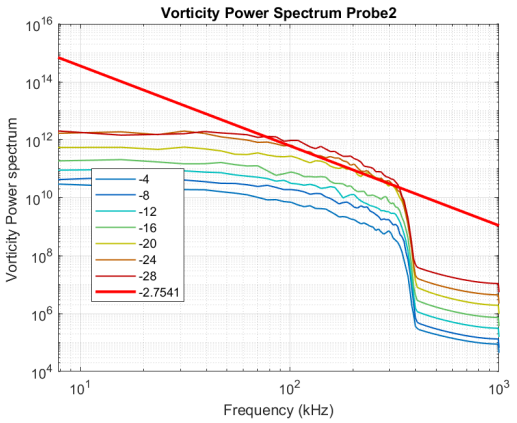

Figure 4.146: Vorticity power spectrum for probe 2. Second experiment without polarization.

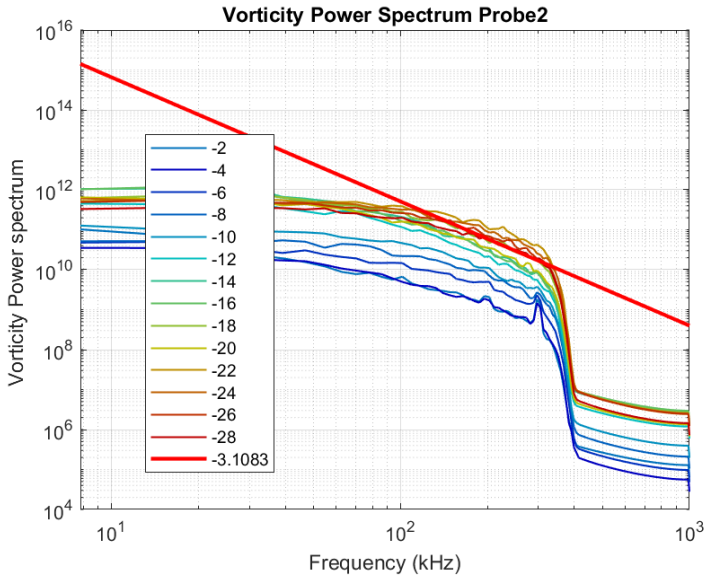

Figure 4.147: Vorticity Pwer spectrum for probe 2. B=0.6T.

The spectral indexes for the second experiment are taken in the closest radial position compared with the first one, since the scan here was done in steps of 4 millimeters instead of 2.

Results suggest that a high magnetic field may not be related with variations on the spectral index for the vorticity, with the process decaying at the same rate as seen the previous results. There is evidence in the previous figures that the decay starts at higher frequencies for the polarization results.

Vorticity Flux

In [74] it is shown that for ExB-dominated turbulent flows, which have azimuthally invariant fluctuation statistics, the vorticity flux is related to the turbulent Reynolds stress and Reynolds force F_θ^R exerted by the fluctuations upon the background plasma The vorticity flux, previously introduced in equation 2.17 is computed and presented from Figure 4.148 to 4.151:

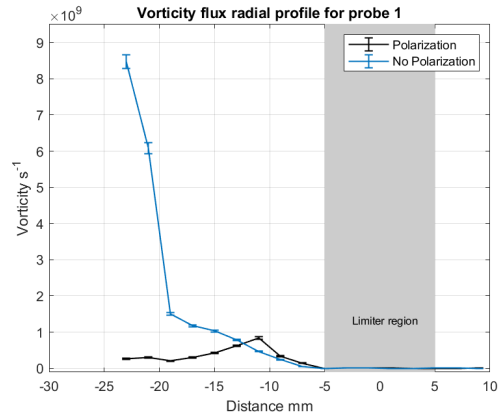

Figure 4.148: Vorticity flux radial profile for probe 1. Positive Cycle.

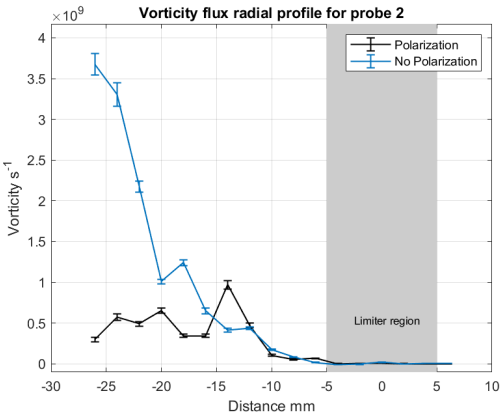

Figure 4.149: Vorticity flux radial profile for probe 2. Positive Cycle.

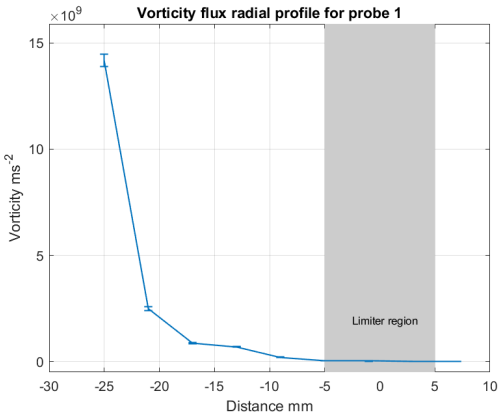

Figure 4.150: Vorticity flux radial profile for probe 1. Second experiment without the electrode

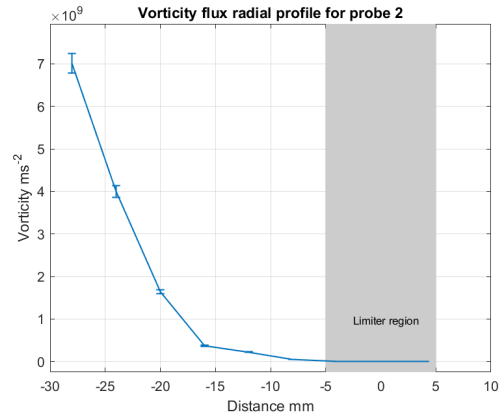

Figure 4.151: Vorticity flux radial profile for probe 2. Second experiment without the electrode

The vorticity flux is close to zero until 15 millimeters into the limiter. After, high flux values are observed with a maximum value close to $1 \times 10^{10} ms^{-2}$ for probe 1 and $4 \times 10^{9} ms^{-2}$. The magnitude and radial profile for both experiments are comparable. The polarization reduces the vorticity flux dramatically in the inner regions, with a maximum value close to $1 \times 10^{9} ms^{-2}$ for both probes. The maximum value of vorticity flux occurs in 11 and 14 millimeters inside the limiter, for probe 1 and probe 2 respectively. The major decrease in the flux is associated with the stronger shear layer generated by the polarization in this region. The strong shear layer de-correlates the turbulent events, reducing the vorticity flux up to 90% across the most inner studied regions of the tokamak.

The same increase in the shear layer occurs when looking at higher magnetic field configurations as presented in Figure 4.152. The results from previous experiments are also presented in Figure 4.153

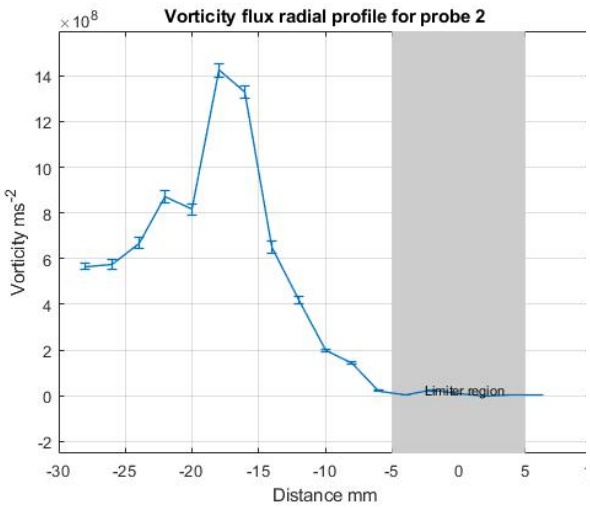

Figure 4.152: Vorticity flux for probe 2. B=0.6T.

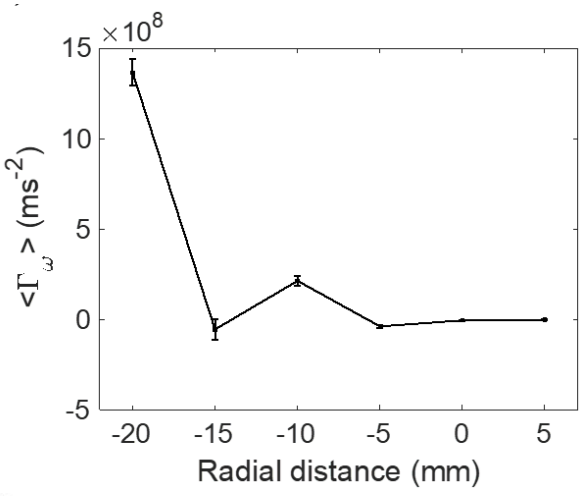

Figure 4.153: Vorticity flux from previous experiments at ISTTOK[60].

In this case, the vorticity flux start do decrease after 20 millimeter inside the limiter. Externally to this position, the behavior resembles the previous experiments. The higher magnetic field configuration suggested a decrease in the vorticity flux in inner regions of the plasma, without the polarization. The results again can be compared to the ones with polarization for the first experiment, that shows fluxes up to 10 times smaller, comparing to the non polarization results.

These results show that the vorticity flux may strongly contribute to the shear flow amplification in the plasma edge region.

Vorticity Flux Power Spectrum

The vorticity flux power spectrum for the three experiments is presented from Figure 4.154 to 4.158:

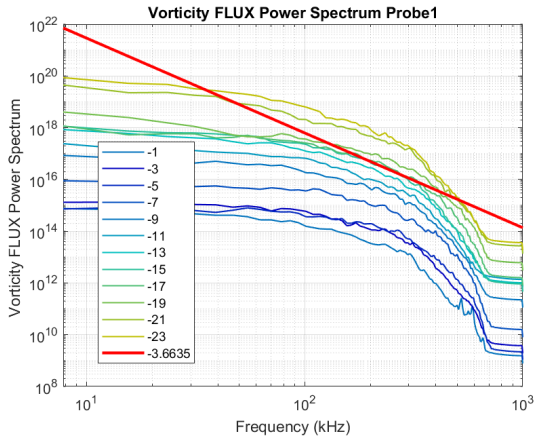

Figure 4.154: Vorticity flux power spectrum for probe 1. Positive Cycle

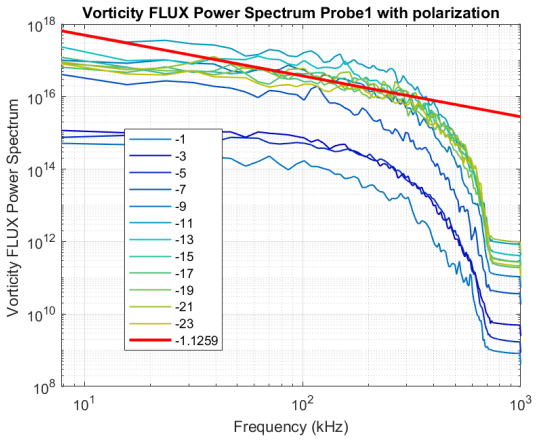

Figure 4.155: Vorticity flux power spectrum for probe 1 with polarization. Positive Cycle

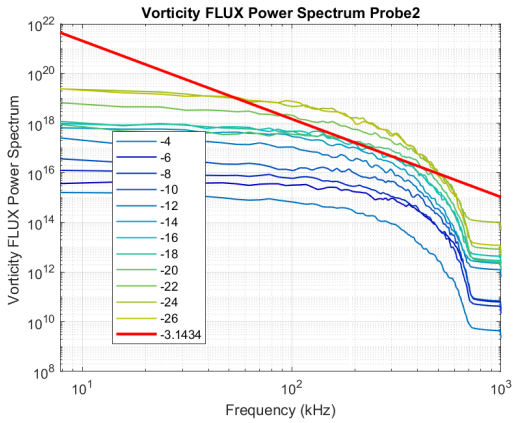

Figure 4.156: Vorticity flux power spectrum for probe 2. Positive Cycle

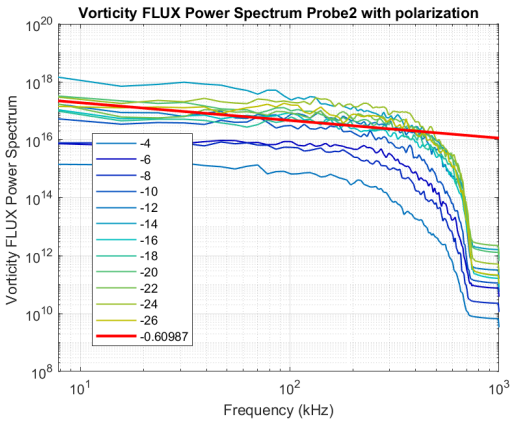

Figure 4.157: Vorticity flux power spectrum for probe 2 with polarization. Positive Cycle

The probe 1 shows higher values of vorticity flux. Not only that, but the decay of the process also occurs at a faster rate. The spectral index for the vorticity flux on probe 1 is consistently higher than in the probe 2. For both probes, the polarization has lower spectral indexes. The results for the third experiment with B=0.6T are presented in Figure 4.158:

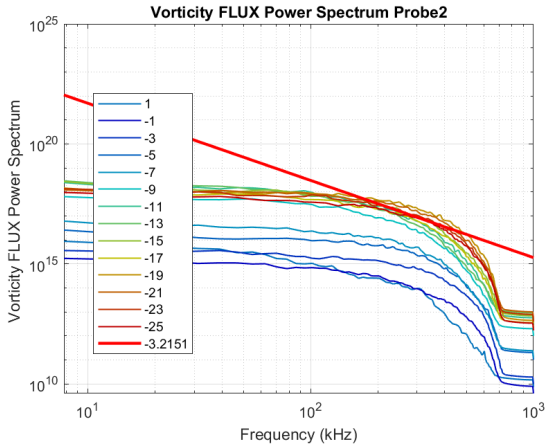

Figure 4.158: Vorticity flux power spectrum for probe 2. B=0.6T.

There is no evidence that increasing the magnetic field increases the rate of the decay with frequency, with a spectral index of 3.21.

Chapter 5

Conclusions

The main goal of this thesis was to study turbulent processes in plasma edge and experimentally estimate the vorticity on ISTTOK tokamak, using a Langmuir probe array.

The presence of a shear layer inside the limiter is detected through all profiles computed. The results presented in the previous section, show strong evidence that polarization clearly has impact in plasma confinement. The shear amplification on electric fields is evident, and has effects in all quantities analyzed through this work. The results show that the vorticity flux may strongly contribute to the shear flow amplification in the plasma edge region. The particle flux and vorticity flux are closely related during all experiments. Strong variations of the correlation length are observed around the limiter position. The clear variation of this correlation length with the radial position strongly suggests that the correlation lengths is affected by the presence of a self generated shear layer on the Tokamak.

It was observed that the vorticity is constant in the SOL and limiter region but in the plasma edge, where the ExB shear flow is higher a larger dispersion is observed in the vorticity measurements. The observed dispersion is not unexpected as theoretical models have predicted that the magnitude of the shear layer leads to selectivity of the vorticity [75]. In this work it was shown that in the absence of the sheared flow, the axial (perpendicular to the plane) vorticity field would be rather homogeneous and isotropic while a sheared flow carries an associated constant axial vorticity that is added to the background vorticity. The vorticity is well fitted by a Q-Gaussian distribution, with flattened distributions and heavier tails for inner positions, and sharper distributions for outer regions, which can be seen at Figure 4.127. The PDF tails are typical of strongly correlated systems, implying the existence of intermittent coherent structures.

The poloidal velocity increases as we move into inner radial positions of the tokamak. All the results, from both methods agree that the poloidal velocity in the SOL region show little variations along the radial positions analyzed. Strong variations in the poloidal velocity are observed in inner regions, around 5 millimeters inside the limiter with the S(k,w) and correlation method. Poloidal velocity is also affected by the polarization, with much higher velocities in the inner regions of the tokamak. All the previous mentioned results confirm the presence of the shear layer, and the amplification of it with polarization. The results obtained are similar to previous observations in JET Tokamak[59]. The shear layer effect,

in the reduction of the correlation length of turbulent events, was also observed. The results show evidences of multiple radial scale lengths in the plasma boundary region. PDFs of turbulence radial coherence are modified in the proximity of the velocity shear layer, which remains near marginal stability in the proximity of the LCFS, like previously observed in JET[59].

Experiments with higher magnetic field also show impact on the confinement conditions as expected, with lower values of Reynolds stress, particle flux, vorticity flux and vorticity. These results can be compared to the ones from the plasma signals with polarization.

5.1 Future Work

Should be interesting analyze in more detail the variation of the spectral index with the radial position. Along this work, this variation was clearly visible in the power spectrums presented. There is also evidence that the inflexion point of the power spectrums varies with the radial position.

Since the reason for this results is not evident, further experiments would be needed. The results for the higher magnetic field configuration where interesting, many times resembling results from the polarization with lower magnetic fields. Analyzing the plasma with both, high magnetic field and polarization, could give some fascinating results. Unfortunately, the electrode that polarized the plasma discharged malfunctioned after the first experiment presented in this thesis, so i was not able to do that. There is some evidence that the plasma was disturbed by the electrode. To avoid this, new experiments with the device placed closer to the limiter, further from the plasma, should be done. It would also be interesting to perform correlation length measurements with ion saturation probes. The present probe configuration do not allow that since the ion saturation current pins of the probe have a poloidal separation.

Noise was a problem during this work. The noise signal presented in Figure 3.19 shows how spread through all spectrum the signal is, which makes him hard to mitigate during the data analysis. Noise studies would be important, understand where it is coming from and finding ways to attenuate it, would help all future works done in the ISTTOK.

Future work will also focus on the comparison of the results with numerical simulations, such as 2D numerical turbulent interchange model HESEL[76] and GBS[77] code and on performing similar measurements in larger fusion devices to allow direct comparison between L and H-mode.

Bibliography

[1] IEA. *World Energy Outlook 2017*. IEA, 2017. doi: 10.1787/weo-2017-en.

[2] IEA. *The average share of electricity from renewable energy sources in the EU*. EUROPEAN COMMISSION, 2017. EUROSTAT, Directorate E: Sectoral and regional statistics Unit E.5: Energy.

[3] URL `http://www-fusion-magnetique.cea.fr/gb/fusion/physique/demo_ntt.htm`. Accessed: 12/05/2019.

[4] J. H. E. Proll. *Trapped-particle instabilities in quasi-isodynamic stellarators*. 2014. Thesis.

[5] Mendes, S. Vaz. Characterization of the turbulent transport in the edge plasma of the tokamak isttok. 2019.

[6] W. Fundamenski. Chapter 6: Scrape-off layer transport on jet. *Fusion Science and Technology*, 53(4):1023–1063, 2008. doi: 10.13182/FST08-A1746. URL `https://doi.org/10.13182/FST08-A1746`.

[7] S. I. KRASHENINNIKOV, D. A. D'IPPOLITO and J. R. MYRA. Recent theoretical progress in understanding coherent structures in edge and sol turbulence. *J. Plasma Physics*, 74:679–717, 2008.

[8] P. D. et al. *Physics of Plasmas*, 19, 2012. doi: 10.1063/1.4751473.

[9] B. Gonçalves and I. Henriques and C. Hidalgo and C. Silva and H. Figueiredo and V. Naulin and A H. Nielsen and J.T. Mendonça. *Radial structure of vorticity in the plasma boundary of ISTTOK tokamak*, 2018. The experimental results presented in this paper, allowing for the first time a direct comparison with theoretical models, show that the vorticity flux feeds into the shear flow in the tokamak plasma edge region.

[10] Burton, W.B. and Kuijpers, J. and Heuvel, Edward and Laan, H. and Appenzeller, I. and Bahcall, J. and Bertola, F. and Cassinelli, Joseph and Cesarsky, C. and Engvold, O. and McCray, R. and Murdin, P. and Pacini, F. and Radhakrishnan, V. and Sato, K. and Shu, F. and Somov, B. and Sunyaev, R. and Tanaka, Y. and Kaw, Predhiman. *Nonequilibrium Phenomena in Plasmas*. 01 2005. ISBN 978-1-4020-3108-3. doi: 10.1007/1-4020-3109-2.

[11] Budaev, V.P. and Ohno, Noriyasu and Masuzaki, Suguru and Morisaki, Tomohito and Komori, A. and Takamura, S. Extended self-similarity of intermittent turbulence in edge magnetized plasmas. *Nuclear Fusion*, 48:024014, 01 2008. doi: 10.1088/0029-5515/48/2/024014.

[12] J. B. Taylore. Diffusion of plasma ions across a magnetic field. *The Physics of Fluids*, 4, 1961. It is shown that the flux can be considered in three parts; one depends on the electric field correlation function and the others on the dynamic friction, which is related to the correlation function by Nyquist's theorem.

[13] B. Gonçalves . *20th IAEA Fusion Energy Conference*, November 2004. Vilamoura, Portugal.

[14] C. Hidalgo et al . *31st EPS Conference on Controlled Fusion and Plasma Physics*, London, UK, 28 June-2 July 2004.

[15] E. Sanchez et al . *Journal of Nuclear Materials*, 337-339:376–380, March 2005. Two-dimensional fluid simulations of scrape-off layer (SOL) turbulence with non-constrained energy content (flux driven) are characterized by profile relaxation and strong outward bursts of density. The ballistic propagation extends well beyond the e-folding length of the SOL.

[16] "B. Gonçalves and C. Hidalgo and M.A. Pedrosa and R. O. Orozco and E. Sánchez and C. Silva". *Phys. Rev. Lett*, 96, 2006. 145001.

[17] C. Hidalgo et al. *Physical Review Letters*, 108, 2012. 065001.

[18] B. Gonçalves et al. *Journal of Nuclear Materials*, 337–339:376–380, Mar. 2005. doi:10.1080/10618560701678647.

[19] Carreras.B.A. *IEEE Trans. Plasma Sci*, 245(1281), 1997.

[20] D. A. D'Ippolito, J. R.Myra, S. I.Krasheninnikov, G. Q. Yu, and A. Yu. Pigarov. Blob transport in the tokamak scrape-off-layer. *Plasma Phys*, 44:205–216, 2004.

[21] S. I. KRASHENINNIKOV. On scrape off layer plasma transport. *Physics Letters A*, 283:368–370, 2001.

[22] D'Ippolito, D. and Myra, J. and Zweben, S. Convective transport by intermittent blob-filaments: Comparison of theory and experiment. *Physics of Plasmas*, 18, 06 2011. doi: 10.1063/1.3594609.

[23] Halsig, Sebastian and Artz, Thomas and Iddink, Andreas and Nothnagel, Axel. Using an atmospheric turbulence model for the stochastic model of geodetic vlbi data analysis. *Earth, Planets and Space*, 68, 12 2016. doi: 10.1186/s40623-016-0482-5.

[24] Roger Lewandowski, Benoît Pinier. The kolmogorov law of turbulence, what can rigorously be proved ? *Springer*, 44:71–89, 2016.

[25] Derot, Jonathan. Use of marel carnot automatic biogeochemical data for understanding the mechanisms of extremes in water quality in boulogne-sur-mer. 12 2014.

[26] Garcia, Odd Erik. Blob transport in the plasma edge: a review. *Plasma and Fusion Research*, 4, 01 2009. doi: 10.1585/pfr.4.019.

[27] Myra, J. and D'Ippolito, D. and Stotler, Daren and Zweben, S. and Menard, J. and Maqueda, R. and Boedo, J. Blob birth and transport in the tokamak edge plasma: Analysis of imaging data. *Physics of Plasmas*, 13:092509–092509, 09 2006. doi: 10.1063/1.2355668.

[28] Liu, Haiqing and Hanada, K and Nishino, Nobuhiro and Ogata, R and Ishiguro, M and Zushi, H and Nakamura, Kikuyasu and Sato, K and Sakamoto, Mizuki and Idei, H and Hasegawa, Mikage and Higashizono, Y and Kawasaki, S and Nakashima, H and Higashijima, A and Group, Quest. Measurement of blob-like structure behavior in the plasma edge in quest. 01 2020.

[29] P. W. Terry. Suppression of turbulence and transport by sheared flow. *Department of Physics, University of Wisconsin-Madison, Madison, Wisconsin 53706*.

[30] R.A. Antonia et al . Experiments in fluids. 33:384–390, 2002.

[31] T. Zhou et al. Experiments in fluids. pages 459–471, 2003.

[32] P. Sullivan and A. Pollard. Meas. sci. technol. 7:1498–1516, Oct. 1996.

[33] T. Zhou et al. *Experiments in Fluids*, 33:334–345, 2002.

[34] M.Y. Tanaka et al. 29th eps conf. on plasma phys. control. fusion, montreux. 18, June 2002.

[35] K. Nagoaka et al. *Experiments in Fluids*, 33:334–345, 2002.

[36] T. Zhou et al. *Phys. Plasmas*, 10:2211– 2216, 2003.

[37] T. Zhou et al. *Phys. Rev. Lett.*, 89(075001), 2002.

[38] Jean C. Perez and W. Horton and Roger D. Bengtson and and Troy Carter. *Phys. Plasmas*, 055701, 2006.

[39] W. Horton et al. *Phys. Plasmas*, 12, 2005.

[40] Lautrup, J.B . Physics of continuous matter: Exotic and everyday phenomena in the macroscopic world. pages Institute of Physics Publishing, Bristol, U.K.; Philadelphia, U.S.A., 2005.

[41] S.B. Korsholm and P.K. Michelsen and V. Naulin and J. Juul Rasmussen and L. Garcia and B.A. Carreras and V.E. Lynch. Reynolds stress and shear flow generation. *Plasma Phys. Control. Fusion*, 43:1377–1395, 2001. In this work it is investigated an alternative method, based on density measurements, to estimate the Reynolds stress, and demonstrate the validity range of this quantity.

[42] G. G. Craddock and P. H. Diamond. *Phys. Rev. Lett*, 67(1535), 1991.

[43] H. Bigliari et al. Radio frequency power in plasmas. *AIP Conf. Proc. No. 244(AIP, New York*, page 376.

[44] C. Hidalgo and C. Silva and M. A. Pedrosa and E. Sánchez and H. Fernandes and C. A. F. Varandas. Radial structure of reynolds stress in the plasma boundary of tokamak plasmas. *Physical review letters*, 83(11), Sept. 1999. Investigation of the radial profile of Reynolds stress in the plasma

boundary region of the ISTTOK tokamak using a multiarray of Langmuir probes. A radial gradient close to the velocity shear layer location is found, exhibited by the electrostatic Reynolds stress component which is proportional to the crosscorrelation of radial and poloidal fluctuating fields.

[45] C.Silva, H. Figueiredo, I.Nedzelskiy, B. Gonçalves, C. Varandas. Control of the edge turbulent transport by emissive electrode biasing on the tokamak isttok. *Plasma Physics and Controlled Fusion*, 48:727, 04 2006. doi: 10.1088/0741-3335/48/6/002.

[46] C.Silva, H. Figueiredo, I.Nedzelskiy, J. Cabral, C.Varandas,J. Stockel. Limiter biasing experiments on the tokamak isttok. *Czechoslovak Journal of Physics*, 53:937–944, 09 2003. doi: 10.1023/A:1026300808534.

[47] H. Figueiredo, I. Nedzelskiy , C.Silva ,J. Cabral, C. Varandas. Rev. sci. instrum. 75 4240. 2004.

[48] F. David, D. Persi . On the histogram as a density estimator: L2 theory. *Probability Theory and Related Fields*, 57:453–476, 1981.

[49] J.M. Beall and Y.C. Kim and E.J. Powers. Estimation of wavenumber and frequency spectra using fixed probe pairs. *Department of Electrical Engineering and Electronics Research Center, The University of Texas at Austin, Austin, Texas*, 1981. The local wavenumber and frequency spectral density is shown to be equivalent to the conventional wavenumber and frequency spectral density when the fluctuation is stationary and homogeneous and consists of a superposition of wave packets; such a fluctuation is the basic model used in many turbulence theories. A digital method for estimating the local wavenumber spectrum is described and applied to the study of drift-wave turbulence in an rf-excited discharge.

[50] Kat, Roeland and Ganapathisubramani, Bharathram. Frequency–wavenumber mapping in turbulent shear flows. *Journal of Fluid Mechanics*, 783:166–190, 11 2015. doi: 10.1017/jfm.2015.558.

[51] B Hooper Jr, E . Correlation techniques in experimental plasma physics. *Plasma Physics ,*, page Institute of Physics (Great Britain).

[52] P. Cripwell et al 1991 . 18th european conf. on controlled fusion and plasma physics vol 14b part i. p 17. 1991.

[53] Gilmore M. et al. Plasma phys. control. fusion 42 l1. 2000.

[54] `http://www.cfn.ist.utl.pt/eng/Prj_Tokamak_main.html`.

[55] D C Robinson. The present role of small tokamaks. *Plasma Physics and Controlled Fusion*, 35 (SB):B91–B104, dec 1993. doi: 10.1088/0741-3335/35/sb/007. URL `https://doi.org/10.1088%2F0741-3335%2F35%2Fsb%2F007`.

[56] Dinklage, A. Klinger, Th. Marx, G. Schweikhard (Eds.) . Plasma physics confinement, transport and collective effects. pages Springer–Verlag Berlin Heidelberg.

[57] E. Martines et al. Nuclear fusion 39, 581. (1999).

[58] Biglari H. et al. Phys. fluids b2 1. 1990.

[59] B. Goncalves, C. Hidalgo, C. Silva, M.A. Pedrosa, K. Erents . Statistical description of the radial structure of turbulence in the jet plasma boundary region. (2005).

[60] B. Gonçalves , I. Henriques,C. Hidalgo , C. Silva, H. Figueiredo, V. Naulin, A. H. Nielsen, J.T. Mendonça . Radial structure of vorticity in the plasma boundary of isttok tokamak. 2008.

[61] B. Gonçalves et al . 20th iaea fusion energy conference, 1-6 november 2004, vilamoura, portugal. 2004.

[62] C. Hidalgo et al . 31st eps conference on controlled fusion and plasma physics, 28 june-2 july 2004, london, uk. 2004.

[63] B. Gonçalves et al. . Journal of nuclear materials, volumes 337–339, , pages 376–380. 2005.

[64] B. Gonçalves, C. Hidalgo, M.A. Pedrosa, R. O. Orozco, E. Sánchez, C. Silva . Phys. rev. lett., 96 145001. 2006.

[65] G. Kaniadakis, M. Lissia, and A.M. Scarfone . Physica a, 340, 41. 2004.

[66] G. Kaniadakis, M. Lissia, and A.M. Scarfone . Phys. rev. e, 71, 046128. 2005.

[67] Lavagno, A.M. Scarfone, and S. Narayana . J. phys. a: Math. theor., 40, 8635. 2007.

[68] C. Tsallis, M. Gell-Mann, and Y. Sato . Europhys. news 36, 186. 2005.

[69] J.A. Marsh, M. A. Fuentes, L. G. Moyano and C. Tsallis . Physica a, 372, 183. 2006.

[70] G. Livadiotis et al. . Journal of geophysical research, vol.114, a11105.

[71] F. Caruso, A. Pluchino, V. Latora, S. Vinciguerra and A. Rapisard . Phys. rev. e, 75, 055101. 2007.

[72] L. F. Burlaga, A. F. Vinas, N. F. Ness and M. H. Acuna . Apj. j., 644, l83. 2006.

[73] V. Antoni et al . Phys. rev. lett. 80, 4185. 1998.

[74] M.Xu et al . Prl 107, 055003. 2011.

[75] R. Sanchez et al . Plasm. phys. control. fusion 53. 2011.

[76] Nielsen et al . Phys. lett. a 379 3097. 2015.

[77] Ricci et al . Plasma phys. control. fusion 54 124047. 2012.

Appendix A

Derivation for the Langmuir probe results

Describing electrons by the distribution function $f(x, v, t)$ which gives the number of electrons per unit of volume with velocity between v and $v + dv$ at the position x and time t, the electron density is given by:

$$n_e(x,t) = \int f(x,v,t) dv_x dv_y dv_z \tag{A.1}$$

The electron current density to the probe can be written as:

$$j = e \int f(v) v.\hat{n} d^3 v \tag{A.2}$$

where the $\hat{n}$ is the normal to the probe surface. Assuming that the sheath dimensions are small compared to the probe dimensions and that the probe is approximately planar, the probe current density it is given by:

$$j = e \int_{v_{min}}^{\infty} \int_{-\infty}^{\infty} \int_{-\infty}^{\infty} f(v_x, v_y, v_z) v_z dv_x dv_y dv_z, \tag{A.3}$$

with $v_{min} = [2e(V_p - V_B)/m_e]^{1/2}$, V_B the probe bias and m_e the electron mass. Integrating over the two velocity components perpendicular to the probe:

$$j = e \int_{v_{min}}^{\infty} f_z(v_z) dv_z \tag{A.4}$$

Expressing the plasma density in spherical polar coordinates:

$$n = \int f(v, \theta, \phi) v^2 sin\theta dv d\theta d\phi \tag{A.5}$$

and assuming an isotropic distribution function

$$n = 4\pi \int v^2 f(v) dv = 4\pi \sqrt{\frac{2}{m^3}} \int f(\epsilon) \sqrt{\epsilon} d\epsilon \tag{A.6}$$

with $\epsilon = mv^2/2$ and $f(\epsilon)$ obtained by replacing v in $f(v)$ by $\sqrt{2\epsilon/m}$. The energy distribution function $f_E(\epsilon)$ can be identified as:

$$f_E(\epsilon) = 4\pi\sqrt{\frac{2}{m^3}}f(\epsilon)\sqrt{\epsilon} \tag{A.7}$$

The current density to a negatively biased planar probe in therms of spherical polar coordinates comes as:

$$j = e\int_{v_{min}}^{\infty}\int_{\theta_{min}}^{\frac{\pi}{2}}\int_{0}^{2\pi} vcos\theta f(v,\theta,\phi)v^2 sin\theta dv d\theta d\phi \tag{A.8}$$

which for an isotropic distribution function $f(v,\theta,\phi) = f(\epsilon)$ reduces to:

$$j = e\frac{2\pi}{m^2}\int_{e(V_p-V_B)}^{\infty}\epsilon f(\epsilon)\left(1-\frac{e(V_p-V_B)}{\epsilon}\right)d\epsilon \tag{A.9}$$

The electron current per unit area to a planar probe biased at V_B is calculated with:

$$j_e(V_B) = e\int f(x,v,t)v_z dv_x dv_y dv_z) \tag{A.10}$$

A sufficiently negative bias voltage on the probe V_B with respect to the plasma potential V_P collects positive ions until the bias voltage reach V_P. After this the positive ions start getting repelled. On other hand, with V_B¿¿V_P, the probes collects electron saturation current I_{es}. For nondrifting Maxwellian electron, the velocity distribution $f(x,v,t)$ is given by:

$$f(x,v,t) = ne\sqrt{\left(\frac{m_e}{2\pi T_e}\right)^3}exp\left[-\frac{m_e v^2}{2T_e}\right] \tag{A.11}$$

The expression for the probe current as function of V_B is given by:

$$I_e(V_B) = \begin{cases} I_{es}exp\left[-e\left(\frac{V_P-V_B}{kT_e}\right)\right] & \text{if } V_B \leq V_P, \\ I_{es} & V_B > V_P \end{cases} \tag{A.12}$$

with I_{es} the electron saturation current that can be obtained by integrating the equation A.9 and its given by:

$$I_{es} = \frac{1}{4}en_e v_e A_{probe} \tag{A.13}$$

where $v_e = \sqrt{\frac{8kT_e}{\pi m_e}}$ is the electron thermal speed, m_e the electron mass and n_e the plasma electron density.

A.1 Vector identities

$$\nabla \times (\nabla\phi) = 0 \tag{A.14}$$

$$\nabla \cdot (\nabla \times \mathbf{u}) = 0 \tag{A.15}$$